

**MIXED LAYER DYNAMICS FROM REMOTE
SENSING OBSERVATIONS**

THESIS

**SUBMITTED TO THE GOA UNIVERSITY
FOR THE DEGREE OF DOCTOR OF PHILOSOPHY
IN MARINE SCIENCE**

By

K. N. BABU



574.92

BAB/MIX

T-358

August, 2006

T-358

STATEMENT

As required under the University ordinance 0.19.8 (vi), I state that the present thesis entitled "**MIXED LAYER DYNAMICS FROM REMOTE SENSING OBSERVATIONS**", is my original contribution and the same has not been submitted on any previous occasion. To the best of my knowledge, the present study is the first comprehensive work of its kind from the area mentioned.

The literature related to the problem investigated has been cited. Due acknowledgements have been made wherever facilities and suggestions have been availed of.

Place: *Coa, University*
16/5/2007
Date:



A handwritten signature in black ink, appearing to read "K. N. Babu".

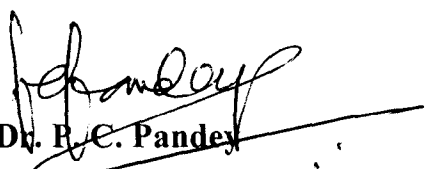
K. N. Babu

CERTIFICATE

This is to certify that the thesis entitled “**MIXED LAYER DYNAMICS FROM REMOTE SENSING OBSERVATIONS**”. Submitted by Mr. K. N. Babu for the award of the Degree of Doctor of Philosophy in Marine Science is based on his original studies carried out by him under our supervision. The thesis or any part thereof has not been previously submitted for any other degree or diploma in any universities or institutions.

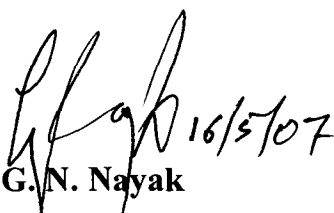
Place:

Date:


Dr. P. C. Pandey
(Research Guide)

Former Director

NCAOR, Goa-403 804


Dr. G. N. Nayak
(Research Co-guide)
Professor of Marine Science
Head, Dept. of Marine Sciences
Goa University, Goa-403 206

Acknowledgments

I am most indebted to my supervisors Dr. P. C. Pandey, former Director, National Centre for Antarctic and Ocean Research, Goa, India and Dr. G. N. Nayak, Professor of Marine Sciences, Dean of Faculty of Life Sciences and Environment, Goa University, Goa, India for their continuous guidance and support. It is true to say that without their support and encouragement this thesis would not have materialized. I learned a great deal from their guidance.

I would like to record my gratitude to my Teachers Dr. M. Dhakshinamurthy, Dr. B. Gananaprakasam fostered my interest in research field and quietly inspired me with their brilliance. I am gratified to, Dr. Sankara, and Dr. A. K. S. Gopalan, former Directors and Dr. R. R. Navalgund, Director, Space Applications Centre, Ahmedabad for being a constant source of inspiration.

I would like to thank Dr. M. M. Ali, Head of Department, Oceanography Division, National Remote Sensing Agency, Hyderabad and Dr. M. Ramesh Kumar, Scientist, Physical Oceanography Division, National Institute of Oceanography, Goa, India for their valuable scientific guidance. Thanks to Dr. Ramesh for being my research council member at Goa University and for his valuable constructive comments. Also grateful to Dr. M. S. Narayanan, and his family, who offered homely situation in Ahmedabad. Mrs. SathyaBama Karthikeyan and her family also share this place in my heart.

I take this opportunity to thank Dr. Rashmi, Scientist, Ocean Sciences Division, who greatly helped in shaping the results in thesis form. Without her support and interest it would have been difficult for me to complete in time. I am thankful to the scientific group of Meteorology and Oceanography Group, Dr. V. K. Agarwal, Dr. P. C. Joshi, Dr. A. Sarkar, Dr. M. Mohan, and Dr. S. K. Basu.

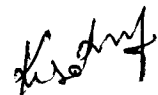
Dr Jim Price and Dr. Weller, Senior Scientists, (WHOI Massachusetts, USA) provided their model code and their. I am very much grateful to Dr. Weller for his

time-to-time suggestions. I have benefited from discussions with Shri. R. M. Dwivedi, and Dr. R. R. Rao.

My sincere thanks to my family friends, Sukanya BalaSubramaniam, Loganathan, Varalakshmi, Anand, Vicky, Murali, Antony, Sathyamoorthy, Kartikeyan, Durai Pandiyan, and Durai Raj and my friends at SAC especially Bintu, Neeraj Agarwal, Yaswant, Netaji, Falguni, Pawan, Sushil, Indrani Chadhury, Indrani Das, Neetu, Jigesh, Rajini Kant, and Neeraj Rastogi. Also my special thanks to NCAOR friends, Nagoji, Nilay, Raja Kumar, Anil Kumar, Praveen, Luis, Amita, Subramaniam, Sushant and Ganesh. A Special regards to Dr. Mihir. K. Dash and Dr. P. SriRam.

I am deeply indebted to my parents, who have done so much and always been a source of my inspiration. This thesis is made for their tribute to convey my gratitude. They gave me unconditional love and support throughout my life and have always encouraged me to dream. I am very grateful to rest of my family members and my wife for their love and affection.

Place: Coaa, University
Date: 16/5/2007



K. N. Babu

The more insight we gain into the interrelation of phenomena, the easier it will be to free ourselves from the misconception that not all branches of the natural sciences, be they the observing and describing branches, the investigation of chemical components, of the exploration of the everywhere existing physical forces of matter, are of equal importance for the culture and prosperity of mankind.

Alexander von Humboldt

Kosmos I, 1845

PREFACE

The northern Indian Ocean spanning from 30°E to 120°E longitude and -30°N to 30°N latitude including Bay of Bengal, Arabian Sea and southern Indian Ocean has been chosen for investigating the estimation of marine mixed layer depth by 1-Dimensional model and its variability by using remote sensing observations. The Indian Ocean is a unique environment for studying the forced upper ocean response with distinct atmospheric forcing of characteristic monsoonal cycles with reversing winds and transition periods. The transition periods are characterized by weak winds, enhanced evaporative rate and heat fluxes. The strong seasonal cycle in surface forcing over the Arabian Sea leads to seasonal circulation along the Somalia coast. Normally, Arabian Sea saltier than rest of the Indian Ocean, while large run off draining the Indian subcontinent makes the Bay of Bengal significantly fresher.

The progress of oceanographic and Meteorological research and operations heavily relies upon a variety of oceanic observations. The *in-situ* measurements are hindered because of the natural and obvious difficulties. Mixed layer depth (the depth of quasi-homogeneous/homogeneous physical properties of the upper ocean from the surface) is one such parameter; to understand its dynamical behavior large amount of *in-situ* data collection at subsurface level over temporal and spatial resolution are needed.

On the other hand satellite sensors (operating in optical, thermal, and microwave channel) are capable of delivering many of the sea surface parameters, for eg. chlorophyll concentration, suspended sediment, yellow substances, sea surface temperature, wind speed, sea surface height, wave height, water vapor, and many other on synoptic and temporal coverage with retrieval accuracy. These modern observational tools significantly helped in overcoming the difficulty of sparse sea truth measurements. Microwave sensors have become indispensable part of remote sensing platforms particularly over tropical regions because of frequent cloud coverage.

However for getting subsurface information of ocean parameters is not possible from satellite platform. Often the ocean modelers, model the ocean with initial subsurface ocean state along with sea surface parameters. Satellite remote sensing and numerical ocean modeling has significantly helped in overcoming these difficulties and in enriching the understanding of oceanic features even at subsurface levels.

The various surface forcing and different methods of mixed layer modeling are explained under three major classifications in chapter 2. The relative comparisons of each model in-terms of its computational requirement and advantages are also explained.

The present analysis is initiated keeping in mind to identify various forcing parameters on marine mixed layer (which are space based observation or derivable from them) and its nature of spatio-temporal variability. And subsequently parameterize them into a 1-Dimensional marine mixed layer model with climatic temperature and salinity profile as initial subsurface fields. Sea surface temperature (SST), sea surface height (SSH), wind speed (WS), net heat gain (NHG), and evaporation minus precipitation (EMP) are analyzed for this purpose. The spatio-temporal variability of these surface parameters and relative variability with climatic mixed layer depth is explained in chapter 3. The criterion for mixed layer depth estimation and various methods of its estimation is given in appendix.

The 1-Dimensional mixed layer model of Price, Weller, and Pinkle (PWP, the model equations are diurnal in nature) is initiated with yearlong observations over 61.5°E , 15.5°N (October 1994 to October 1995) to explore the feasibility of incorporating remote sensing/re-analysis observations for mixed layer depth computation. The model equations and sensitivity to surface forcing is explained in chapter 4. The sensitivity study reveals that the wind speed is dominating the model performance compare surface total heat loss and radiation.

The following objectives are investigated and incorporated in order to model the mixed layer depth over northern Indian Ocean with satellite/re-analysis observations over spatial and temporal resolutions. They are;

- (1). Quantification of model diurnal heating at the ocean surface
- (2). Assimilation of surface forcing parameters from satellite derived/re-analysis parameters
- (3). Seawater classification based on chlorophyll concentration
- (4). Seasonal variability of model derived mixed layer depth.

The diurnal solar heating over the sea surface is modeled with average incoming shortwave radiation and total heat loss from surface. The method and its validation for the computation of shortwave radiation at a given model time step is explained in chapter 4. The diurnal variability of wind speed and total heat loss are assumed to daily average values to force the model.

Most of the ocean models treat ocean waters as type-1, open ocean waters. However the seasonal chlorophyll observations obtained from the coastal zone color scanner shows spatial and seasonal biological variability even incase of open, deep oceanic regions. Here a methodology is devised for classifying waters with the help of satellite derived chlorophyll concentration up to five water types, the details are explained in chapter 4.

The analysis of model performance for the year 1990 – 1996 studied with climatic temperature and salinity profiles. ERS scatterometer winds, comprehensive oceanic and atmospheric data sets total heat loss, and coastal zone color scanner seasonal chlorophyll concentration also used. Here the influence of chlorophyll concentration on mixed layer depth termed as biological heating. The model

results are compared with yearlong observations over central Arabian Sea and also with available conductivity temperature depth (CTD) observations from the Arabian Sea during the period 1994 - 1995.

The seasonal behavior of the mixed layer depth over Arabian Sea and Bay of Bengal is studied using the model derived mixed layer depth and empirical orthogonal function (EOF). The details of the data preparation and theory of empirical orthogonal function technique is given in chapter 5.

Chapter 6 elucidates overall outcome of the present work, limitations of the present methodology and scope of improvement as the future work in mixed layer modeling over Indian Ocean.

Contents

Acknowledgments	i
Preface	iv
Contents	ix
List of figures	xii
List of tables	xv
Chapter I	
Introduction	1
1.1 Background of work	1
1.2 State of art	3
1.3 Work proposed	5
1.4 The study area and its geographical importance	5
Chapter II	
Basics and modeling aspects of mixed layer	8
2.1 Definition	8
2.2 Upper Ocean Structure	8
2.3 Forcing on marine mixed layer	10
2.3.1 Radiative forcing	11
2.3.2 Wind forcing	16
2.3.3 Solar penetrative profile	20
2.3.4 Evapo-precipitation	22
2.4 Basic mixing mechanism	23
2.4.1 Radiative mixing	23
2.4.2 Wind mixing	26
2.5 Mixed layer models	28
2.6 Summery	38
Chapter III	
Spatiotemporal distribution of mixed layer depth and forcing parameters	41
3.1 Introduction	41

3.2	Spatiotemporal distribution of mixed layer depth	41
3.3	Spatiotemporal distribution of wind speed	46
3.4	Spatiotemporal distribution of sea surface height	50
3.5	Spatiotemporal distribution of net heat gain	54
3.6	Spatiotemporal distribution of sea surface temperature	58
3.7	Spatiotemporal distribution of evaporation minus precipitation	63
3.8	Temporal variability of parameters at selected locations	66
Chapter IV		
	One-dimensional model and parameterization	70
4.1	Mixed layer model	70
4.1.1	The model equations	70
4.1.2	Mixing	72
4.2	Sensitivity analysis	73
4.2.1	Model sensitivity with surface forcing	73
4.2.2	Model sensitivity to ability of solar penetration	77
4.3	Yearlong model computation and comparison with <i>in-situ</i> observations	79
4.3.1	Over view of atmospheric data	79
4.3.2	Over view of oceanic response and mixed layer	83
4.3.3	Model performance with <i>in-situ</i> observations	86
4.4	Remote sensing parameters in mixed layer computation	87
4.4.1	Diurnal variation of model forcing parameters	87
4.4.2	Parameterization of radiative forcing	88
4.4.3	Validation of noon radiation	90
4.4.4	Parameterization of ocean turbidity	92
4.5	Seasonal variation of attenuation coefficient and chlorophyll concentration over Indian ocean	93
4.6	Model run with constant and variable biology	97
4.7	Validation of ERS scatterometer wind	98
4.8	Analysis of the model simulations	99

4.9	Evolution of MLD in the central Arabian Sea	100
4.10	Summary	105
Chapter V		
	Seasonal variability of mixed layer depth	107
5.1	Introduction	107
5.2	Havmoller diagram of mixed layer depth	109
5.3	EOF analysis of MLD	111
5.3.1	EOF over Arabian Sea	114
5.3.2	EOF over Bay of Bengal	117
5.4	Summary	120
	Conclusion	122
	Reference	129
	Annexure	148

List of figures

Fig. 1	Area of study	6
Fig. 2.1	Typical mean temperature/depth profiles for the open ocean	9
Fig. 2.2	A typical structure of the layers in the upper ocean	25
Fig. 2.3	The schematic diagram of wind force mixing in marine mixed layer	27
Fig. 2.4	Contributors to mixing the upper ocean	39
Fig. 3.1a	Spatial distribution of marine mixed layer depth	44
Fig. 3.1b	Continuation ...	45
Fig. 3.2a	Mean monthly distribution of wind speed	48
Fig. 3.2b	Continuation ...	49
Fig. 3.3a	Monthly mean distribution of sea surface height anomaly	52
Fig. 3.3b	Continuation ...	53
Fig. 3.4a	Monthly mean distribution of net heat gain	55
Fig. 3.4b	Continuation ...	56
Fig. 3.5a	Monthly mean distribution of sea surface temperature	59
Fig. 3.5b	Continuation ...	60
Fig. 3.6a	Monthly mean distribution of evaporation minus precipitation	64
Fig. 3.6b	Continuation ...	65
Fig. 3.7	Temporal variation of parameters	68
Fig. 4.1	Geo-location of surface mooring	74
Fig. 4.2	Model sensitivity curves	75
Fig. 4.3	Path length of solar radiation in different water type	78
Fig. 4.4	Measured radiative flux observations over the buoy time span	80
Fig. 4.5	Meteorological observation over the buoy time span	82
Fig. 4.6	Upper ocean thermal and density distribution over surface mooring	84
Fig. 4.7	Estimated MLD and the parameter concerned for its variation	85
Fig. 4.8	Comparison of model with buoy observations MLD	86

Fig. 4.9	Typical one day diurnal cycle of the radiative and wind forcing to the model	88
Fig. 4.10	Model solar cycle	89
Fig. 4.11	Comparison of solar cycles	89
Fig. 4.12	Comparison of <i>in-situ</i> noon radiation	91
Fig. 4.13a	Seasonal distribution of chlorophyll concentration, and short-wave extinction coefficient	95
Fig. 4.13b	Continuation ...	96
Fig. 4.14	Time series of the daily averaged ERS scatterometer wind speed and observed daily averaged wind speed at the mooring site	98
Fig. 4.15	Scatter plot of MLD simulated with variable biology versus observed MLD from CTD observations	100
Fig. 4.16	(a) Annual changes of MLD at the central Arabian Sea simulated from model with constant and varying biology, and MLD from in situ observations. Time series of (b) wind (ms^{-1}) and (c) extinction depth (meters).	102
Fig. 4.17	Monthly averaged mixed layer depth at the central Arabian Sea simulated from model with constant and varying biology. Also shown is the MLD from <i>in-situ</i> observations.	103
Fig. 4.18	Distribution of difference of the two MLDs (simulated using constant and varying biology) over the study area during January, May, August, and November of 1994.	105
Fig. 5.1	Havmoller plot of MLD over Arabian Sea and Bay of Bengal along 15° N	110
Fig. 5.2	The time filter used to smooth the high frequency and delete the low frequency components in the data	114
Fig. 5.3	EOF over Arabian Sea	116
Fig. 5.4	EOF over Bay of Bengal	119

Fig. app. Time series of MLD (meters) computed with density (dashed - 150 line) and temperature (solid line) criteria at the data buoy location in central Arabian Sea

List of tables

Table 4.1a	Percentage reduction of model MLD: with constant noon radiation and wind speed and for varying total heat loss	76
Table 4.1b	Percentage reduction of model MLD: with constant total heat loss, wind speed and for varying noon radiation	76
Table 4.1c	Percentage reduction of model MLD: with constant total heat loss, noon radiation and for varying wind speed	77
Table 4.2	Model computed result under unified forcing condition in different water types	79

Chapter I
Introduction

1.1 Background of work

The vertical temperature structure in the ocean is generally divided into three zones. There is an upper layer of the ocean (0m-200m) with fairly uniform temperatures similar to those at the sea surface. The thermocline is the zone below the mixed layer up to approximately 500m in which the temperature gradient (rate of change of temperature with depth) is at maximum. Below the thermocline is a deep zone in which temperature changes slowly. The depths of these features vary with time and geographic location. The upper layer of the ocean exhibits a surface Mixed Layer (ML), whose thickness vary by tens of meters over a diurnal cycle (Price et al., 1986; Denman and Gargett, 1988; Schneider and Muller, 1990) and by 100m over an annual cycle (Dodimead et al., 1963; Sprintall and Roemmich, 1999; Pickard, 1982). The ocean mixed layer is generally considered a quasi-homogeneous region in the upper ocean where there is little variation in temperature or density with depth. This definition is based on profiles from in-situ data that clearly reveal the presence of approximately uniform vertical regions of temperature and salinity starting at the ocean surfaces or at some shallow depth below (eg. Roden, 1979; Pickard and Emery, 1990; Monterey and Levitus, 1997). These regions of vertical uniformity owe their existence to turbulent mixing generated from the energy input by the action of wind stress and heat fluxes at the ocean surface, there by this layer possesses a homogeneous/quasi-homogeneous properties. The depth of the upper ocean from the surface, up to which the physical properties are nearly homogeneous, is called Mixed Layer Depth (MLD).

The heat capacity of the top two and one-half meter of the ocean equals that of the whole column of air above it. Thus, ocean essentially acts as a "thermal flywheel" for the climate system. Knowledge of the seasonal and maximum annual depth of the thermocline is of importance for heat storage in the Ocean (White et al., 1998; Gallimore and Houghton, 1987; Meehl, 1984; Stevenson and Niiler, 1983). The ocean's effect on weather and climate is governed largely by processes (upper ocean mixing, wave braking, ocean circulation and bio-geochemical cycle) occurring in the few ten meters of water bordering at the ocean surface. For example, water warmed at the surface on a sunny afternoon may remain available to warm the atmosphere that evening, or it may be mixed deeper into the ocean not be emerge for many years, depending on near-surface mixing processes. Local mixing of the upper ocean is predominantly forced from the state of the atmosphere directly above it. The daily cycle of heating, cooling, wind, rain, changes in temperature and humidity associated with mesoscale weather feature produce a hierarchy of physical processes that interact to stir the upper ocean.

The response of the upper ocean to diurnal variations of solar heating has a long research history (Defant, 1961). Interest in the subject has revived in recent years as climatologists have realized that failure to resolve or adequately parameterize the diurnal cycle of mixing in the upper ocean. This leads to systematic errors in the seasonal and longer-term temperature and depth of the mixed layer (Woods, 1984). Sea surface and mixed layer processes also play a vital role in the exchange of gases such as O₂ and CO₂ between the atmosphere and the ocean. The

exchange occurs by diffusion across the sea surface and bubbles created by breaking waves (eg. Wanninkhof, 1992). CO₂ is taken up in the surface layers of the ocean by growing phytoplankton, with the growth rate depending upon the availability of nutrients that are entrained from below to the base of the mixed layer. The average light intensity to which the phytoplankton are exposed is also critical and this becomes insufficient for further growth if the depth over which the phytoplankton are mixed becomes too great (Denman and Gargett, 1995). The physics of this surface mixed layer presents a variety of fascinating fluid dynamical problems, and is of great importance for a wide variety of problems arising in studies of climate, air-sea interaction, biological productivity, under water acoustic propagation and marine population. Hence, the study of the mixed layer and its variability has more importance.

1.2 State of Art

The conventional way of studying the mixed layer depth is from temperature/density profiles. Having such profiles all over the study region with desirable temporal resolution is not possible. To overcome these difficulties a number of previous investigators have developed the oceanic mixed layer model to study the upper ocean dynamics and the processes of air-sea interactions (Kraus and Turner, 1967; Denman, 1973; Mellor and Yamada, 1982; Niiler and Kraus, 1977; Clancy and Pollack, 1983; Price et al., 1987; Stull and Kraus, 1987). Various algorithms have been used to analyze the *in-situ* surface and subsurface temperature variations. All these method needs heat flux and turbulent flux at the sea surface,

which varies the temperature and mixed layer thickness. Thus all the models determine mixed layer thickness at each model time step with reference to its initial state parameters.

An analytical mixed layer thermal inertia model based on remote sensing data is investigated by Yan et al., (1989a, b, 1991) to estimate the diurnal mixed layer thickness and the thermal inertia of the mixed layer, with the assumptions that the horizontal advection and horizontal diffusion are less. Chu et al., (1999, 2000) used a parametric model (based on the layered structure of the upper ocean temperature) for determining subsurface thermal structure from satellite sea surface temperature observations. Ravindran et al., (1999) modulated energy conservation equation in estimation of mixed layer depth and sea surface temperature for the ocean weather station papa. In regions such as the equatorial oceans, shear-induced mixing at the thermocline base can play an important role in deepening the mixed layer. Further to account this effect, Chen et al., (1994) have developed a hybrid-mixing scheme in which the evaluation of the mixed layer is described using the Kraus and Turner formulation (Kraus and Turner, 1967), and the evaluation of the thermocline is described using the vertical mixing scheme of Price et al., (1986), which is based on the critical Richardson number criterion. Review of marine mixed layer modeling is given in chapter 2.

1.3 Work proposed

A 1-Dimensional mixed layer model of Price et al., (1986) is used for the investigation of upper ocean dynamics (along with satellite derived geo-physical surface parameters), which accounts for the diurnal heating and wind mixing process over the Pacific Ocean region. Fischer, (1997, 2000) used this model to study the upper ocean response to the Indian Ocean monsoon over the central Arabian Sea at the US Data Buoy location (61.5°E; 15.5°N). However, in the present study, the mixed layer depth estimation and its variability have been studied in detail over the entire north Indian Ocean using remote sensing and re-analysis observations.

1.4 Study area and its geographical importance

The north Indian Ocean spanning from -30°N to 30°N latitude and 30°E to 120°E longitude including the Bay of Bengal (BOB), Arabian Sea (AS), and Southern Indian Ocean (SIO) has been chosen for investigation. Figure 1 shows the study region. The upper ocean thermal structure and stability to uphold the mixing in the ocean interior over the Indian Ocean differs significantly from that in the other two basins (Pacific and Atlantic ocean). Indian Ocean is a unique environment for studying the forced upper ocean response, with strong and distinct atmospheric forcing regimes, and a clear separation in the time domain between mesoscale oceanic variability and variability in the atmospheric forcing. It is influenced by a unique monsoonal cycle, with reversing wind forcing, an evaporative fresh water flux over most of the basin, and an annual mean net heat gain.

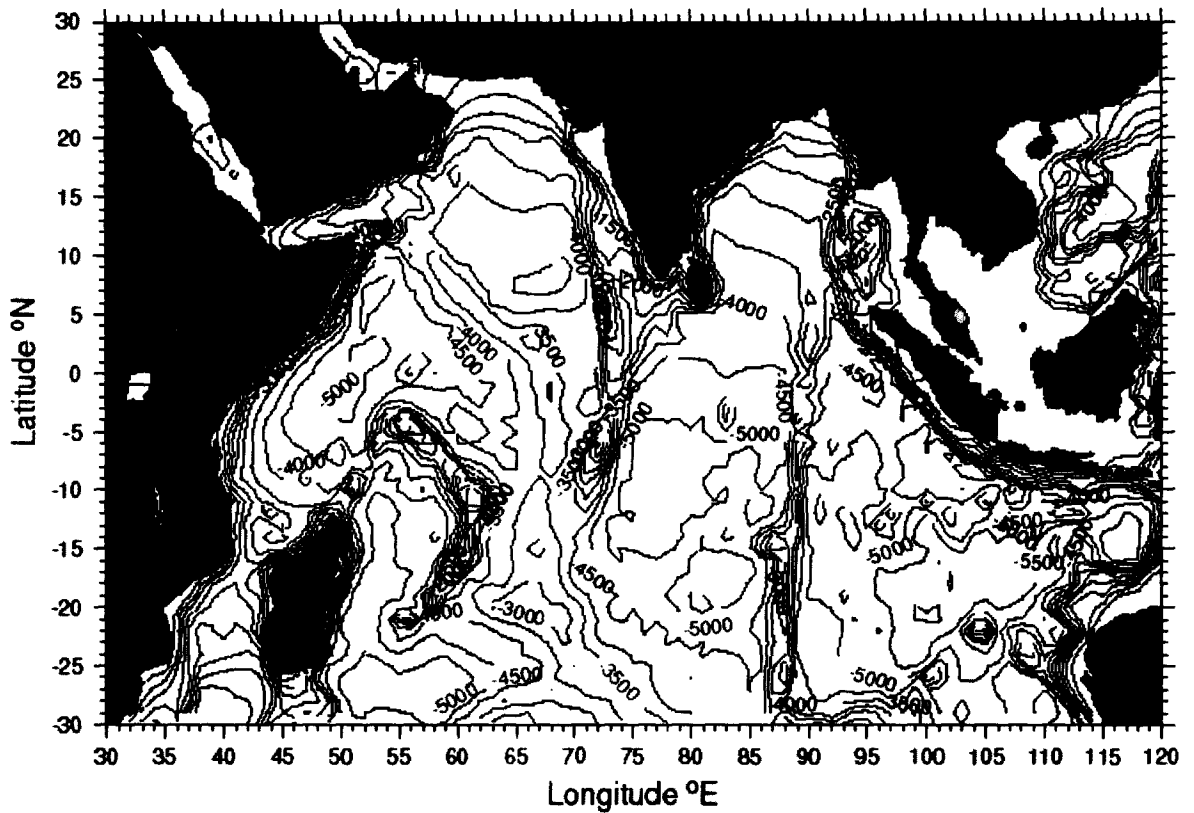


Fig. 1: Area of study spanning longitudinally from 30°E to 120°E and along latitudinal direction from -30°N to 30°N, consisting of Arabian Sea, Bay of Bengal, and southern Indian Ocean (referred to Indian Ocean from equator to -30°N).

However, compared to the tropical Pacific or the north Atlantic, the role of the Indian Ocean is very little understood. The Tropical Indian Ocean is one of the essential regions where El Nino southern oscillation in the Tropical Pacific Ocean and the Asian monsoon system interact (Webster and Yang, 1992). The wintertime northeast monsoon (NEM, from December to February) is characterized by mild to moderate wind stress and an oceanic heat loss leading to a destabilizing surface buoyancy flux for the ocean leading to convective mixing (deepening of MLD). The southwest monsoon (SWM, from June to August) brings strong surface wind forcing across the central Arabian Sea in the form of the Findlater jet (Findlater, 1969), and a neutral to strong stabilizing surface

buoyancy flux, again deepening the mixed layer depth due to turbulence. The two transition periods are characterized by weak wind forcing and large evaporative and heat fluxes. Excess evaporation makes the upper ocean, Arabian Sea, saltier than rest of the Indian Ocean, while large run off from rivers draining the Indian subcontinent makes the eastern part, the Bay of Bengal, significantly fresher. The marked seasonal cycle in the surface forcing over the Arabian Sea leads to a strong seasonal cycle in the circulation of the Arabian Sea along the Somalia coast. The Somalia current in the western boundary peaks up to 3.7 ms^{-1} during the southwest monsoon (Schott, 1983). Observations also have found a vigorous mesoscale eddy features in the Arabian Sea (Molinari et al., 1990; Flagg and Kim, 1998; Kim et al., 2001). The southwest monsoon wind field causes upwelling along the Arabian coast. All these intra-seasonal atmospheric and oceanic process have significant role on upper ocean dynamics and hence mixed layer depth variations.

Chapter II
**Basics and modeling aspects of mixed
layer**

2.1 Definition

Action of wind, wave and radiation induces vertical mixing in the upper columnar water of the ocean. Mixed layer is that portion of the upper ocean where significant physical, chemical and biological activities are taking place. This layer is well mixed by wind and waves and hence it possess homogeneous/quasi-homogeneous properties like temperature, salinity and density and is known as mixed layer depth and it is confined to a depth of 20m – 150m in the Indian Ocean.

2.2 Upper Ocean Structure

The salient feature of the oceanic thermal structure is a remarkably shallow thermocline, especially in the tropics and subtropics. Which factors determine its depth? The oceanic circulation that maintains this thermal structure has two main components, a shallow wind-driven circulation and a deep thermohaline circulation. Theories for the deep thermohaline circulation provide an answer that depends on oceanic diffusivity (but they deny the surface winds an explicit role). Theories for the shallow ventilated thermocline take into account the influence of the wind explicitly. To complete and marry the existing theories, for the oceanic thermal structure Giulio et al., 2004, proposed a balanced heat budget for the ocean. According to his theory, oceanic heat gain occurs primarily in the upwelling zones of the tropics and subtropics and depends strongly on oceanic conditions, specifically the depth of the thermocline. The heat gain is large when the thermocline is shallow but is small when the thermocline is deep. Therefore,

an increase in heat loss in high latitudes can result deepening the thermocline and decrease in heat loss can cause shoaling of the tropical thermocline.

Based on thermal property of ocean, it is divided into three zones. There is an upper zone from surface to 200m depth, and a zone below this extending to 500m (thermocline) and a deep zone. The temperature in the upper layer shows seasonal variations, particularly in middle latitudes. Over the mid-latitude oceans, at winter season sea surface temperature is low and the mixed layer is deep and may extend to the main thermocline (~150m from surface) and during summer season surface temperature rises and a seasonal thermocline often develops in the upper ocean. Figure 2.1 shows the thermal structure of the ocean at low, mid, and high latitudes.

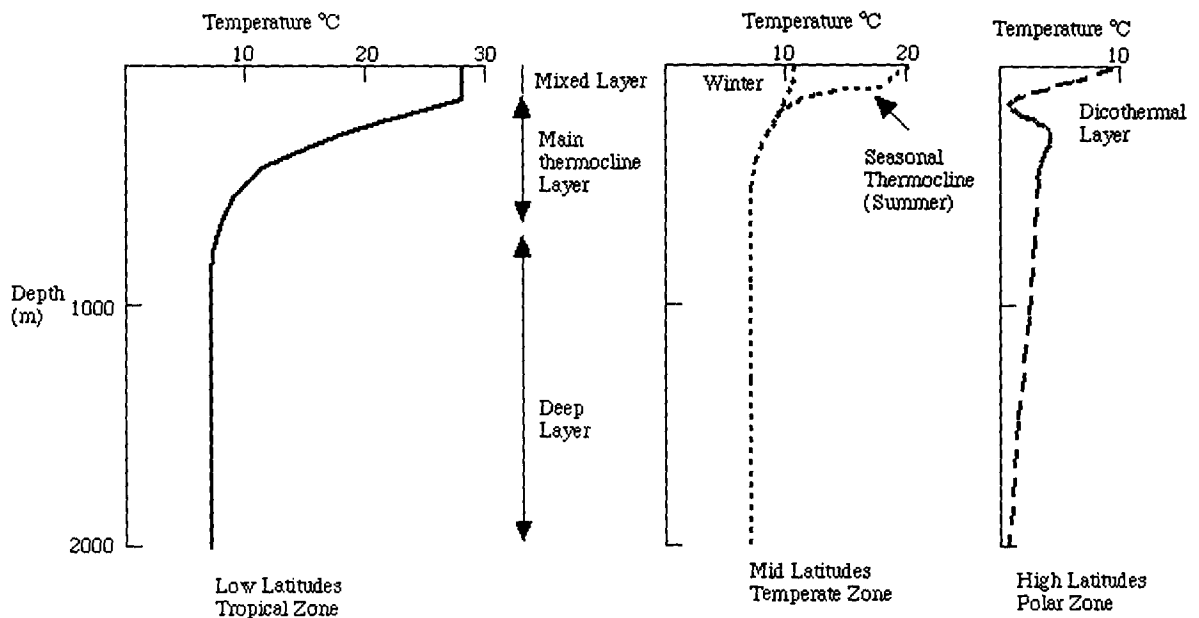


Fig. 2.1: Typical mean temperature/depth profiles for the open ocean. (Adapted from Pickard and Emery, 1982)

2.3 Forcing on marine Mixed Layer

The different physical processes that control the change in physical and chemical properties of the upper ocean are called the atmosphere-ocean exchange processes and which are divided into four parts;

- (1) Radiative forcing
- (2) Wind forcing
- (3) Penetration of solar radiation
- (4) Evapo-precipitation

The radiative forcing plays a vital role in vertical convective processes rather than horizontal advection in the upper ocean. As a result the vertical process has significant role than the horizontal one in changing the upper ocean properties at any given time. For example, the gradient in the seawater temperature has a significant variation of nearly 30m depth whereas on horizontal direction, similar variation can be observed over a distance of 1000m or so. Also, convection is aided by wind forcing, in part because winds help to disrupt the viscous sub-layers at the sea surface, permitting more rapid transport of heat through the surface. However the action of wind on the surface layer enhances advection. To quantify the different energy fluxes exchanged through the ocean-atmosphere interface, an empirical formulae based on available observations were established (Coantic, 1974).

2.3.1 Radiative forcing

Radiative forcing over the sea surface comprises of incoming shortwave radiation Q_S , and outgoing longwave radiation Q_L . Q_L consists of infrared radiation (Black body radiation), Q_B , sensible heat Q_H , and latent heat Q_E .

Shortwave radiation Q_S

The largest term in the heat balance and the only one of global consequence that is positive is Q_S , the incoming shortwave radiation. The direct solar energy reaching the sea surface is centered in the band of wavelength from $0.5 \mu\text{m}$ - $1 \mu\text{m}$, between the visible and infrared portions of the electromagnetic spectrum. The actual amount of solar energy Σ_0 , integrated over the entire electromagnetic spectrum, that falls on a disk centered at the mean Earth-Sun distance and having a radius to the radius of the Earth is about 1390Wm^{-2} , and is called the *solar constant*. Since, the disk has an area of πR^2 , where R is the radius of the Earth, and the sphere has a surface area $4\pi R^2$, then the globally averaged value of solar energy falling on the Earth at the top of the atmosphere is just $S_0 = \Sigma_0/4$, or about 347.5Wm^{-2} .

Since the Earth is not a perfect absorber, the solar energy S_0 reaching the top of the atmosphere is immediately reflected back into space. A measure of the amount of energy reflected back into space is called the *albedo* (α). The amount of solar energy entering the top of the atmosphere is then $S = S_0 (1 - \alpha) = 222 \text{Wm}^{-2}$, where Earth's average *albedo* α is about 0.3. From this total amount, the clouds absorb a fraction of the energy before reaching the sea surface, and the remaining

is absorbed by atmospheric dust, ozone, and water vapor in the atmosphere. The result is a global average of about 150Wm^{-2} of solar energy that actually reaches the sea surface.

Infrared radiation Q_B

Earth radiates energy in the infrared portion of the spectrum, which results in a globally averaged loss of heat (Q_B) of about 50Wm^{-2} over the oceans. The amount of heat radiates from the sea surface in this fashion can be estimated from the Stefan-Boltzmann relation;

$$Q_B = e_m \sigma_B (T_s^4 - T_{ref}^4)$$

where, e_m is *emissivity* of the sea surface, σ_B is Stefan-Boltzmann constant, T_s is Surface temperature, and T_{ref} is characteristic radiative temperature at cloud bottoms.

More often we express this temperature T_{ref} based on the air temperature T_a by using the relation:

$$T_{ref} = T_a - \Delta T_{at}$$

where, ΔT_{at} is the difference in temperature between the cloud bottom and the oceanic atmospheric layer.

Sensible heat flux Q_H

Normally the ocean and atmosphere are at different temperatures, there will be a flux of heat between them in order to attain a state of thermal equilibrium. This

heat flux is called sensible heat, or conductive heat flux (Q_H). This heat flux corresponds to a loss or gain of energy by the sea, depending on the sign of the temperature difference ($T_s - T_a$). The physical method by which the heat is transferred between the atmosphere and ocean is quite complicated and depends on the temperature difference, relative humidity, wind speed, and a number of other environmental parameters. It is possible to gain a simple understanding of heat transfer process between ocean and atmosphere by considering the temperature gradient denoted by $\frac{\partial T}{\partial z}$, where T is temperature. We can anticipate that, in the absence of other factors, a gradient such as this would result in diffusion of the property T in the directions of decreasing T . As the gradient increases or decreases, it is expected the diffusive flux of T would increase or decrease correspondingly. We can state in this case the flux of T is proportional to the gradient of T , or $F_c = -\kappa \frac{\partial T}{\partial z}$, where the minus sign denotes the fact that the flux is in the opposite direction to the gradient, and the constant of proportionality ' κ ' known as the diffusivity. Diverse formulae used operationally are derived from different meteorological parameters. For example, citing the semi-empirical form of Coantic, (1974):

$$Q_H = \rho_a C_p C_H (T_a - T_s)$$

where, ρ_a is air density, C_p is the specific heat capacity at constant pressure, and C_H is heat transfer coefficient.

Latent heat flux Q_L

Since the atmosphere directly above the ocean is usually not saturated with moisture (i.e., the relative humidity <100%), there will be a tendency for evaporation from the sea surface in order to increase the moisture content of air. The energy required for evaporation is called latent heat of evaporation. Normally this energy is taken from the ocean surface and thus it consequently cools the sea surface; this amount of heat energy can be calculated by using the formula given below.

$$Q_L = \rho_v \mathcal{L} C_e (P_s - P_a)/P_a$$

where, ρ_v is density of water vapor, \mathcal{L} is latent heat of vaporization, C_e is evaporation coefficient, P_s and P_a are vapor pressures at temperature T_s and T_a .

Advective heat Q_V

Ocean cannot transport any net heat on a globally averaged basis, but advective heat fluxes between ocean basins or within a basin are quite possible. If the ocean is truly in thermal equilibrium and we neglect the geothermal heating (benthic heating), then we can write that

$$Q_{SURF} + Q_V = 0,$$

where, Q_V is the advective heat transport by the ocean. Since Q_{SURF} represents a flux of heat through the sea surface, and Q_V represents an internal flux of heat through the ocean, integral over a region of ocean to find that

$$\int_{\lambda_0}^{\lambda_1} \int_{\Phi_0}^{\Phi_1} Q_{SURF} d\lambda d\Phi = - \int_{\lambda_0}^{\lambda_1} \int_{-H}^0 Q_V d\lambda dz$$

This equation implies that if there is a net loss of heat through the surface of the ocean in some region, then there must be some net advection of heat into that region by the ocean circulation in order to maintain thermal equilibrium.

To generalize, the advective heat flux Q_V is proportional to both the velocity of the ocean circulation V and the temperature of the water; T . thus we can parameterize Q_V as

$$Q_V \approx VT = \rho CVT$$

where, ρ is seawater density and C is the heat capacity of seawater. Advective flux is a vector quantity, since it depends on both the magnitude and direction of V .

Heat balance Q_T

Shortwave radiation and latent heat loss are the dominant terms in the heat balance (Oberhuber, 1988; da Silva et al., 1994). The conservation of heat in a medium is called heat balance or heat budget. This quantifies source and sink terms of the heat in all directions. Generally, the heat budget of the oceanic component of the Earth can be written as

$$\downarrow Q_T = \downarrow Q_S + \uparrow Q_B + \downarrow Q_H + \uparrow Q_E + \vec{Q}_V + \uparrow Q_G$$

where, Q_T is net heat flux into the Earth (0Wm^{-2}), Q_S is direct solar input (150Wm^{-2}), Q_B is black body radiation (-50Wm^{-2}), Q_H is sensible heat loss (-10Wm^{-2}), Q_E is evaporative heat transfer (-90Wm^{-2}), Q_V is advective heat transfer (0Wm^{-2}), and Q_G is geothermal heating ($\sim 10^{-2}\text{Wm}^{-2}$).

These are the major terms with approximate global average values are given inside the parentheses. It is assumed in this formulation that the Earth is presently in thermal equilibrium: the heat lost equals the heat gained. If these are indeed a global warming (or global cooling) underway, then Q_T is not zero; however, nearly all contemporary attempts to deduce a value for Q_T yields a result that smaller than the errors in the determination. Thus, now $Q_T = 0$ to within our ability to measure it. The terms in the right side are individually somewhat known on a global average; with arrow headed upward, implying a net heat gain by the Earth and down headed arrow denotes a net heat loss. The advective heat transfer, Q_V , must equal to zero on a global average basis since the ocean cannot, on a net basis, create any heat by advection. The geothermal heating term, Q_G , is small enough to be considered and negligible with respect of the other terms, but it may have a major impact on the circulation of the deep sea, where the direct heat flux from the sea surface is small.

2.3.2. Wind forcing

The momentum transferred by sea surface winds to ocean surface influence the upper ocean properties such as currents, temperature/salinity to change via a mechanism called wind stirring, this impact also felt on the evolution of biology and bio-geochemical processes. Generally surface winds are represented by wind stress and empirically given as;

$$\tau^s = \rho_a C_D |w| w$$

where, ρ_a is air density, C_D the drag coefficient and W sea surface wind represented as vector.

Breaking waves

Large scale breaking of waves evidenced at the surface by white-capping and surface foam disrupts the ocean's cool skin. Small scale breaking, which has no visible signature, also disrupts the ocean's cool skin. Turbulence observations in the surface layer under a variety of conditions have indicated that at times (generally lower winds and simpler wave states) the turbulence dissipation rate (and presumably other turbulence quantities including fluxes) behave in accord with simple wall-layer scaling and is in this way similar to the atmospheric surface layer. However, under higher winds, and perhaps more complicated wave states, turbulence dissipation rates greatly exceed those predicted by wall-layer scaling. This is a problem of great importance in determining both transfer rates across the air-sea interface to the mixed layer below and the evolution of the mixed layer itself. It is at times when turbulence is most intense that most of the air-sea transfers and most of the mixed layer modification occur.

Langmuir circulation

The Langmuir circulations are coherent structure within the mixed layer that produces counter-rotating vortices with axes aligned parallel to the wind. Their surface signature is familiar as windrows: lines of bubbles and surface debris aligned with the wind that marks the convergence zones between the vortices.

These convergence zones enhance gas exchange rates with the atmosphere. Langmuir circulations appear to be intimately related to the Stokes drift, a small net current parallel to the direction of wave propagation, generated by wave motions. Stokes drift is concentrated at the surface and is thus vertically sheared. Small perturbations in the wind-driven surface current generate vertical vorticity, which is tilted toward the horizontal (downwind) direction by the shear of the Stokes drift. It is the convergence associated with these vortices that concentrates the wind-driven surface current into jets. Langmuir cells thus grow by a process of positive feedback. Ongoing acceleration of the surface current by the wind, together with convergence of the surface current by the Langmuir cells, provides a continuous source of coherent vertical vorticity. Maximum observed velocities are located well below the sea surface but also well above the mixed layer base. Langmuir circulations are capable of rapidly moving fluid vertically, thereby enhancing and advecting the turbulence necessary to mix the weak, near-surface stratification, which forms in response to daytime heating. However, this mechanism does not seem to contribute significantly to mixing the base of the deeper mixed layer, which is influenced more by storms and strong cooling events. In contrast, penetration of the deep mixed layer base during convection (driven by the conversion of potential energy of dense fluid plumes created by surface cooling/evaporation to kinetic energy and turbulence) is believed to be an important means of deepening the mixed layer.

Wind-Driven shear

Wind-driven shear erodes the thermocline at the mixed layer base. Wind-driven currents often veer with depth due to planetary rotation. Fluctuations in wind speed and direction result in persistent oscillations at near-inertial frequencies. Such oscillations are observed almost everywhere in the upper ocean, and dominate the horizontal velocity component of the inertial wave field. Because near-inertial waves dominate the vertical shear, they are believed to be important sources of mixing at the base of the mixed layer. In the upper ocean, near-inertial waves are generally assumed to be the result of wind forcing. Rapid diffusion of momentum through the mixed layer tends to concentrate shear at the mixed layer base. This concentration increases the probability of small-scale instability. The tendency toward instability is quantified by the Richardson number, $R_i = N^2 / S^2$, where $N^2 = -\left(\frac{g}{\rho}\right)\rho_z$, represents the stability of the water column, and shear, S , represents an energy source for instability. Small values of R_i ($<1/4$) are associated with Kelvin-Helmholtz instability. Through this instability, the inertial shear is concentrated into discrete vortices (Kelvin-Helmholtz billows) with axes aligned horizontally and perpendicular to the current. Ultimately, the billows overturn and generate small-scale turbulence and mixing. Some of the energy released by the instabilities propagates along the stratified layer as high frequency internal gravity waves. The mixing of fluid from below the mixed layer by inertial shear contributes to increasing the density of the mixed layer and to mixed layer deepening.

Temperature ramps

Another form of coherent structure in the upper ocean has been observed in both stable and unstable conditions. In the upper few meters temperature ramps, aligned with the wind and marked by horizontal temperature changes of 0.1K in 0.1m, indicate the upward transport of cool/warm fluid during stable/unstable conditions. This transport is driven by instability triggered by the wind and perhaps similar to the Kelvin-Helmholtz instability discussed above.

2.3.3. Solar penetrative profile.

Seawater properties will change under the accumulation of hydrosols (suspended particles, and yellow sediments), which attenuates the penetrated solar radiation. Normally the long-wave component of the solar radiation of the visible spectrum (300nm - 700nm) being absorbed in the top few centimeters and the remaining component of the radiation penetrates up to a depth of 20m – 40m. This characteristic depth of penetration may change depending on the constituents in the ocean waters.

At the depth h , the effect of solar radiation having penetrated the mass of water above is generally expressed as a function of radiative flux through the surface Φ_0 and of the extinction coefficient $\kappa_s(h)$. So, we write the solar radiation penetration to the depth h ;

$$S(h) = \Phi_0 \exp \left\{ - \int_0^h \kappa_s(z) dz \right\}$$

The extinction coefficient is often considered as constant. Then we simply have:

$$S(h) = \Phi_0 \exp(-\kappa_s h)$$

so, at depth h , the energy acquired from solar radiation is written:

$$R(h) = \frac{\partial S}{\partial z} \Big|_h = -\kappa_s \Phi_0 \exp(-\kappa_s h)$$

Attenuation of solar radiation in the water bodies is of great interest for both marine optics and biology. A reduction of solar radiation occurs by penetrating in the ocean water, caused by a mixture of particles of different composition, increases with decreasing wavelength (Kirth, 1985). Though the scattering depends weakly (for large particles) on wavelength, the effect of selectivity is largely caused by absorption.

It is known that, the useful wave band of light for photosynthesis is from 350nm to 700nm (Dera, 1992). As far as the suitability of light for photosynthesis is concerned, the end of the useful wave band is not irreversibly fixed in the literature, as the influence of light on photosynthesis is complicated. Often the useful range of light is taken to be the visible wave band, 400-700nm. Since ultraviolet is strongly absorbed in the water, the energy differences in the water depth ensuing from such shifts in the endpoints of the wave band concerned are small, around 1% (Dera, 1992). Accordingly, most of the Photo-synthetically Active Radiation (PAR) wave band sensors measure in the range 360nm-700nm.

2.3.4. Evapo-precipitation

Evaporation minus precipitation is the mass transfer quantity at the air-sea interface. The increase in one quantity will lead to decrease the other quantity. Here the evaporative term is an outgoing mass quantity, and the other is the condensation term, which is entering as fresh water at the air-sea interface. Outgoing mass term (evaporation) induces instability in the upper ocean by increasing the density. Thereby it makes a shift in halocline profile. If this discontinuity is not balanced by thermal shift, a diurnal pycnocline starts forming between the upper layer and the permanent thermocline or halocline. On the other hand the incoming fresh water mass makes the upper ocean to a less dens and hence it becomes more stable. A temporary thermocline can be seen in the form of an inversion to the normal profile. Rainfall on the sea surface can catalyze several important processes that act to both accentuate and reduce upper ocean mixing. Drops falling on the surface disrupt the viscous boundary layer, and may carry air into the water by forming bubbles. Rain is commonly said to 'knock down the seas.' The evidence for this is the reduction in breaking wave intensity and white capping at the sea surface. Smaller waves (<20cm wavelength) may be damped by surface turbulence as heavy rainfall acts to transport momentum vertically, causing drag on the waves. The reduced roughness of the small-scale waves reduces the probability of the waves exciting flow separation on the crests of the long waves, and hence reduces the tendency of the long waves to break. While storm winds generate intense turbulence near the surface, associated rainfall can confine this turbulence to the upper few meters, effectively insulating the water

below from surface forcing. This is due to the low density of fresh rainwater relative to the saltier ocean water due to evaporation. Turbulence must work against gravity to mix the surface water downward, and turbulence mixing is therefore suppressed. So long as vertical mixing is inhibited, fluid heated during the day will be trapped near the sea surface. Preexisting turbulence below the surface will continue to mix fluid in the absence of direct surface forcing, until it decays due to viscous dissipation plus mixing, typically over the time scale of a buoyancy period, N^{-1} .

2.4. Basic Mixing Mechanism

Two types of physical mechanisms are governing the evolution of marine mixed layer; namely the *radiative mixing* and the *wind mixing*.

2.4.1 Radiative mixing

Solar heating has a profound effect on the depth of convection because it is concentrated close to the surface. Half of the solar energy is absorbed in the top meter of the ocean. For several hours centered at noon each day at most locations around the world, the oceanic heat gain from the sun is more than double the loss to the atmosphere. Late evening and before noon of the next day sea surface cools and this cold dense fluid, which later sink to a depth determined by the local stratification in a convective process. Cooling occurs almost every night and sometimes during daytime in association with local weather systems such as cold air outbreaks from continental landmasses. Convection may also be caused by an

excess of evaporation over precipitation, which increases salinity, and hence density, at the surface. Winds aid convection by a variety of mechanism, which agitates the sea surface, thereby disrupting the viscous sub-layer and permitting rapid transfer of heat through the surface. Convection in the ocean is analogous to that found in the daytime atmosphere boundary layers, which are heated from below. Retrospective studies of atmospheric convection have helped in understanding the ocean's behavior. The depth of convection is then less than one meter, regardless, of the depth of the turbocline (where the vertical gradient of turbulence is large), the later normally being much more than a-meter. At night, the heat loss to the atmosphere is supplied convectively from heat storage during the day and, in the winter season, during earlier days. The depth of convection then nearly reaches the turbocline defining the bottom of the mixed layer. Surface tension and viscous forces initially prevent dense, surface fluid parcels from sinking. Once the fluid becomes sufficiently dense, however, these forces are overcome and fluid parcel sinks - this process is called *convective plumes*. The relative motions of the plumes help to generate small-scale turbulence, resulting in a turbulent field encompassing a range of scales from the depth of the mixed layer. The depth of convection is limited by the local thermocline. Mixing due to penetrative convection in to the thermocline represents another source of cooling of the mixed layer above. Within the convective layer, there is an approximate balance between buoyant production of turbulent kinetic energy and viscous dissipation.

At the top of the convective layer in which the fluid parcel/sea water vertical motion takes place due to density variation (Fig. 2.2). Convective process takes place when the seawater instability occurs due to solar heating and action of wind at the surface. It is embedded in the mixed layer, which is conventionally turbulent. The bottom of the mixed layer is defined by the turbocline (the layer in which the turbulent process occurs) below which turbulence is intermittent and an average very much weaker. The diurnal (the hourly variation) pycnocline lies between the turbocline and the top of the seasonal pycnocline that extends down to the top of the permanent pycnocline. The diurnal pycnocline disappears every night and the seasonal pycnocline every

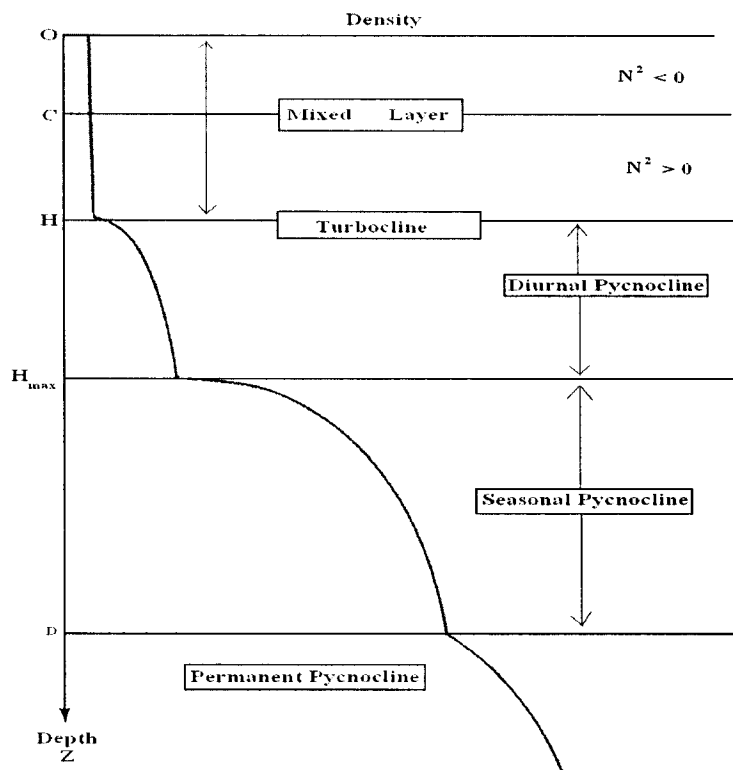


Fig. 2.2. A typical structure of the layers in the upper ocean defined based on density profile. The mixed layer defined here with uniform density values. Pycnocline region is divided according to the nature of persistence, namely diurnal pycnocline, seasonal pycnocline, and permanent pycnocline. (Adopted from Woods and Barkmann, 1986).

winter; the permanent pycnocline is always present. The water column is statically unstable (Brunt-Vaisala frequency N is negative) in the convective layer ($0 < Z < C$) and statically stable ($N^2 > 0$) in the rest of the mixed layer ($C < Z < H$). In the diurnal pycnocline ($H < Z < H_{max}$), the seasonal pycnocline ($H_{max} < Z < D$) and the permanent pycnocline ($Z > D$) the water masses are statically stable ($N^2 > 0$).

2.4.2. Wind mixing

Convection is aided by wind forcing because winds help to disrupt the viscous sub-layer at the sea surface by permitting rapid transport of heat. Atmospheric forcing of the upper-Ocean Boundary Layer (OBL) plays a fundamental role in regulating the sea surface temperature of the world's ocean (Eric et al., 2000). The most direct influence of the atmosphere is through surface fluxes of latent and sensible heat. During conditions of strong surface heat loss and weak forcing, the Ocean boundary layer behaves much like a well-mixed, convective boundary layer with turbulent fluxes that are in agreement with Monin-Obukhov similarity theory near the surface and a mixed layer structure that scales with the surface buoyancy flux (Shay and Gregg, 1986; Lombardo and Gregg, 1989). Often however, upper Ocean mixing is driven by wind and surface wave forcing, with entrainment flux at the mixed layer base dominating the Ocean boundary layer heat budget and the surface heat flux having a secondary role. Therefore, the Ocean boundary layer behaves more like a stratified boundary layer and cannot be easily described through classical boundary layer theory (Mahrt, 1999). Build up of momentum in the Ocean boundary layer through inertial resonance has been

well documented through observation and one-dimensional modeling studies (Crawford and Large, 1996; Large and Crawford, 1995). What has been thoroughly explained is how the upper ocean currents create and interact with turbulence and the stratified pycnocline at the boundary layer base. A schematic diagram, figure 2.3, shows the pathways that wind energy follows in driving inertial currents and turbulence. In the Ocean boundary layer, energy provided by

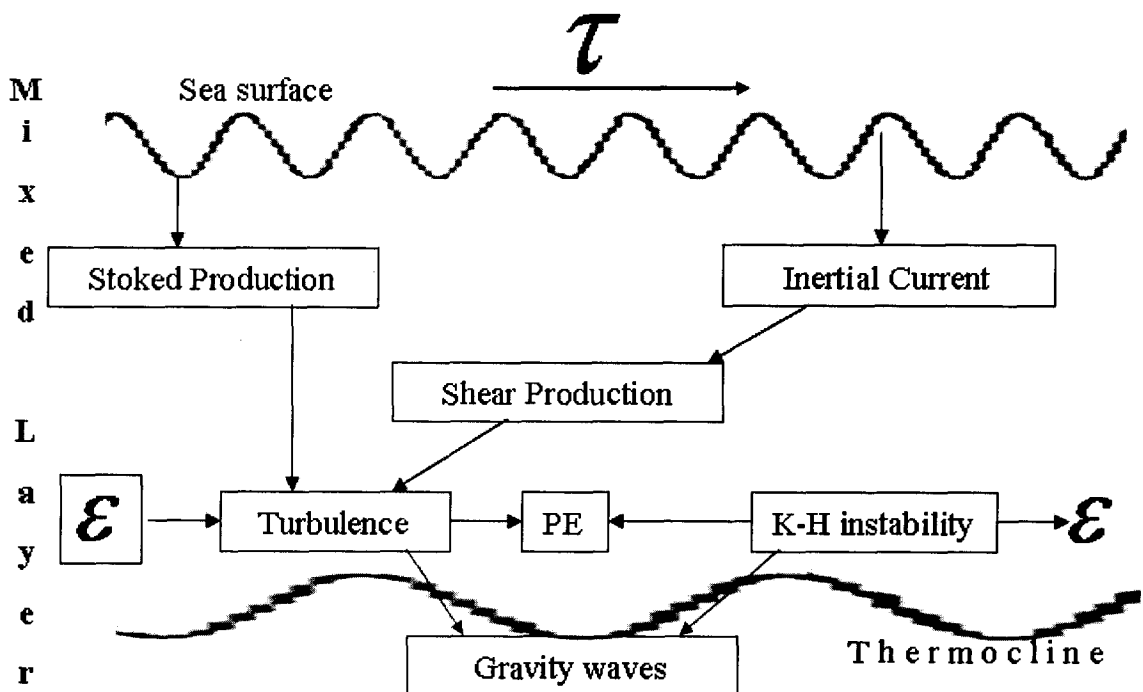


Fig. 2.3: The schematic diagram of wind force mixing in marine mixed layer. (After Eric et al., 2000)

the wind is partitioned between the mean current and turbulence generated by shear production and wave-current interaction (Stokes production). Some fraction of this energy is removed through turbulent dissipation, ϵ . Another portion goes into vertical mixing of thermocline water, thereby reducing the Ocean boundary layer temperature and increasing wave energy is generated at the mixed layer base through the shear of the mean inertial current. Energy from this process is also

used to mix thermocline water and is dissipated through friction and internal wave propagation.

2.5 Mixed-Layer Models

Given the inputs of heat, fresh water, and momentum from the atmosphere, a one-dimensional mixed layer model predicts the depth of the mixed layer and in some models the shape of the mixed layer base as a function of time. There are three basic families of mixed layer models: the “bulk Turbulent Kinetic Energy (TKE)” models, the “shear instability” models, and the “turbulent closure” models (Martin, 1985, 1986; Niiler and Kraus, 1977). The assumed physical mechanisms by which entrainment occurs differ fundamentally among the three families, but all are reasonably successful at predicting the observed depth of the mixed layer.

Integrated TKE, or “Bulk”, models

The so-called bulk turbulent kinetic energy model, initially formulated by Kraus and Turner, (1967), treats mixing based on a budget for the integrated turbulent kinetic energy of the surface ocean. A fundamental assumption of this model is that the mixed layer is completely homogeneous in the various state variables (temperature, salinity, surface current, turbulent kinetic energy, solutes, etc.). This assumption appears to be well founded in most parts of the surface ocean (Price et al., 1986; Martin, 1986). A heat balance is constructed which accounts for exchange with the atmosphere and fluxes by radiative transfer, and cooling caused

by entrainment of colder water from below (as the mixed layer depth, h , changes with time):

$$h \frac{dT_s}{dt} = \lambda \frac{dh}{dt} \Delta T - \frac{1}{\rho C_p} (Q_I - Q_{blue,l} e^{-\beta z} - Q_B - L_V E - H) \quad (1)$$

where,

$$\lambda = 0, \text{ if } f(dh, dt) < 0$$

and

$$\lambda = 1, \text{ if } \frac{dh}{dt} > 0$$

T_s is the sea surface temperature, and ΔT is the temperature difference across the mixed layer base.

The two-degree of freedom in equation (1) are sea surface temperature and the depth of the mixed layer; another independent equation is necessary to close the system. The requisite constraint is based on a kinetic energy budget. The source of turbulent kinetic energy is the wind stress (a scaling coefficient, m , times the “friction velocity” of the wind, U_*^3) and the sink is dissipation (D). The residual kinetic energy (the difference between input and dissipation) is transformed into potential energy by mechanical mixing of cold water into the mixed layer (also, the average *TKE* of the mixed layer decreases as quieter water is entrained):

$$\frac{1}{2} \frac{dT_s}{dt} h^2 + \lambda \Delta T h \frac{dh}{dt} = m U_*^3 - D$$

Since (Kraus and Turner, 1967), many other workers have used models based on this formulation, and much of the work has centered on the dissipation of

turbulence (Stevenson, 1979). The generation and dissipation of turbulence is the greatest weakness of this type of model; in the case of dissipation in particular, the link between the model and the actual physics is weak. Some authors scale turbulent kinetic energy dissipation as a constant loss rate times the mixed layer depth (Kim, 1976; Niiler and Kraus, 1977). Others calculate the dissipation rate as a function of the total amount of mixed layer turbulent kinetic energy, the Coriolis parameter (Grawood, 1977) and/or the Monin-Obukhov length scale for turbulence (Gaspar, 1988). To simulate the mixed layer response to hurricanes, (Elsberry et al., 1976) used a parameterization for dissipation as a fraction of surface input of turbulent kinetic energy that increases with increasing mixed layer depth.

The other weakness of the bulk turbulent kinetic energy family of models is the generation of turbulent kinetic energy (calculated as a constant, m , times the wind stress). The value of m is “tuned” to fit the model predictions to observed data, and the best value for m tends to vary with location and conditions (ranging from 0.1 to 0.39 (Martin, 1985), 0.3 to 0.9 (Price et al., 1978) and 0.4 to 0.5 (Davis et al., 1981)). The instability of m and the uncertainty about turbulent kinetic energy dissipation certainly detract from the predictive ability of the bulk turbulent kinetic energy type model.

Shear Instability models

Another potential source of turbulent kinetic energy, not considered in the original Kraus-Turner formulation, is the generation of turbulence by current shear. Although the only source of energy to the mixed layer is input by wind, in the shear models this energy is assumed to generate mean flow rather than turbulent energy, and the flow is converted to turbulence at the base of the mixed layer (Gargett et al., 1979).

Formulation

Mixing in a stratified fluid is governed by the gradient of velocity with depth (shear) and the density stratification (Ellison and Turner, 1959). The relevant non-dimensional parameter is calculated as the ratio so these quantities (from Price et al., 1986),

$$Rg = \frac{g \frac{\partial \rho}{\partial z}}{\rho_0 \left(\frac{\partial u}{\partial z} \right)^2} \text{ and is called the gradient Richardson number.}$$

The Richardson number used in most mixed layer models is defined somewhat differently. The mixed layer is viewed as a slab, with uniform velocity and density. Instead of the differential quantities $\frac{\partial \rho}{\partial z}$ and $\frac{\partial u}{\partial z}$, the differences $\Delta \rho / h$ and $\Delta u / h$ are used, where $\Delta \rho$ and Δu are the changes in density and velocity across the mixed layer base. The length scale is the thickness of the mixed layer, h , rather than a scale associated with the thickness of the mixed layer base. The

dimensionless number thus defined, $R_b = \frac{g\Delta\rho h}{\rho_0(\Delta u)^2}$ is called the bulk Richardson number (Pollard et al., 1973; Price et al., 1986). In the shear models, mixing is assumed to begin when R_b falls below a critical value, and water is entrained until R_b reaches the critical value once again. Models based on the bulk Richardson number predict mixed layer variations quite well, and the only potential “tunable” parameter is the critical Richardson number, which appears to be stable throughout a variety of locations and chemical conditions (Price et al., 1978; Price et al., 1986). Theoretical justification for use of bulk, rather than the gradient, Richardson number for these models is still a matter of discussion (Pollard et al., 1973; Price et al., 1978).

The shear instability model of (Price et al., 1986) uses both R_b and R_g to determine mixing. The model is used to simulate detailed diurnal fluctuations in the mixed layer depth and current profiles from the subtropical Pacific. In the model, the heat fluxes (except penetrating solar radiation) and the wind stress are applied to the mixed layer. The bulk Richardson number at the base of the surface box is calculated, and if the shear is greater than the density stratification necessary to support it ($R_b < 0.65$), then the properties of the two adjacent boxes are averaged (the boxes are mixed). This process continues downward until $R_b > 0.65$. The mixed layer is considered homogeneous for momentum and density, as it is in the bulk turbulent kinetic energy formulations considered above. The density transition at the mixed layer base is smoothed using the gradient Richardson number. If R_g between two adjacent boxes is smaller than a critical value ($R_g <$

0.25), the adjacent boxes are partially mixed until the shear becomes sub-critical again, and the process is repeated until R_g is greater than or equal to the critical value throughout the water column. Thus, there is a region of partial mixing below the completely mixed zone. The model also includes convective entrainment driven by surface cooling.

Behaviour

A model in which the generation of turbulence scales with the Richardson number behaves differently from a model, which scales the turbulence directly with wind stress (Price et al., 1978). This is largely because of the rotation of an inertial current to the surface of the earth (the Coriolis effect). In the presence of steady, non-rotating wind forcing, a natural limit is imposed on the current velocity by the “*inertial*” rotational frequency (the value for which varies as a function of latitude). The advantage of scaling entrainment to the current velocity, as opposed to scaling with the wind stress directly, is that the current velocity is limited by the rotational frequency, and no artificial dissipation term is required to limit the steady-state mixed layer. (With constant wind forcing and no dissipation term, a turbulent kinetic energy model would entrain forever). Treatment of dissipation is one of the major weaknesses in the turbulent kinetic energy model formulation. Also, the value of the critical R_b required to simulate oceanographic data using a shear instability mixed layer model is fairly constant throughout a range of climatic conditions (Price et al., 1978; Pollard et al., 1973; Price et al., 1986). This can be contrasted with the wind-scaling coefficient used in the turbulent kinetic

energy model, which must be tuned to simulate data from different locations or climatic regimes.

Turbulence closure models

The third family of upper ocean mixing models is the most general, the most complicated, and the most stringently founded in the theoretical and empirical properties of fluid turbulence. These are the “turbulence closure” models, first introduced into the mainstream oceanography literature by Mellor, 1973 (also Mellor and Yamada, 1974, 1982; Mellor and Durbin, 1975). Turbulence closure models were originally constructed for use in the atmospheric boundary layer. In the oceans, Mellor’s model is general enough to be applied to special cases like the equator, where the equatorial undercurrent produces regions of extremely high shear and to a system of estuarine circulation, spanning the benthic boundary layer, the highly stratified shear flow between the saline and fresh waters, and the surface boundary layer.

Formulations

The physical foundation for the turbulence closure models begins with the Reynold’s equations for momentum and heat (from Mellor and Yamada, 1974):

$$\frac{\partial U}{\partial t} + U \cdot \nabla U + f \times U = \nabla P - g\beta\theta + \nu \nabla^2 U \quad \text{and}$$

$$\frac{\partial \theta}{\partial t} + \nabla \cdot U\theta = \alpha \nabla^2 \theta$$

where, U is velocity, θ is temperature, f is Coriolis parameter, P is pressure, g is the acceleration due to gravity, ν is the molecular viscosity, α is the thermal diffusivity, and β is the thermal expansion coefficient. The equations for the mean flow and temperature can be found by decomposing the total velocity and temperature fields into mean and fluctuating components and averaging:

$$\frac{\partial U}{\partial t} + U \cdot \nabla U + f \times U = \nabla p - g\beta\theta + \nu \nabla^2 U - \nabla \cdot \overline{u u} \quad \text{and}$$

$$\frac{\partial \theta}{\partial t} + \nabla \cdot U \theta = \alpha \nabla^2 \theta - \nabla \cdot \overline{u \theta}$$

the terms $\overline{u u}$ and $\overline{u \theta}$ represent the effect of the turbulent fluctuations on the mean velocity and temperature (the Reynolds stress and “*eddy diffusion*”). Finding analytical expressions for these terms is the problem at the heart of the turbulence closure models.

Derivation of expressions for these terms begins with these two sets of equations, and incorporates several empirical simplifying relationships based on laboratory data (Mellor and Yamada, 1974). The salient point to understand about the derivation is that the solutions contain several empirical constants, which are fit to laboratory data from neutral (de-stratified) flows. Mellor and Yamada, (1982) showed the surprising result that the model, using these constants, is also able to predict laboratory data for stratified flow, flow in a pipe, and flow over a curved surface. Some of the terms in the equations also require a constant with units of length to maintain dimensional homogeneity. Mellor assumes that the length scales are all proportional to a single “mixing length scale” (l). This assumption,

and the derivation of a number for l , is considered a weak link in the turbulent closure scheme. The choice of l is crucial; the levels 2 and 2.5 models supply eddy diffusion coefficients that scale directly to l .

The mixing coefficient predicted by the model turns out to be a function of the local gradient Richardson number (Niiler and Kraus, 1977; Mellor and Durbin, 1975); above $R_g = 0.23$, no mixing at all is predicted. This is similar to the Price model, in which mixing takes place until a critical $R_g > 0.25$ is attained. The level 2.5 model has been used in a global ocean model that focuses on the surface ocean and the sea surface temperature (Rosati and Miyakoda, 1988).

Behaviour

The turbulence closure models are more difficult to understand in an intuitive way than the other models. Insight can be gained by comparing the behavior of the model with those of the bulk turbulent kinetic energy and shear models described above.

One obvious distinction is the degree of mixing in the turbulence closure model mixed layer. Whereas the other formulations assume homogeneity of all properties within the mixed layer, the turbulence models predict high but finite mixing coefficients within this zone. Under conditions of deep convective mixing, the “*bulk*” assumption (that the mixed layer is completely homogeneous in all properties) is probably inadequate, but under conditions of shallower, wind-driven

mixing, the “*bulk*” approximation may be closer to reality than the output of the turbulence models (Martin, 1986).

The fundamental distinction between the bulk and shear models presented earlier is the source of the turbulent energy for entrainment: from wind stress directly or from current shear. The main source of entrainment energy in the turbulence closure models is difficult to judge from first principles. For the primary source of turbulence to be generation at the surface, the rate of transport of turbulent energy through the mixed layer must be greater than the rate of generation of turbulence by shear at the mixed layer base. In the level-2 model, transport of turbulence does not occur; all turbulence is dissipated locally. Numerical experiments using level-2.5 and higher have shown that the transport flux of turbulent energy from the surface zone in these models is also small relative to the generation of turbulence by shear (Klein and Coantic, 1981; Martin, 1986). Thus the turbulence closure models appear to function primarily as shear instability models.

Computational efficiency

Martin, 1986 also compared the computation time required by the different types of models. As written, the bulk model is the fastest. The Price shear-driven model is significantly slower, mainly because of calculations involved in maintenance of the partially mixed zone beneath the mixed layer (based on R_g , explained above), which can be eliminated (Archer et al., 1993). The turbulence models are the slowest, because of their complexity and the higher temporal and spatial

resolution required. Turbulence models are the most suitable for use in a vectorized or parallel computer architecture, which would reduce somewhat the computation disparity between the model types.

2.6 Summary

Mixed layer is a region of stable stratification that partially insulates the upper ocean from the ocean interior. Heat, momentum, and chemical species exchanged between the atmosphere and the ocean interior must traverse the centimeters thick cool skin at the very surface, the surface layer, and the mixed layer to modify the stable layer below. These vertical transports are governed by a combination of processes, including those that affect only the surface itself (rainfall, breaking surface gravity waves), those that communicate directly from the surface throughout the entire mixed layer (convective plumes) or a good portion of it (Langmuir circulations) and also those processes that are forced at the surface but have effects concentrated at the mixed-layer base (inertia shear, Kelvin-Helmholtz instability, propagating internal gravity waves). Several of these processes are represented in schematic form in figure 2.4.

All of the models can adequately predict observed fluctuations in the mixed layer depth of the ocean, under most conditions. There may be situations (for example, the equatorial undercurrent, or regions near a western boundary current), which are more complicated and these will probably be better handled by the turbulence closure scheme. A criterion for comparison of the model formulations is the

quantity and stability of the empirical parameters required for oceanic simulation. The bulk turbulent kinetic energy models appear to be weakest in this respect in that the coefficient which predicts turbulent kinetic energy flux into

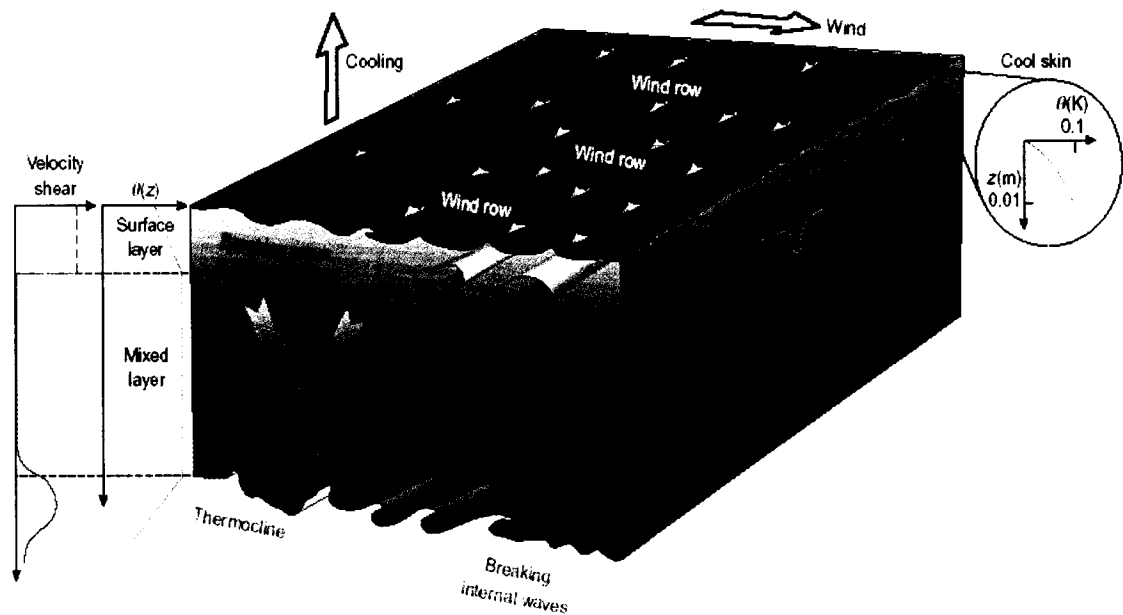


Fig. 2.4: Contributors to mixing the upper ocean, courtesy to Moum and Symth, 2001: Diagram showing processes that have been identified by a wide range of observational techniques as important contributors to mixing the upper ocean in association with surface cooling and winds. The temperature (θ) profiles shown here have the adiabatic temperature (that due to compression of fluid parcels with depth) removed; this is termed potential temperature. The profile of velocity shear (vertical gradient of horizontal velocity) indicates no shear in the mixed layer and nonzero shear above. The form of the shear in the surface layer is a current area of research. Shear-induced turbulence near the surface may be responsible for temperature ramps observed from highly resolved horizontal measurements. Convective plumes and Langmuir circulations both act to redistribute fluid parcels vertically; during convection, they tend to move cool fluid downward. Wind-driven shear concentrated at the mixed-layer base (thermocline) may be sufficient to allow instabilities to grow, from which internal gravity waves propagate and turbulence is generated. At the surface, breaking waves inject bubbles and highly energetic turbulence beneath the sea surface and disrupt the ocean's cool skin, clearing a pathway for more rapid heat transfer into the ocean.

the mixed layer based on the wind stress seems to vary as a function of climatic conditions. The empirical parameters used by the shear instability models are the critical Richardson numbers R_b and R_g , which do not vary in this way (Price et al.,

1978). The constants in the turbulence closure models were determined from laboratory experiments, and appear to be adequate for oceanic use (Rosati and Miyakoda, 1988). The detailed comparisons of each model in terms its ability, to simulate the ocean state, is given by Martin, (1985; 1986). The latter study is an extension of the former, with the inclusion of the (Price et al., 1986) model and a turbulence closure scheme other than Mellor's (Therry and Lacarrere, 1983).

The conclusions are the following. First, the turbulence closure schemes are essentially Richardson number driven models, and the main differences among them (and the Price et al., 1986 model) are the exact value of the critical Richardson number at which mixing commences. Second, the bulk turbulent kinetic energy models do not attempt to simulate partial mixing at the base of the mixed layer, as do the Price model and the turbulence closure schemes. For this reason, the bulk turbulent kinetic energy model mixed layer base is unrealistic. Third, the turbulence models predict a greater gradient of momentum and density through the mixed layer than is observed (Price et al., 1986); apparently, some mechanism for mixing exists (such as Langmuir circulation) that is not included in the 1-Dimensional turbulence closure model formulation. Finally, under some circumstances, each of the models predicts mixed layer depths that deviate somewhat from the observed data.

Chapter III
**Spatiotemporal distribution of mixed
layer depth and forcing parameters**

3.1 Introduction

This chapter is anticipated to explain, the spatial and temporal distribution of monthly mixed layer depth and forcing parameters, which enhances its variability over the study region. As such there are many parameters involved in changing the mixed layer's physical and chemical properties. Few of them are chosen (namely wind speed, net heat gain, sea surface temperature, evaporation minus precipitation, and sea surface height), since they are available either from satellite platforms or re-analysis. Subsequent pages explain the spatiotemporal variability of forcing parameters and mixed layer depth.

3.2 Spatiotemporal Distribution of Mixed Layer Depth

Climatic mean monthly temperature and salinity profiles of Levitus, (1994) are used for the description of spatiotemporal distribution of mixed layer depth. These profiles are at $1^\circ \times 1^\circ$ (longitude x latitude) grids. Density profile is constructed by applying Gill, 1981 approximation on salinity and temperature fields at each depth; later mixed layer depth is estimated using the above density profile by adopting Levitus, (1982) criterion with the view that the mixed layer is the region just below the ocean surface where the temperature or density is approximately uniform. The depth where the density is greater than the surface value by 0.125kg m^{-3} is defined as mixed layer depth. Henceforth for estimating the mixed layer depth this criterion is adopted. Validation of this method is given in appendix.

Climatic monthly distribution of mixed layer depth is shown in figure 3.1. During the winter season almost the entire Indian subcontinent and enclosed ocean experiences cold weather condition. The Arabian Sea experiences augmented northeast monsoon effect in January with strengthening of winds (8ms^{-1}) off Somalia, and western Sri Lankan coast. In response to surface cooling, mixed layer depth deepens considerably over northern Arabian Sea through entrainment owing to convective mixing. Analysis of Rao et al., (1989; 1991) also showed wintertime, mixed layer depth is of the order of 100m. There is, however, little indication of such thick mixed layer in synoptic observations from Bay of Bengal. Instead, there is a fresh, surface layer caused by intense rainfall and river runoff from earlier in the year, and there can be temperature inversions across the layer. The resulting large density difference across the base of the mixed layer inhibits entrainment. Because of the heat input and following mixed layer stratification, the mixed layer depth in Arabian Sea shoals from March to May. June onwards, mixed layer depth starts deepening in association with strengthened monsoonal wind and decreased solar insolation due to cloud cover. The mixed layer depth deepens markedly in the interior of the Arabian Sea to more than 110m due to Ekman convergence (McCreary et al., 1993). The region of shallow mixed layer depth in May along the 10°N has intensified and broadened from 40m to 60m. As the monsoon ceases, mixed layer depth shoals from September to November attains minimum in November following an increasing maximum till February of the next year. Thus Arabian Sea experiences

bimodal oscillation of mixed layer depth, one during northeast monsoon (due to *convective mixing*) and the other during southwest monsoon (due to *wind mixing*).

Though the variations of mixed layer depth over Bay of Bengal is similar to Arabian Sea, the mixed layer depth variation in Bay of Bengal is less influenced by the winter monsoon. In May, the shallowing of mixed layer depth south of India (extends from 65°E to 90°E) and over west coast of India is found owing to Ekman pumping driven by positive wind stress curl (McCreary et al., 1993). In July, small changes that have occurred in Bay of Bengal are most visible in the structure of mixed layer depth, which shows further shallowing along the east coast of India and deepening along the eastern boundary of the bay. The northeast monsoon weakened considerably at this time, and most of the circulation in the northern ocean is remnants of flows that are generated earlier (McCreary et al., 1993).

Southern Indian Ocean is not covered by land, except eastern and western sides, and hence the upper ocean dynamics and the variability of mixed layer depth can be attributed to air-sea interaction and sub-surface processes. Two physical processes, both of which began in April and May, contribute to near-equatorial changes of mixed layer depth. One is local forcing by wind stress curl, a process that is strongest in the southwestern Bay of Bengal which forces mixed layer depth to shallow north of the wind axis (as in May) and to deepen south of it; in consisting with geostrophy

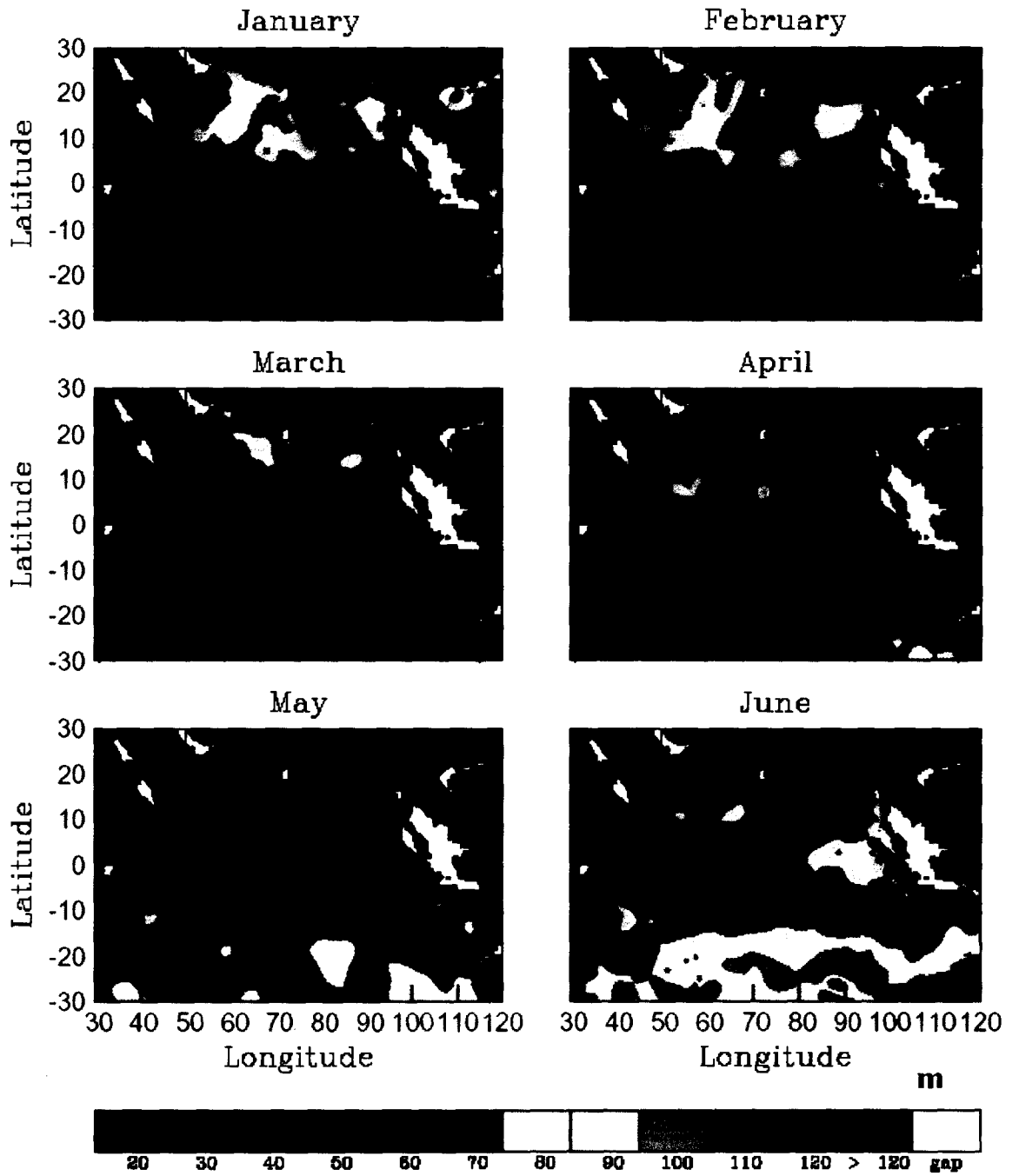


Fig. 3.1a: Spatial distribution of marine mixed layer depth, the units are in meters.

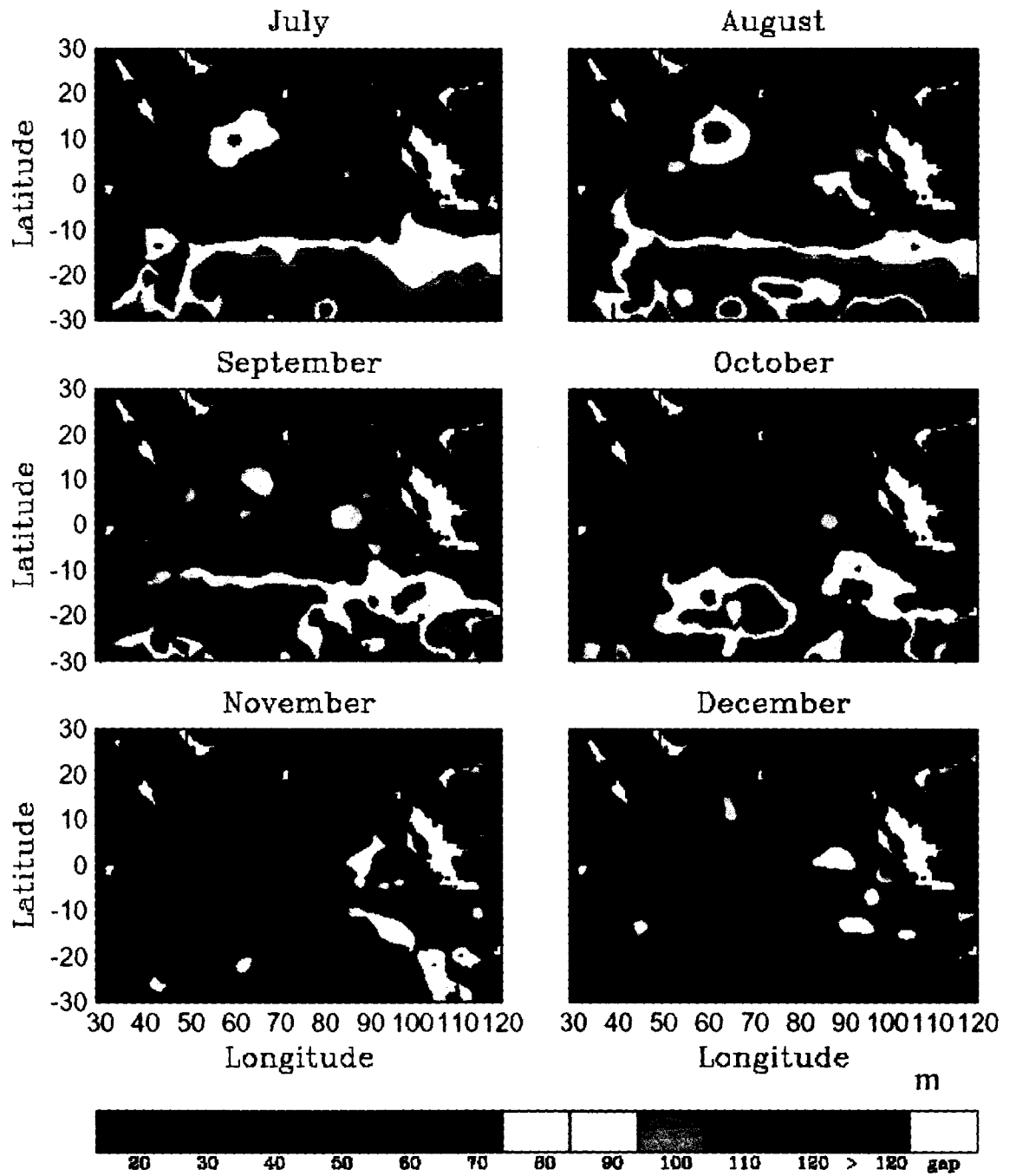


Fig. 3.1b: Continuation ...

an eastward current is generated in the region, and a westward current is produced along the southern portion of the region of deeper mixed layer depth. Similar to

Arabian Sea higher winds and deepening of mixed layer depth is observed during the southwest monsoon season. The other process is the westward propagation of the region of increased mixed layer depth (McCreary et al., 1993). The southwest monsoon collapses in October, and at that time the strongest winds anywhere in the northern ocean are westerly located near and just north of the equator between 60°E and 90°E. The north easterlies are not yet strong enough, nor have they been blowing enough, to modify the circulation in any obvious manner during northeast monsoon season (McCreary et al., 1993).

3.3. Spatiotemporal distribution of wind speed

ERS 1 / 2 scatterometer derived winds for the years 1990 – 2000 is used to produce mean monthly distribution of wind charts over the study region. Spatial distribution of wind speed and wind direction is shown in figure 3.2 on monthly basis. Over Arabian Sea winds are northerly during northeast monsoon and maximum winds higher than 6.5ms^{-1} are found during January over the Somali basin. This northerly wind reduces gradually till April with mean winds of 4ms^{-1} . At early stage of south west monsoon, reversal of wind pattern from northeasterly to southwesterly takes place and subsequently magnify to low-level Somali jet with average wind speed varies from 4ms^{-1} to 6ms^{-1} . This low-level Somali Jet system investigated in detail by Findlater, 1969. The jet system moves toward the African coast and shifts northward following the general advancement of the southeast trade winds. By May, the jet flows across the coastline, blocked by the highlands, and run parallel to them. This jet related activity of the surface wind

field and intense flow near the western boundary of the Indian Ocean is an important consequence for the oceanic response and current system. Synoptic observations further suggest that at the early stage of south west monsoon the Somali current retroflects just north of the equator, with part of the retroflected water re-circulate south of the equator to form a closed gyre, generally known as '*Southern Gyre*' (Bruce, 1973; Swallow et al., 1983). As the southwest monsoon advances from June to August, the wind speed get intensified, figure 3.2 shows maximum wind speed variation of 7ms^{-1} to 14ms^{-1} and peak in July. The transition season follows southwest monsoon with low wind speed of 3ms^{-1} during October and at end of the calendar year and the wind organizes into northerly with maximum winds of 8ms^{-1} .

Ocean basins of Indian subcontinent (AS and BOB) are identical over wind patterns during January with mean northerly winds of 3.5ms^{-1} and the southern central Bay of Bengal resembles with high winds of 6.5ms^{-1} . Till April steady and moderate winds of 3ms^{-1} exists over Bay of Bengal. At early stage of southwest monsoon reversal of wind pattern from northeasterly to southwesterly takes place and subsequently intensify to 7ms^{-1} in May. During southwest monsoon average wind intensify to 8ms^{-1} , which is $3\text{ms}^{-1} - 4\text{ms}^{-1}$ lesser than Arabian Sea. The transition season follows southwest monsoon with low wind speed of 3ms^{-1} during October and at the end of the calendar year, the wind organizes into northerly with maximum winds of 5ms^{-1} in December over southern central Bay of Bengal.

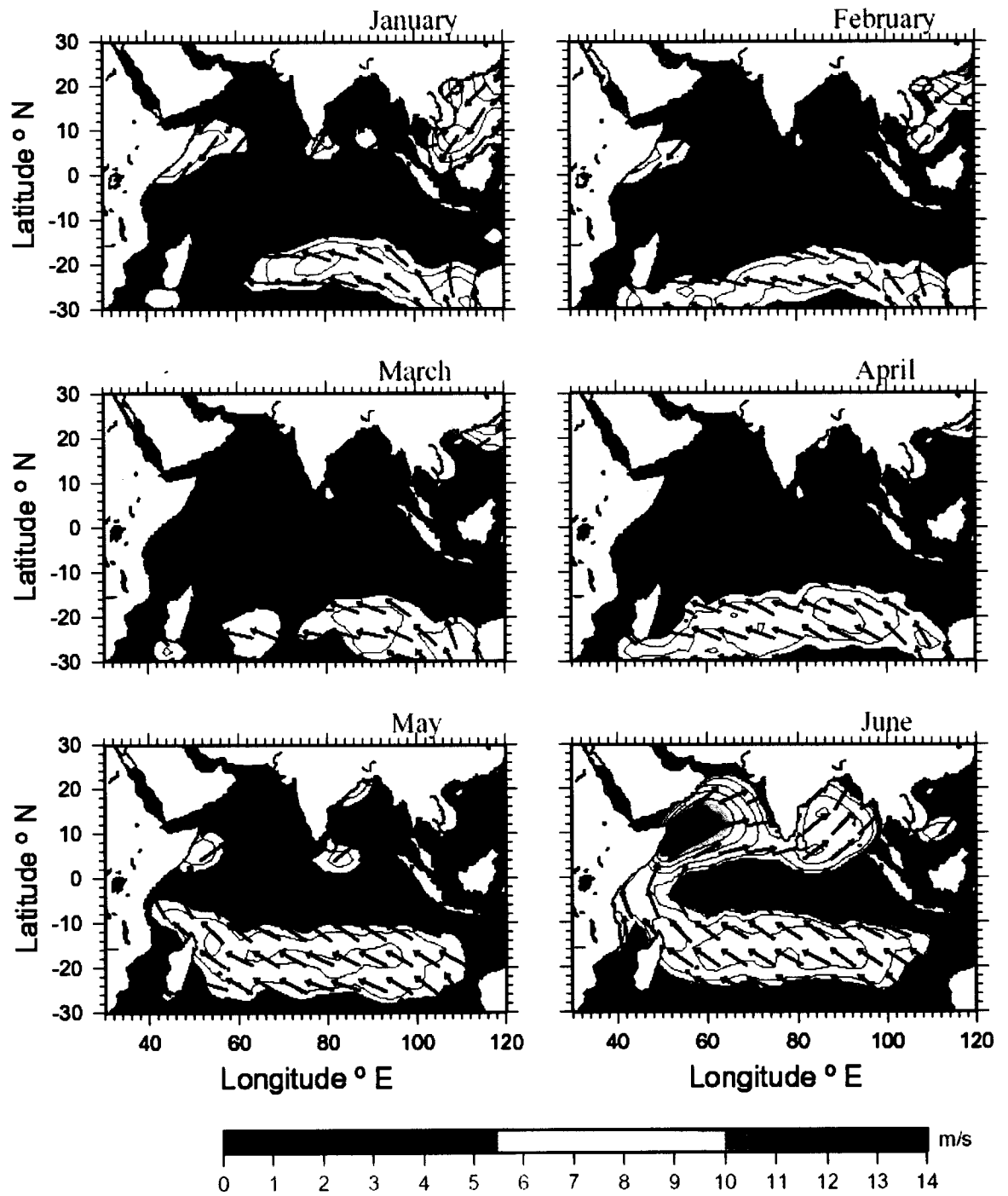


Fig. 3.2a: Mean monthly distribution of wind; the arrows of fixed length indicating the direction and color shade represents the wind magnitude.

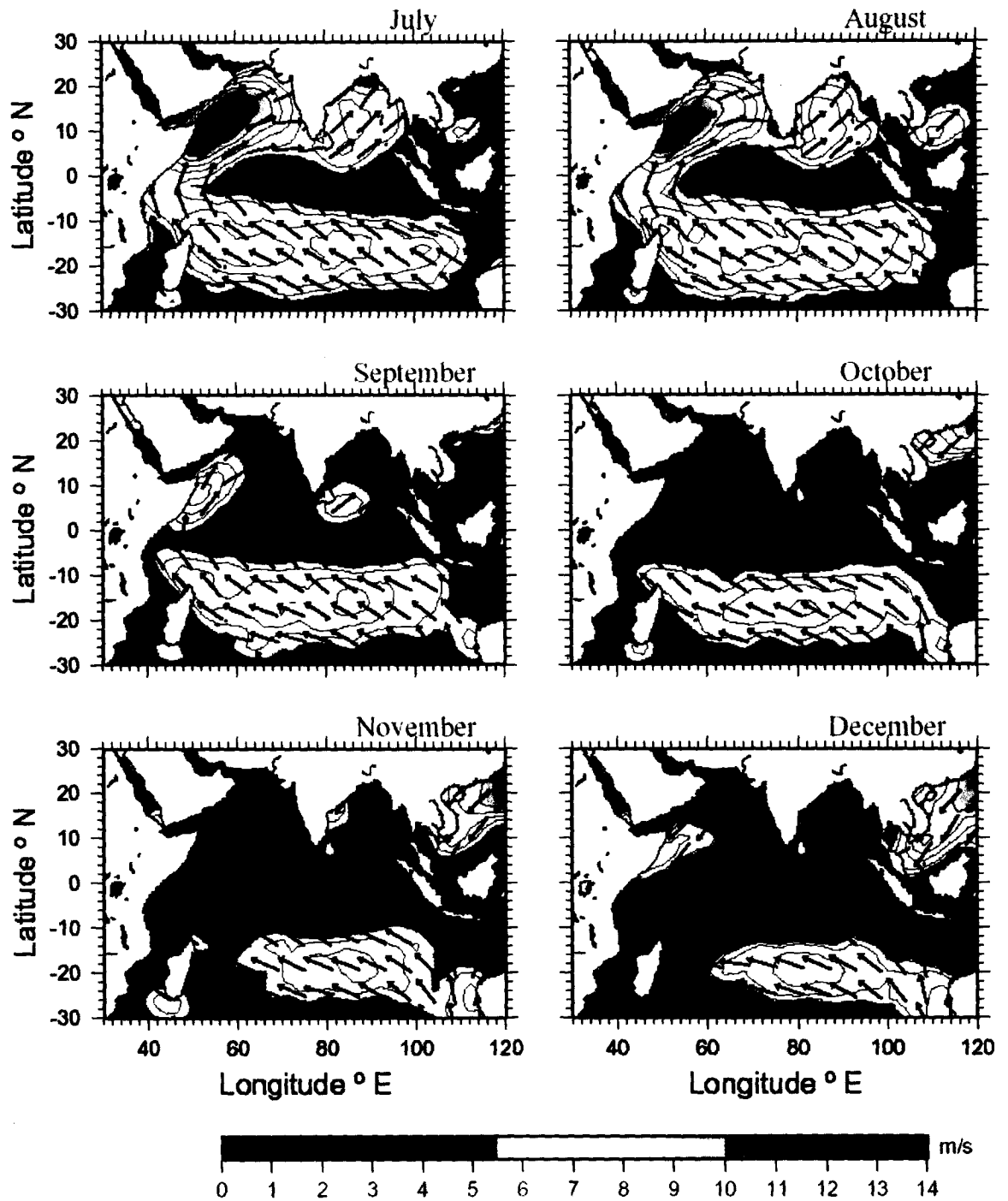


Fig. 3.2b: Continuation ...

The January chart shows a wintertime high-pressure zone over southern Asia. Northerly or northeasterly wind flow reaches across the northern Indian Ocean and convergence with the southeast trade winds at 20°S to 10°S. At this season the Tropical Indian Ocean (TIO) looks most like the other two oceans (Pacific and

Atlantic) in terms of surface wind patterns (Knox, 1987); two trade wind systems, each with a significant easterly component in much of the tropical oceans. As the year progresses the high pressure center over Asia weakens, the north east monsoon decay, Southern hemisphere high pressure center intensifies and moves northward, and the southeast trades penetrate further northward leading to the onset of south west monsoon. By July the southwest monsoon is fully develops. South easterlies from the southern hemisphere high pressure reach across the equator as southerlies or south westerlies. During the monsoon transition period wind becomes westerly and increases in strength over near-equatorial regions.

3.4 Spatiotemporal Distribution of Sea Surface Height anomaly

In the absence of the geoid (an equipotential surface that would be attained by motionless uniform ocean on a rotating earth) information obtaining about absolute sea surface height from altimeters to the required accuracy is not possible. Hence sea surface height variability alone can be studied by taking long-term time series observations. Hence the altimeter observations are always referred with respect to a long-term mean or with respect to a reference pass (Ali et al., 1998; Miller and Cheney, 1990). These variations are called sea surface height anomalies. Monthly mean sea surface height anomaly (here after sea surface height, SSH) derived from TOPEX (topography experiment) altimeter for the seven-year period (1992-1999) over the northern Indian Ocean has shown in figure 3.3.

A negative sea surface height described over Arabian Sea during winter season ranges from -20cm to -7cm. This low sea surface height anomaly indicates the presence of a cyclonic gyre covering the entire basin. The cyclonic/anti-cyclonic circulation patterns can be readily delineated from observations of sea surface height anomaly (Ali et al., 1998b). From February onwards the negative sea surface height high over Somalia region (-6cm) starts strengthening with the advent of the increasing temperature and substantial thermal expansion. Sea surface height over Arabian Sea starts increasing to positive values during the later period of March. During May and June, entire Arabian Sea experiences positive sea surface height with maximum value (~12 cm) at Somali coast. This may be due to the twin-gyre system, which dominates the Arabian Sea circulation at early stage of monsoon. Brown et al., (1980) also described the transition of a one-gyre system late in August. However, over the coastal regions, negative sea surface height found well before August.

The seas around southwest of India, sea surface height shows high positive value in January. This could be due to the strong north equatorial current near 70°E (Rao et al., 1991). Subsequently from February to April the positive sea surface height anomaly extends towards southwest, but with reduced intensity. The southwest spread in the sea surface height from January to April is due to northeasterly winds, similar pattern is also observed by Tapley et al., (1994) with TOPEX, altimeter data.

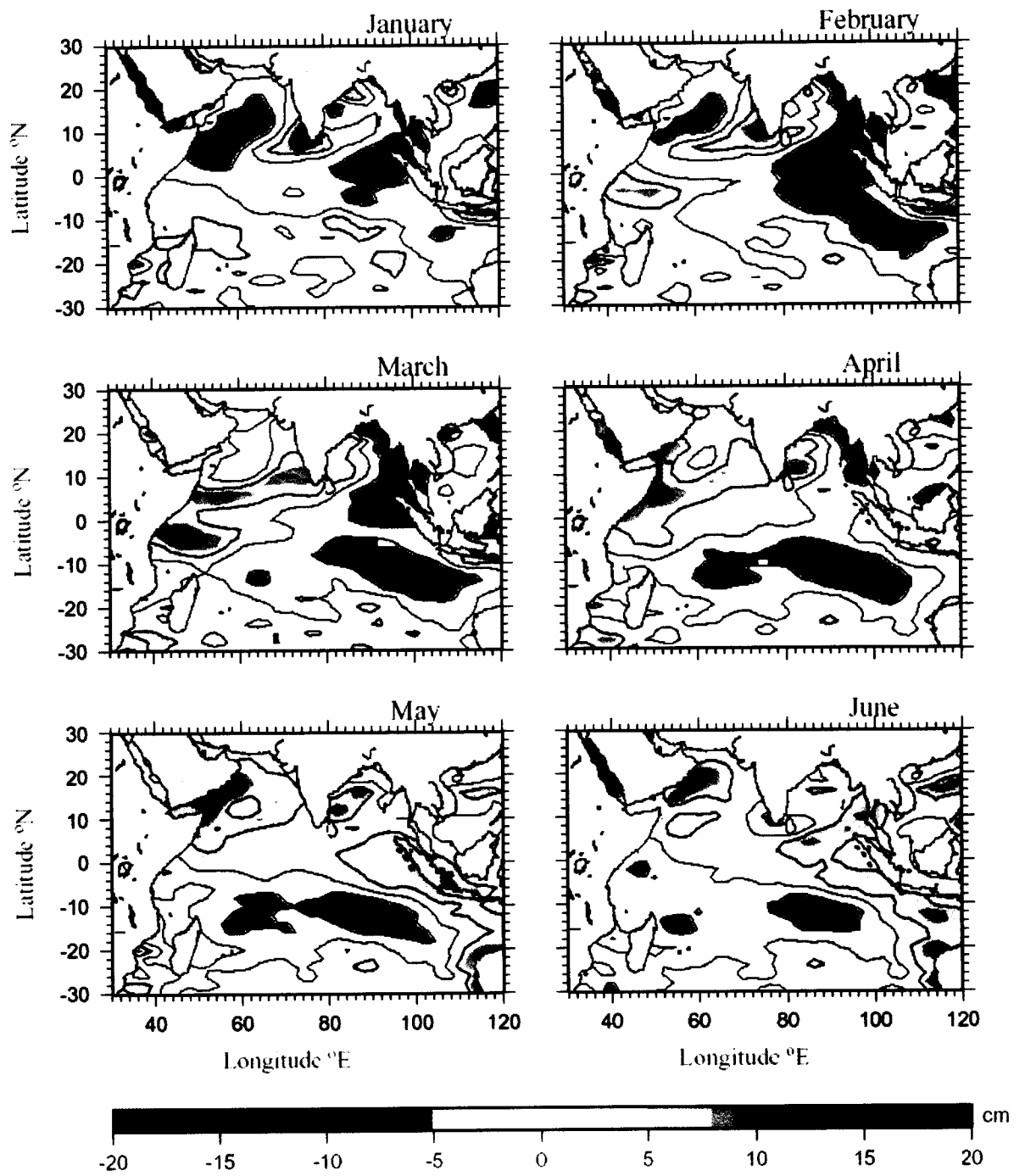


Fig. 3.3a: Monthly mean distribution of sea surface height anomaly.

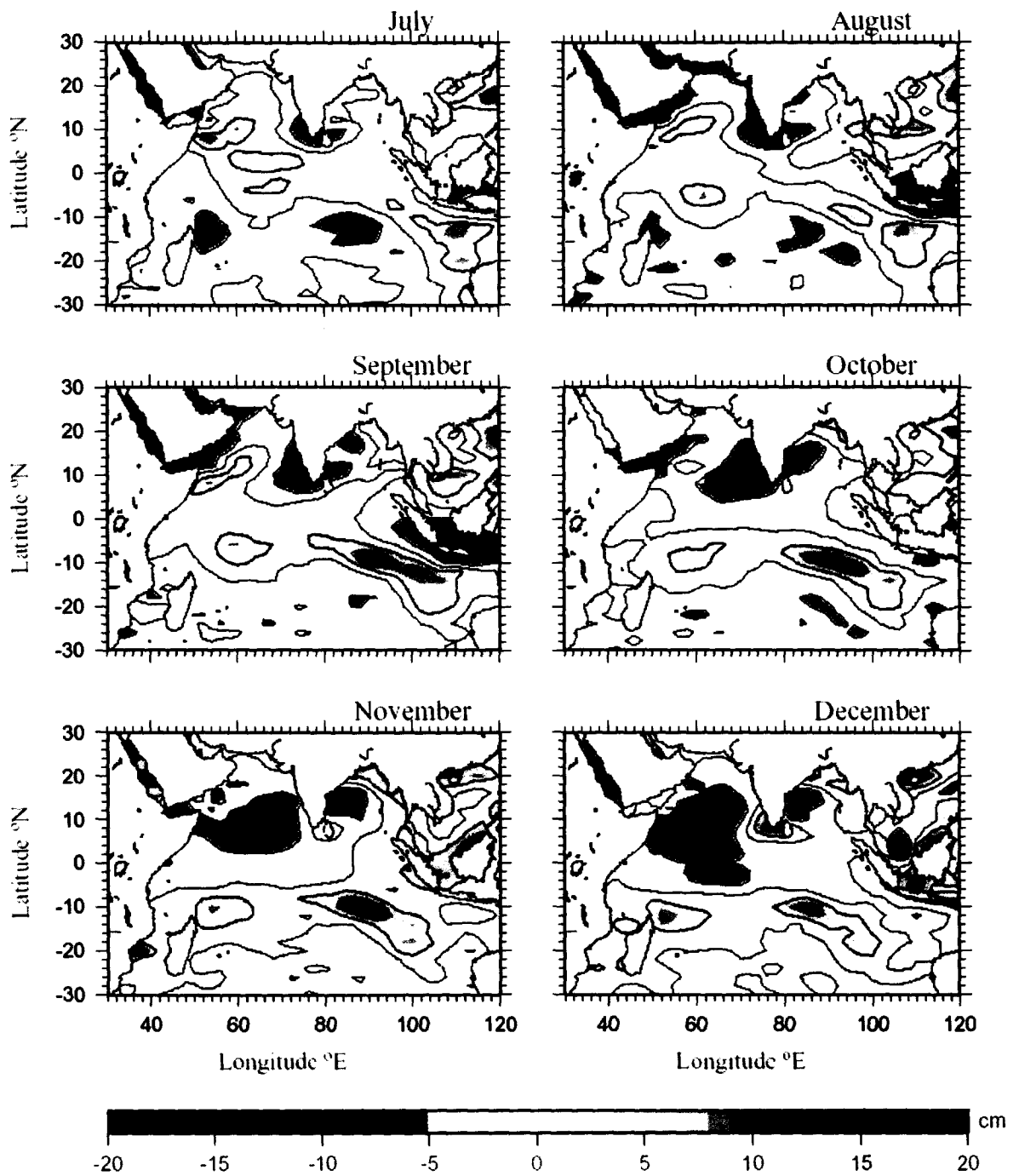


Fig. 3.3b: Continuation ...

During January to March, negative sea surface height (-7cm to -12cm) is observed along the coast of Sumatra, with a basin wide anticyclonic circulation, which may be due to the western boundary current starting at the east coast of India and flowing along the coast. This coastal current pushes the water to right side of the

flow. This gyre shifts towards west in the following months till April, with breaking up into two eddies in March, and then translates into cyclonic gyre from September onwards.

All through December and January the south Indian Ocean covered with sea surface height ranging from -5cm to 5cm, the lower sea surface height (-7cm to -12cm) is observed along the coast of Sumatra, with a basin wide anticyclonic circulation. This gyre shifts towards west in the subsequent months till April with further reduction of sea surface height to -15cm. From May to August, most of the south equatorial Indian Ocean is dominated by positive sea surface height values. The eastern equatorial Indian Ocean characterized with negative sea surface height of -12cm though the entire south equatorial Indian Ocean are covered with positive sea surface height. From September to December, positive sea surface height dominates the south Indian Ocean.

3.5 Spatiotemporal Distribution of Net Heat Gain

The heat flux across the air-sea interface is an important link between the Ocean and Atmosphere. Net heat gain is the sum of incoming and outgoing radiation that determines the net heating or cooling according to its individual magnitude. The current trend of Ocean General Circulation Models is to use heat fluxes on seasonal scale (Semtner and Chervin, 1992). European center for medium range weather forecast net heat gain for the years 1990 – 2000 are used for generating

the mean monthly charts. Its distribution over the study region is shown in figure 3.4.

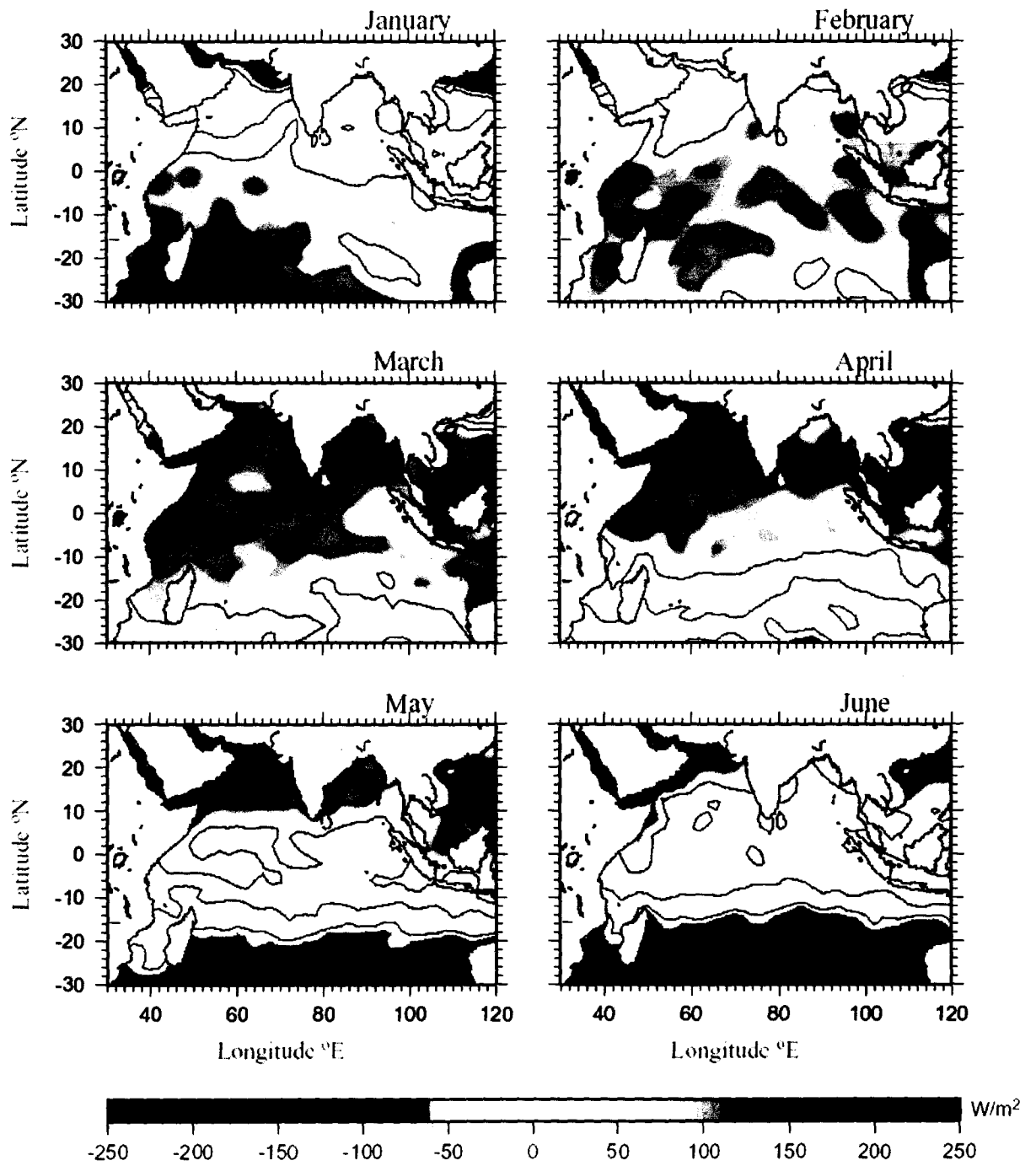


Fig. 3.4a: Monthly mean distribution of net heat gain.

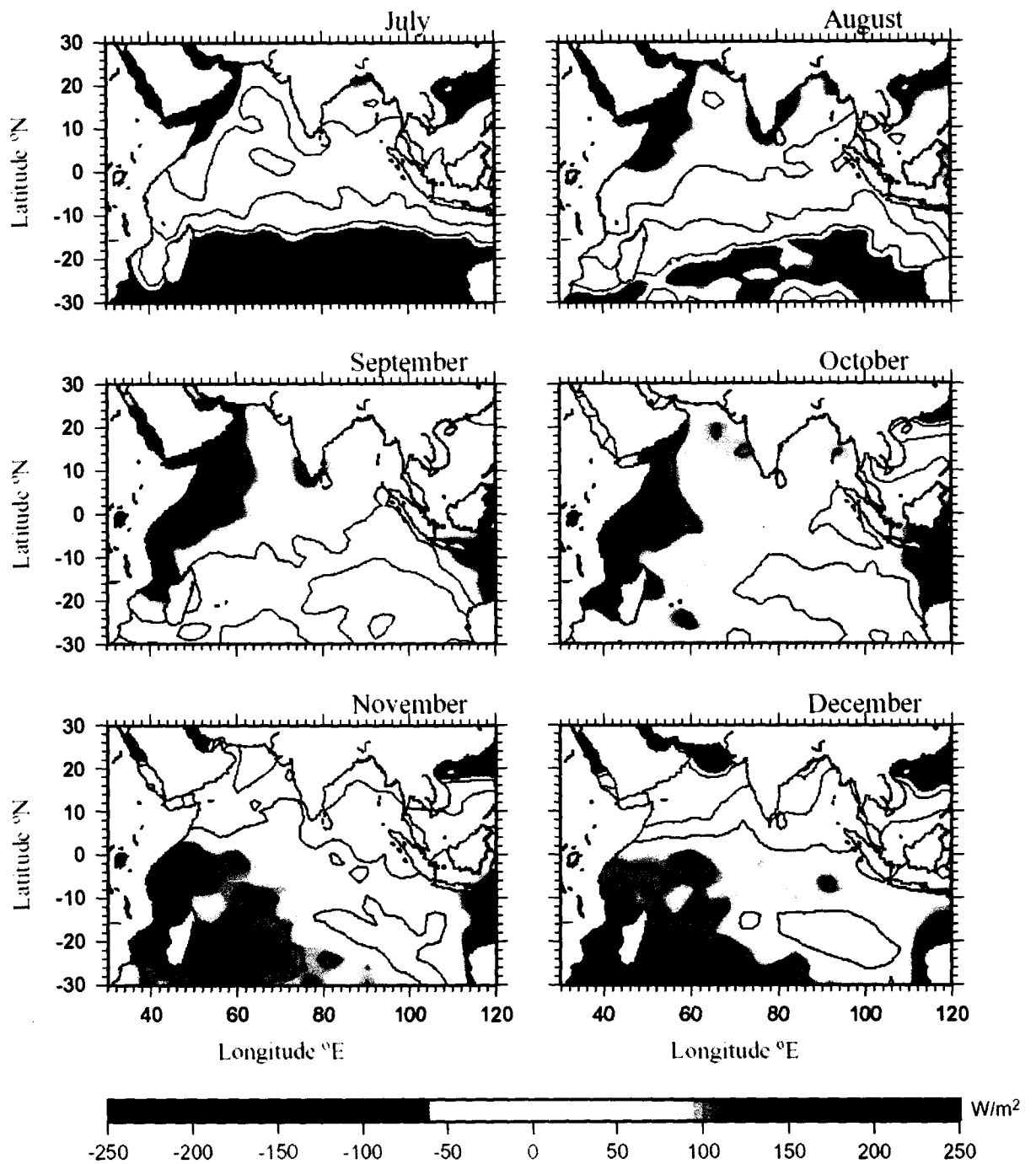


Fig. 3.4b: Continuation ...

The net heat gain over Arabian Sea has a bi-modal distribution of maximum during monsoon transition periods and minimum through monsoon seasons. Most of the incoming solar radiation in summer is utilized in raising the water temperature and thereby developing a strong summer thermocline at surface level.

The maximum net heat gain is found in May with mean value of 250Wm^{-2} . The cooling and cloud cover due to the advancement in summer monsoon reveal reduction of net heat gain from 250Wm^{-2} to 50Wm^{-2} during August. Summer cooling is supported by horizontal advection of cold waters and coastal upwelling along the Somali and the Arabian coast (Wooster et al., 1967; Colborn, 1971; 1975) with characteristic net heat gain of 55Wm^{-2} . The net surface heat loss in the western regions of the Arabian Sea reaches its maximum towards end of June, while in the eastern Arabian Sea, the maximum loss of heat occurs around July. The net heat gain increases from August onwards and mean value reaches to about 120Wm^{-2} , which is 52% lower than May values. The surface layers once again starts cooling from December due to reduction of net heat gain.

Like Arabian Sea, Bay of Bengal has a bi-modal distribution with maximum during monsoon transition periods and minimum through monsoon seasons with respect to net heat gain. The maximum net heat gain during summer season is 150Wm^{-2} and found in April. Over Bay of Bengal cooling starts much early to Arabian Sea and the mean value of net heat gain is 10Wm^{-2} in June. The net surface heat loss in the entire Bay of Bengal reaches peak towards the end of June and early July. The net heat gain increases from August onwards and mean value reaches to about 80Wm^{-2} , which is 47% lower than April values. The net heat gain reduces from December onwards.

The net heat gain over southern Indian Ocean has a uni-modal distribution with single maximum during austral summer (November-January) and minimum (May-July) through austral winter season. The maximum net heat gain is found in December with mean value of 200Wm^{-2} over western region of southern Indian Ocean and an asymmetric distribution over eastern southern Indian Ocean with 75Wm^{-2} . The minimum values during austral winter season are predominant to that of northern hemispheric oceans. The lowest values are found during June-July (-200Wm^{-2}).

3.6 Spatiotemporal Distribution Sea Surface Temperature

The surface value of Levitus, (1994) climatic data set is assigned as sea surface temperature in order to explain spatial distribution. The distribution of sea surface temperature is shown in figure 3.5. The sea surface temperature of the Arabian Sea has a bimodal distribution, which differs from the usual pattern of a single maximum at the end of summer season and minimum at the end of winter season. Most of the incoming solar radiation in summer is utilized in raising the water temperature and thereby developing a strong seasonal thermocline. With the advance of the summer monsoon, predominant cooling takes place through (Rao et al., 1976; Ramesh Babu and Sastry, 1984):

- (1) Advection of cold water from the African Coast,
- (2) Increased heat flux to the atmosphere,
- (3) The reduction in the incoming solar radiation, and
- (4) Entrainment of the cold subsurface waters into the surface layer.

along Somali and Arabian coasts, summer cooling is supported coastal upwelling due to strong offshore winds (Wooster et al., 1967; Colborn, 1971; 1975). Due to summer cooling of waters and prevention of subsequent formation of the seasonal

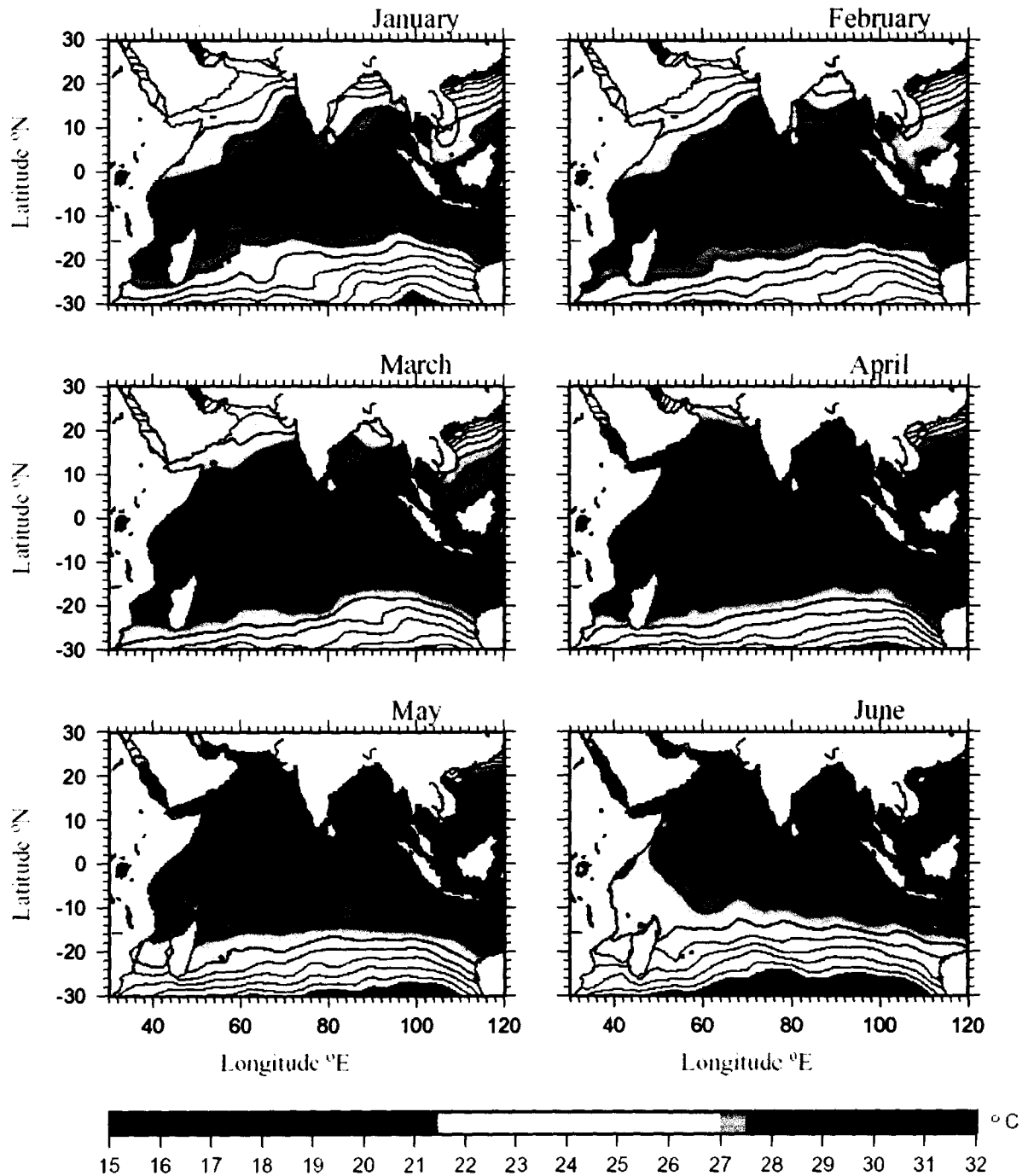


Fig. 3.5a: Monthly mean distribution of sea surface temperature.

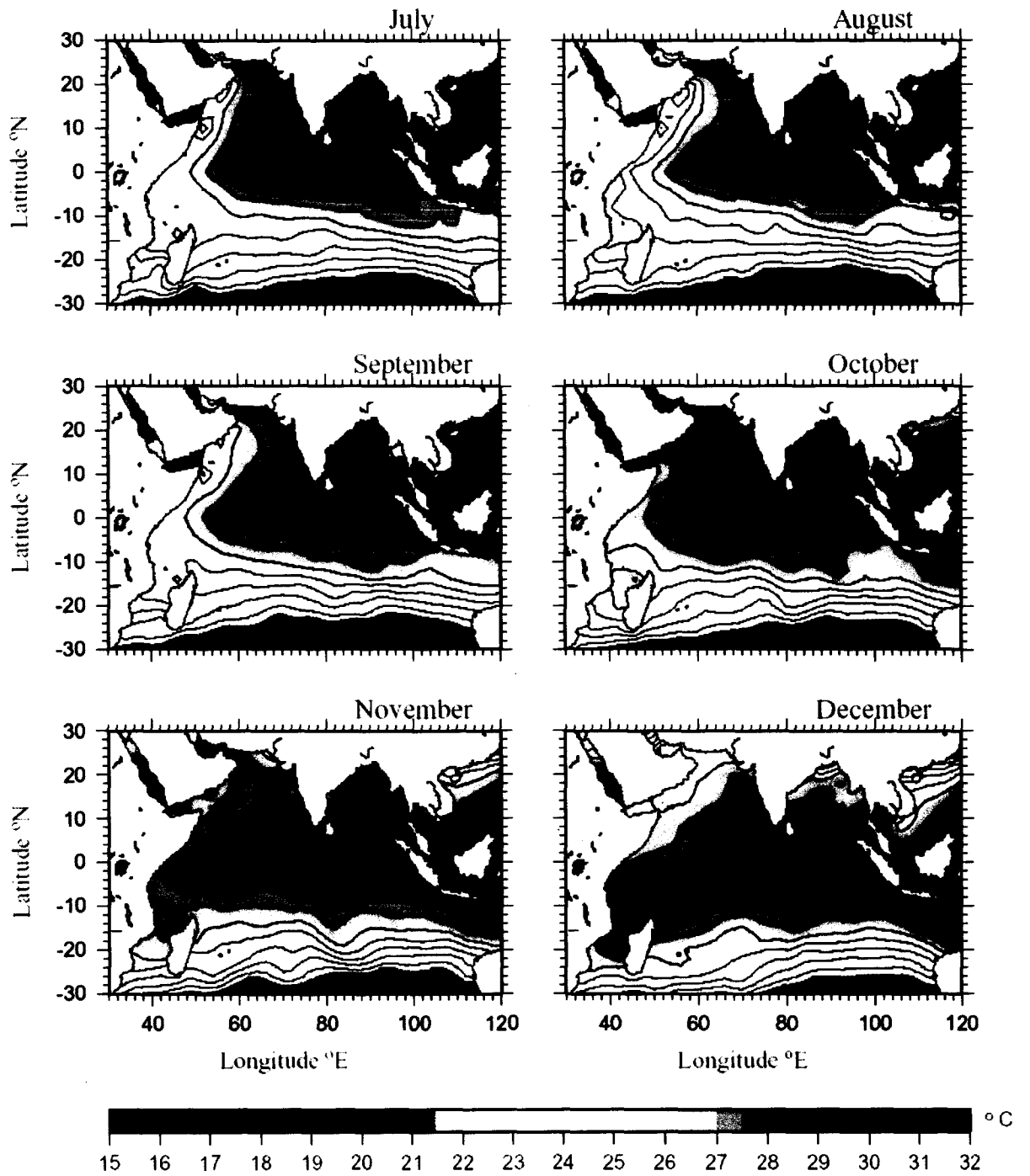


Fig. 3.5b: Continuation ...

thermocline, the Arabian Sea exhibits the characteristic of subtropical waters (Colborn, 1975). The net surface heat loss in the western regions of the Arabian Sea reaches maximum at the end of June, while in the eastern Arabian Sea, the

maximum heat loss occurs around August because of the four processes mentioned above. The secondary maximum in the water temperature occurs after the cessation of the southwest monsoon with the decrease in cloudiness and consequent increase in the incoming solar radiation and reduction in evaporation. However, temperature is as low as 14°C off Somali coast and this feature is reported to occur in July (Bruce, 1968; 1970).

Ramesh Babu and Sastry, (1984) investigated the various mechanisms responsible for the lowering of water temperature in the upper layers in the eastern Arabian Sea during the southwest monsoon of 1979. They concluded that this lowering of the temperature is primarily due to downward transfer of heat, which accounts 55% of the heat loss in the upper layers, while 45% of heat to the atmosphere.

From September onwards the water temperature increases and reaches to 29°C over most parts of the Arabian Sea by November and remains steady over the entire region. The surface layers once again starts cooling from December. This cooling first sets in the western and central regions while the eastern parts maintain relatively higher temperature. By January, the surface temperature is around 25°C north of 10°N and west of 65°E. The Central and eastern regions do not cool significantly and the temperature remains around 27°C this cooling process ceases by February and warming starts thereafter. In this region, maximum temperature is recorded in August unlike in the rest of the Arabian Sea (Wyrтки, 1971).

A Bimodal distribution of sea surface temperature observed in central Bay of Bengal is similar to Arabian Sea. During the peak of southwest monsoon the sea surface temperature drops to 28°C along the coastal boundary. This is partly due to the effect of mild upwelling in response to the monsoonal winds. The maximum temperature is observed during May and June. Second sea surface temperature maxima attains during September and October. The gain in temperature is more in the northern Bay than in the southern Bay. The sea surface temperature rises to 27°C by October and is fairly uniform over the entire Bay. During winter the sea surface temperature falls rapidly to as low as 24°C in the northern Bay. After February the surface warming begins and reaches a maximum up to 30°C by May aided by the latitudinal variation of solar radiation. The temperature distribution along the coastal areas is influenced by the river discharges (Ganapati and Murty, 1954). The distribution pattern changes considerably during southwest monsoon period. The net surface heat exchange from the Bay of Bengal is generally low (Colborn, 1975).

The sea surface temperatures in the equatorial regions are high around 29°C and fairly steady throughout the year. The temperature distribution in the area south of 10°S is zonal. During June-September, the period of southern winter, lowest surface temperature of 12°C -13°C is observed around the southern regions of the Indian Ocean (30°S). The sea surface temperature in the southern region starts warming up from September and reaches a maximum of about 15°C by

December. The annual march of the sun does not show any impact on the surface temperature in the equatorial regions. Off southeastern coast of Africa the temperature varies from 24°C to 28°C and off southwestern coast it varies from 17°C to 21°C annually.

3.7 Spatiotemporal Distribution of evaporation minus precipitation

Figure 3.6 shows the spatial distribution of evaporation minus precipitation over the Indian Ocean. The Mean monthly evaporation minus precipitation is constructed for the years 1990 – 2000 from reanalysis pentad fields of Hamburg Ocean-Atmosphere Parameters and Fluxes from Satellite Data (HOAPS) by Grassl et al., 2000. This data set covers 12.5 years from the beginning of the Special Sensor Microwave/Imager (SSM/I) data record (July 1987 to December 1998).

The most striking characteristic of the rainfall distribution over the Indian Ocean is the anomalous difference between the eastern and western regions in the north. Annual mean precipitation varies between 10cm per year in the west (on the Arabian coast) and 300cm per year or more in the east (near Sumatra and over the Andaman Sea). This is the reverse of the situation usually encountered in the subtropics, where the Trades bring dry continental air over the sea in the east and rain to the western coast. The normal situation of little rain in the east and high rainfall in the west prevails in the southern Indian Ocean; western Australia receives less than 50cm per year but Madagascar some 200cm per year.

Over the Arabian Sea, evaporation minus precipitation 0.8mm day^{-1} is detected most of the time. During the summer months it increases to 1.2mm day^{-1} near Somali coast, along the coast of Arabian Sea. The summer monsoon precipitation

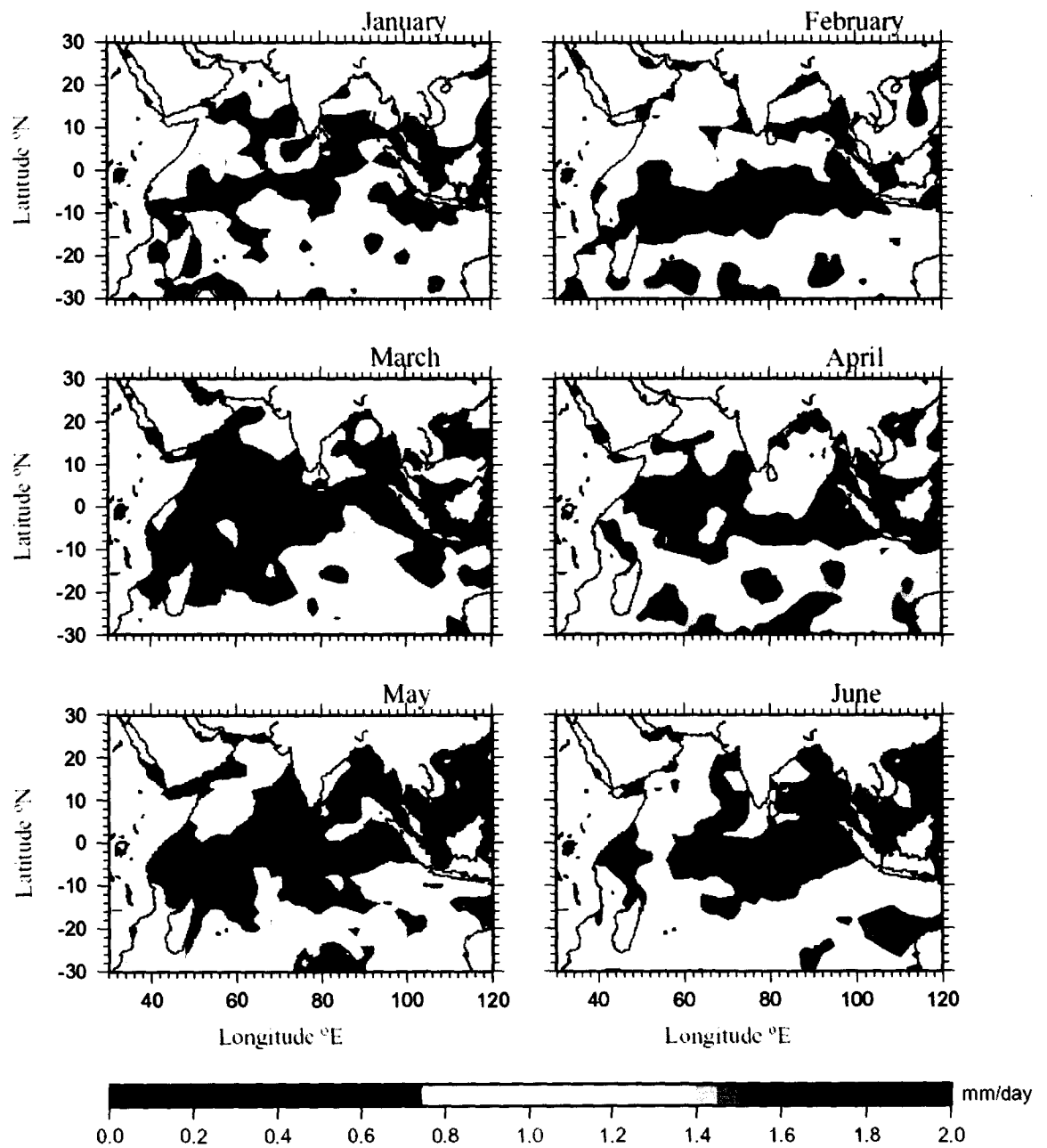


Fig. 3. 6a: Monthly mean distribution of evaporation minus precipitation.

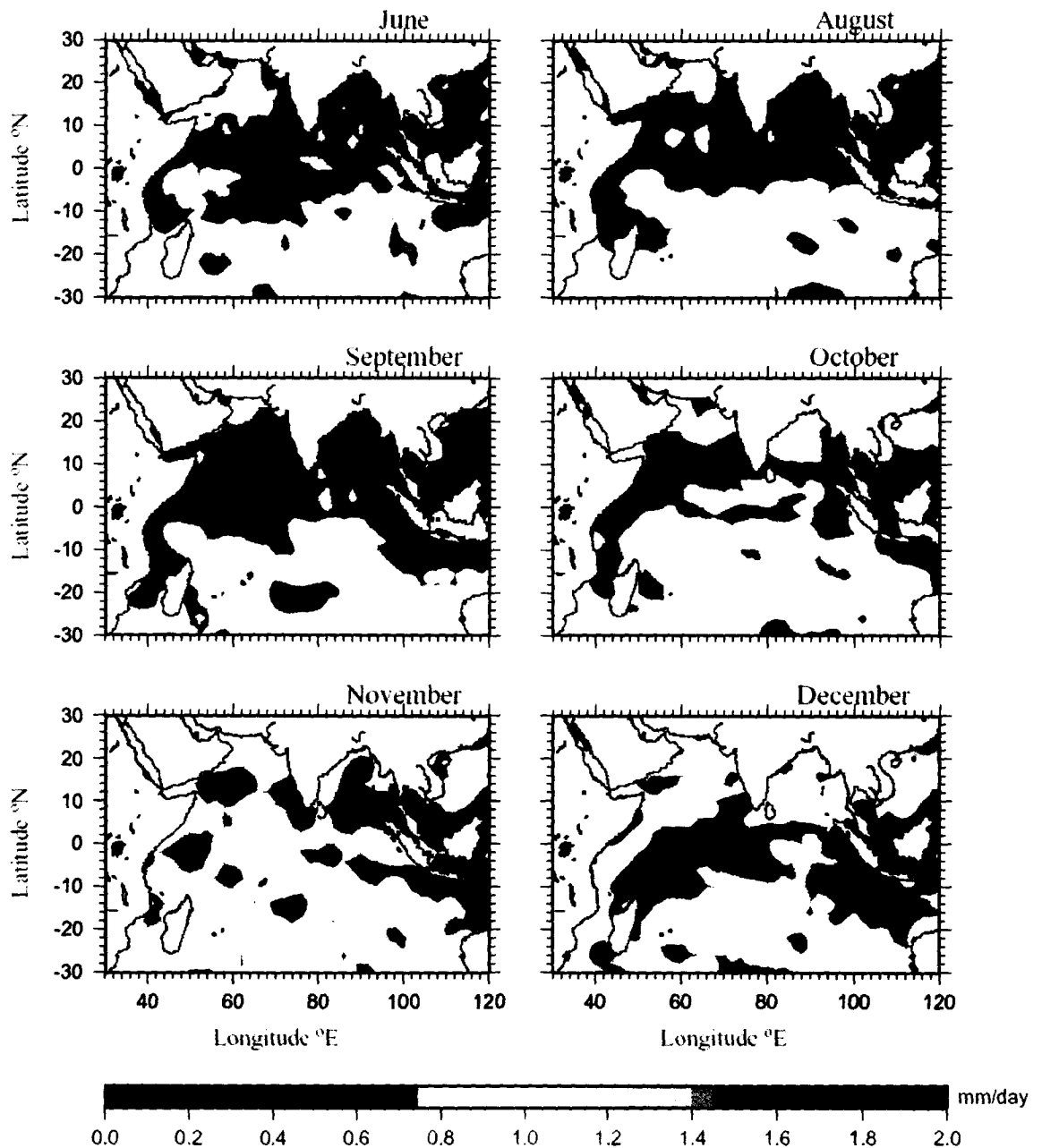


Fig. 3. 6b: Continuation ...

makes evaporation minus precipitation to decline to $0.4 - 0.6 \text{ mm day}^{-1}$. During July a higher evaporation occurs in the central Arabian Sea in compare to the other months. Later a uniform distribution is observed all over the region. Almost all the time, the western boundary of the Arabian Sea shows higher evaporation compared to the eastern boundary. Given the small variation of evaporation over

the region, the evaporation-precipitation balance reflects the rainfall distribution closely. The change from zonal to meridional direction of the evaporation minus precipitation gradient occurs near 10°S in the west and closer to the equator in the east. The continuation of the Pacific inter-tropical convergence zone (ITCZ) and associated rainfall region into the Indian Ocean along 5°S brings rain to the seas west of Sumatra throughout the year; it dominates the annual mean distribution between 10°S and the equator. North of the equator the annual mean rainfall is a poor representation of the actual situation. Evaporation minus precipitation values varies from -1.64mm day⁻¹ along the western Indian coast (in the figure the negative values are not visible) and in the eastern Bay of Bengal during the Summer Monsoon to 0.41mm day⁻¹ during the Winter Monsoon. As with the winds and the currents, the Summer Monsoon produces the stronger signal and dominates the annual mean evaporation minus precipitation distribution, which shows the eastern Bay of Bengal as a region of freshwater gain comparable in importance to the Inter-tropical Convergence Zone.

3.8 Temporal variability of parameters at selected locations

Four different locations are chosen to see the monthly variation of different parameters whose spatial variability is explained above in this chapter. The chosen locations are (a) central Arabian Sea (61.5° E; 16.5° N), central Bay of Bengal (88.5° E; 16.5° N), (c) west equatorial region (91.5° E; 1.5° N), and east equatorial region (49.5° E; 1.5° N) the results are depicted in figure 3.7.

Figure 3.7 (a) shows a bimodal distribution in mixed layer depth, and sea surface temperature. At this location, sea surface temperature and mixed layer depth are anti-correlated. The first peak in mixed layer depth occurs during winter season and the second one in July. Highest winds of 11ms^{-1} persist from June to August and in winter season. The first maximum of evaporation minus precipitation occurs in June and the next in November. Sea surface height values started increasing from May to mid-June, which declines later. Sea surface temperature and net heat gain has similar patterns, with a time delay of nearly one month (visual interpretation).

In the central Bay of Bengal, yearly twice deepening in mixed layer depth is observed (Fig. 3.7b). The extent of deepening is more in the winter season than during the southwest monsoon time, thus indicating the less influence of southwest monsoon effect on Bay of Bengal. Winter season sea surface temperature is 26°C ; the second minimum is not as prominent as in Arabian Sea. During the summer monsoon net heat gain shows a minimum value: the patterns look similar to Arabian Sea. Winds are higher during June to August, and in December. Evaporation minus precipitation effect dominates this region during the month of May.

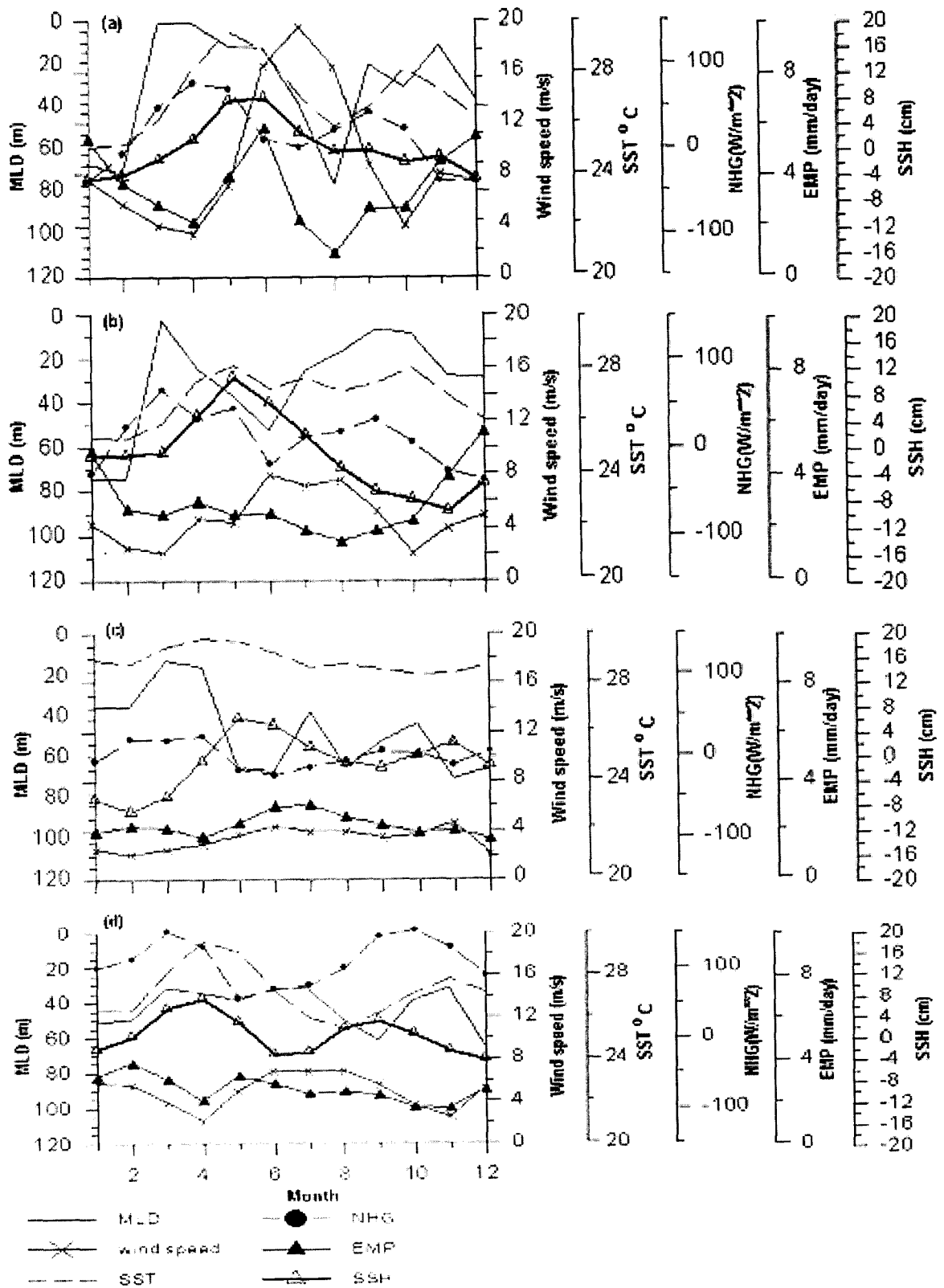


Fig. 3.7: Temporal variation of parameters

Variability in mixed layer depth is least near the east equatorial region compared to the central Arabian Sea and Bay of Bengal (Fig. 3.7c). Twice deepening in mixed layer depth is observed at this location, one in December and other in June. A maximum of 65m deepening of mixed layer is observed in the months of May and June. Elevated sea surface height is found during summer months. Variation in evaporation minus precipitation at the equatorial region is minimal; this may be because of consistence of precipitation and cloud cover. Due to the convergence of winds at the equatorial belt the variations in the wind are less in comparison to other regions.

Unlike east equatorial Indian Ocean, prominent mixed layer depth variability is found at western equatorial Ocean (Fig. 3.7d) that resembles with that of central Arabian Sea. The magnitude of convective deepening of mixed layer depth is less (40m). This oceanic region is characterized with bi-modal distribution of sea surface height. Variation in evaporation minus precipitation at the equatorial region is minimal owing to the consistence of precipitation and cloud cover and variation of wind speed is less.

Chapter IV
One-dimensional model and
parameterization

This chapter leads an insight to 1-Dimensional model of Price Weller and Pinkel popularly known as PWP model (Price et al., 1986) and its parameterization. Also, the model description, sensitivity, and model performance with different water types are explained in this chapter.

4.1 Mixed Layer Model

4.1.1 The Model equation

The model equations are diurnal in nature and are modeled as a vertical wind mixing and radiation process driven by the local surface fluxes of heat and momentum (Niiler and Kraus, 1977). The conservation equations of heat, salt, and momentum are their one-dimensional form and are as follows;

$$\frac{\partial T}{\partial t} = \frac{-1}{\rho_0 C} \frac{\partial F}{\partial Z} \quad (4.1)$$

$$\frac{\partial S}{\partial t} = - \frac{\partial E}{\partial Z} \quad (4.2)$$

$$\frac{\partial V}{\partial t} = - f \times V - \frac{1}{\rho_0} \frac{\partial G}{\partial Z} \quad (4.3)$$

where, the profiles of solar flux (F), evaporation minus precipitation (E), and wind stress (G) are to be determined. The surface values are presumed to be known; like $F(0) = Q$, the air-sea heat flux, positively downward; $E(0) = S(E-P)$, the freshwater flux times the surface salinity; and $G(0) = \tau$, the wind stress.

The heat loss is presumed to leave directly from the sea surface, while solar insolation is absorbed within the water column with double exponential depth dependence (Kraus, 1972) as given below. The 1-Dimensional equations

implicitly assume a horizontal homogeneity, since they predict the horizontal velocity at the single point but ignoring the implications of the velocity in carrying horizontal gradients of properties. Thus the missing terms from a full (hydrostatic and Boussinesq) oceanic evolution equations are turbulent flux, momentum forces due to horizontal pressure gradients, and horizontal momentum advection, heat, salt, and the vertical advection of the same.

The penetrative solar flux, which is modeled as a two-component exponential decay is as,

$$I(z) = I(0) \left(I_1 \exp\left(\frac{-z}{\lambda_1}\right) + I_2 \exp\left(\frac{-z}{\lambda_2}\right) \right) \quad (4.4)$$

the subscripts 1 and 2 refer to the red and blue-green components of the penetrating solar insolation, and z is positive downward with $z = 0$ being the sea surface. In the above equation, I_1 , I_2 , λ_1 , and λ_2 are biologically dependent attenuation parameters. The following parameters are typical of water type-1A (open ocean, hereafter type-1) of Jerlov, (1968) water classification:

$$I_1 = 0.62; \quad \lambda_1 = 0.6\text{m}$$

$$I_2 = 1-0.62; \quad \lambda_2 = 20\text{m}$$

thus about half of the solar insolation incident on the ocean surface is absorbed within the uppermost meter of the water column. The remaining short-wave radiation, principally the blue-green light, is absorbed with the attenuation length scale of 20m. Paulson and Simpson, (1977) provided the attenuation parameters of equation 4.4 for a wide range of ocean waters.

At each time step the density profile is calculated from a linear state equation by taking the temperature and salinity profile into account,

$$\rho = \rho_0 + \alpha (T - T_0) + \beta (S - S_0) \quad (4.5)$$

where, in this case $\rho_0 = 1025 \text{ Kg m}^{-3}$, T_0 the sea surface temperature, $\alpha = -0.23 \text{ Kg m}^{-3} \text{ }^\circ\text{C}^{-1}$, S_0 the sea surface salinity value, $\beta = 0.76 \text{ Kg m}^{-3} \text{ ppt}^{-1}$.

4.1.2 Mixing

The only artful part of such a model is its parameterization to wind mixing. This model is essentially the dynamic instability mixed layer model of Price et al., (1978), which was modified including a mixing process in the stratified fluid below the mixed layer (Price et al., 1986). Vertical mixing occurs in this model in order to satisfy stability criteria, which require that

$$\frac{\partial \rho}{\partial z} \geq 0 \quad (4.6)$$

for static stability,

$$R_b = \frac{g \Delta \rho h}{\rho_0 (\Delta V)^2} \geq 0.65 \quad (4.7)$$

for mixed layer stability, and

$$R_g = \frac{g \partial \rho / \partial z}{\rho_0 (\partial V / \partial z)^2} \geq 0.25 \quad (4.8)$$

for shear flow stability.

In the mixed-layer criterion (Equ. 4.7), h is the mixed layer depth, and $\Delta(\)$ takes the difference between the mixed layer and the level just beneath. The first one (Equ. 4.7), a condition for static stability that models convection, and the second,

a condition for mixed layer stability, is mean to emulate the entrainment process. These two conditions create a slab-like mixed layer with a sharp discontinuity at its base. The last condition is for shear-flow stability, and the resulting jump at the mixed layer is gradually partially mixed until this condition is satisfied. This creates a transition layer beneath the mixed layer connecting it to the ocean interior.

4.2 Sensitivity Analysis

4.2.1 Model sensitivity with surface forcing

Sensitivity of model to different atmospheric forcing is carried out for the water type-1, since yearlong model run has performed with in-situ forcing parameters obtained from US data buoy (explained later part of this chapter) deployed by Woods Hole Oceanographic Institution in deep, type-1 water, the geo-location is shown in fig. 4.1.

Wide ranges of forcing parameter are considered for sensitivity analysis. For example wind speed varied from 3ms^{-1} to 12ms^{-1} in steps of 1ms^{-1} , Total heat loss (Tloss) from -120Wm^{-2} to -30Wm^{-2} in steps of 10Wm^{-2} , and the noon radiation (Prad) from 400Wm^{-2} to 1000Wm^{-2} with an increment of 50Wm^{-2} . Assuming that,

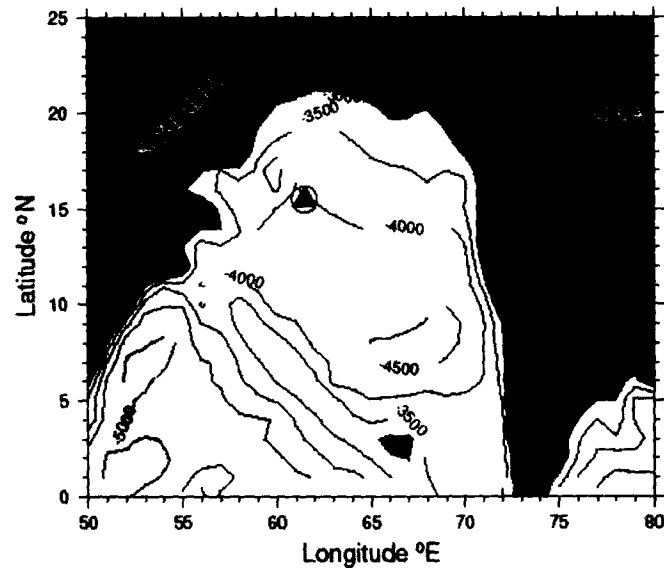


Fig. 4.1: Geo-location of the surface mooring is indicated by shaded triangle. Deployed off the coast of Oman along the climatological axis of the Findlater Jet from October 1994 to October 1995.

this parameter range covers the dynamic range over the study region. Figure 4.2 shows the sensitivity analysis results (Fig. 4.2a for wind speed, Fig. 4.2b for Tloss, and Fig. 4.2c for noon radiation). The values assigned for the biologically dependent attenuation parameters (dimensionless constants, long-wave, and short-wave extinction coefficients) are 0.62, 0.6 m, and 20 m. The changes in mixed layer depth found high (10m – 40m) for wind speed ($3\text{ms}^{-1} - 12\text{ms}^{-1}$), also for this parameter the mixed layer depth showed a positive and linear response (Fig. 4.2a). In case of noon radiation mixed layer depth ranges from 45m to 50m and its response is slightly negative for this parameter. A less variation (39m – 43m) of mixed layer depth with a positive response is observed in case of total heat loss. Table 4.1 shows the percentage reduction of mixed layer depth with these parameters. The percentage reduction is calculated as follows;

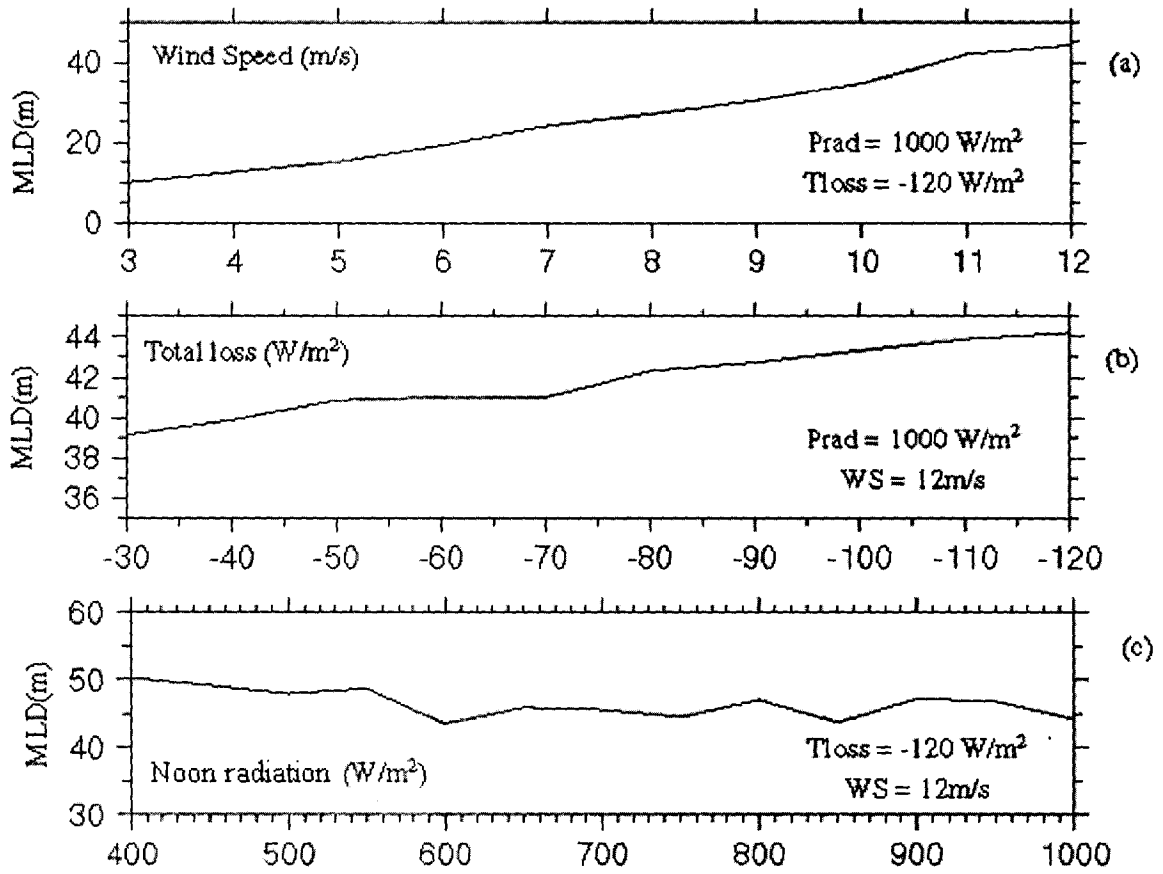


Fig. 4.2: Model sensitivity curves: variation of MLD with varying Wind speed (a), total heat loss (b), and noon radiation (c).

$$\text{Percentage reduction} = \left(\frac{\text{ref_val} - \text{Value}}{\text{ref_val}} \right) * 100 \quad (4.9)$$

The *ref_val* is the model mixed layer depth derived for the noon radiation, total heat loss, and wind speed forcing of values 1000Wm⁻², -120Wm⁻², and 12ms⁻¹ respectively. The model results with different forcing conditions are tabulated in table 4.1a, b, c namely for varying total heat loss, noon radiation and wind speed by assigning fixed values to the remaining parameters. The fractional reduction of mixed layer depth found to be more for wind speed (77.35%); negative correlated for noon radiation (-13.59%) and total heat loss (11.38%).

Table 4.1a: Percentage reduction of model MLD: with constant noon radiation and wind speed and for varying total heat loss.

Wind Speed (ms ⁻¹)	Noon radiation (Wm ⁻²)	Total heat loss (W/m ⁻²)	Model MLD (m)	Percentage reduction (%)
12	1000	-120	44.2	<i>Ref_val</i>
12	1000	-110	43.9	0.68
12	1000	-100	43.3	2.03
12	1000	-90	42.7	3.39
12	1000	-80	42.3	4.30
12	1000	-70	41.0	7.24
12	1000	-60	41.0	7.24
12	1000	-50	40.83	7.62
12	1000	-40	39.87	9.80
12	1000	-30	39.17	11.38

Table 4.1b: Percentage reduction of model MLD: with constant total heat loss, wind speed and for varying noon radiation.

Wind Speed (ms ⁻¹)	Noon radiation (Wm ⁻²)	Total heat loss (Wm ⁻²)	Modeled MLD (m)	Percentage reduction (%)
12	1000	-120	44.2	<i>Ref_val</i>
12	950	-120	46.88	-6.060
12	900	-120	47.29	-6.990
12	850	-120	43.75	1.010
12	800	-120	47.08	-6.510
12	750	-120	44.58	-1.000
12	700	-120	45.63	-3.240
12	650	-120	46.04	-4.160
12	600	-120	43.54	1.500
12	550	-120	48.75	-10.30
12	500	-120	47.92	-8.420
12	450	-120	49.16	-11.22
12	400	-120	50.21	-13.59

Table 4.1c: Percentage reduction of model MLD: with constant total heat loss, noon radiation and for varying wind speed.

Wind Speed (ms^{-1})	Noon radiation (Wm^{-2})	Total heat loss (Wm^{-2})	Modeled MLD (m)	Percentage reduction (%)
12	1000	-120	44.2	<i>Ref_val</i>
11	1000	-120	42.08	4.80
10	1000	-120	34.58	21.76
09	1000	-120	30.42	31.18
08	1000	-120	27.08	38.73
07	1000	-120	23.96	45.79
06	1000	-120	19.37	56.18
05	1000	-120	15.21	65.60
04	1000	-120	12.50	71.72
03	1000	-120	10.01	77.35

4.2.2 Sensitivity to ability of solar penetration

Just like the atmosphere, seawater simultaneously absorbs and scatters solar radiation. Absorption mainly consists of conservation of radiant energy into heat, the remaining part of the absorbed energy being involved in chemical reactions; however this part is of the order of 0.1% (Alexandre, 1977). It has been recognized that absorption of solar radiation and the resulting local heating within the upper ocean are strongly influenced by chlorophyll concentration (e.g. Ivanoff, 1977; Simpson and Dickey, 1981a,b; Simonot et al., 1988; Lewis et al., 1990; Large et al., 1994; Morel and Antoine, 1994). Sathyendrahath et al., (1991) demonstrated a significant biological impact on the Arabian Sea's sea surface temperature. Figure 4.3 shows the theoretical path-length of solar radiation for Jerlov waters and computed by using equation 4.4.

In case of type-1 water the solar radiation penetrates to a greater extent, even 1% of irradiance value has found at 200m depth or so (the depth scale is truncated to 55m). For the other water types the irradiance attenuates to a shallower depth and thus affecting the nature of thermocline. Hence keeping the penetrative profile of solar radiation to constant path-length (traced in type-1) will create more error in the temperature, density and the model computed mixed layer depth.

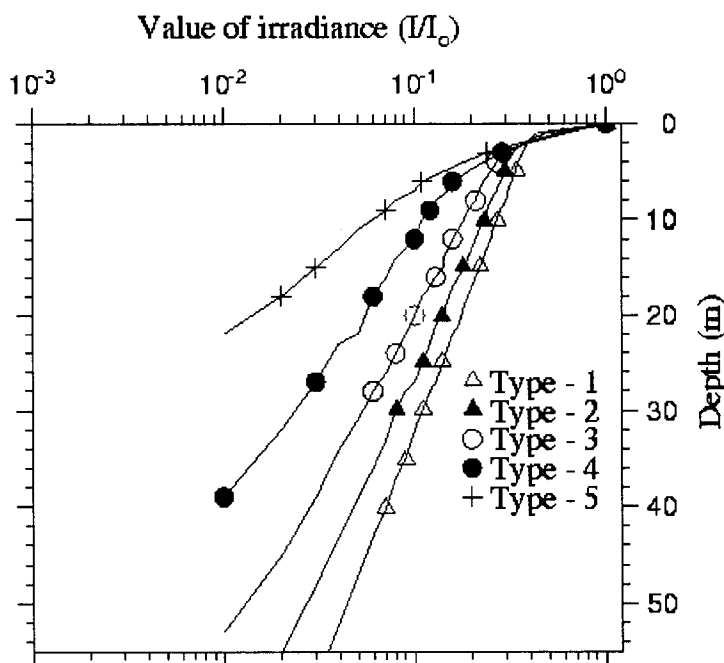


Fig. 4.3: Path length of solar radiation in different water type. Numbers represents in corresponding to those given in table 4.2.

The effect of change in water type on heating of model mixed layer with varying water types, whose values of dimensional constant, coefficient of shortwave extinction and longwave extinction are given in table 4.2. The surface meteorological conditions are kept constant, the noon radiation to 1000Wm^{-2} , the total heat loss to -120Wm^{-2} , and wind speed to 12ms^{-1} . This sensitivity analysis for reduced surface forcing conditions is not carried, since the realistic situation

may corresponds to winter condition in case of radiation fields for Indian Ocean. In this season, the convective mixing dominates the mixed layer deepening and also the depth of convection is greater than the depth of biological heating. To an outcome, the highest mixed layer depth (46.88m) is found for water type-1, and lowest is noticed for water type-1 (B). The table 4.2 depicts the result.

Table 4.2: Model computed result under unified forcing condition in different water types.

Water type	Dimensional constant R	Longwave extinction coefficient ζ_1 (m)	Shortwave extinction coefficient ζ_2 (m)	MLD (m)
I (1)	0.58	0.35	23	46.88
IA (2)	0.62	0.60	20	42.71
IB (3)	0.67	1.00	17	41.67
II (4)	0.77	1.50	14	43.54
III (5)	0.78	1.40	7.9	42.50

4.3 Yearlong model computation and comparison with in-situ observations

Yearlong hourly data sets of both the atmospheric as well as the oceanographic data collected from US data buoy by Woods Hole Oceanographic Institution during October 1994 – October 1995 is used to investigate the model performance. The accuracy of the parameter was reported by Weller et al., (1998).

4.3.1. Overview of Atmospheric data

The buoy atmospheric observations over central Arabian Sea are shown in figure 4.4. The mooring was deployed long before the start of the winter northeast monsoon. The dominance of two monsoon seasons over the site can be demarcated well from the observations, each with dramatically different forcing.

After an initial storm in late October (which is noted by spikes in the wind speed and in solar radiation) the first few months of the deployment are dominated

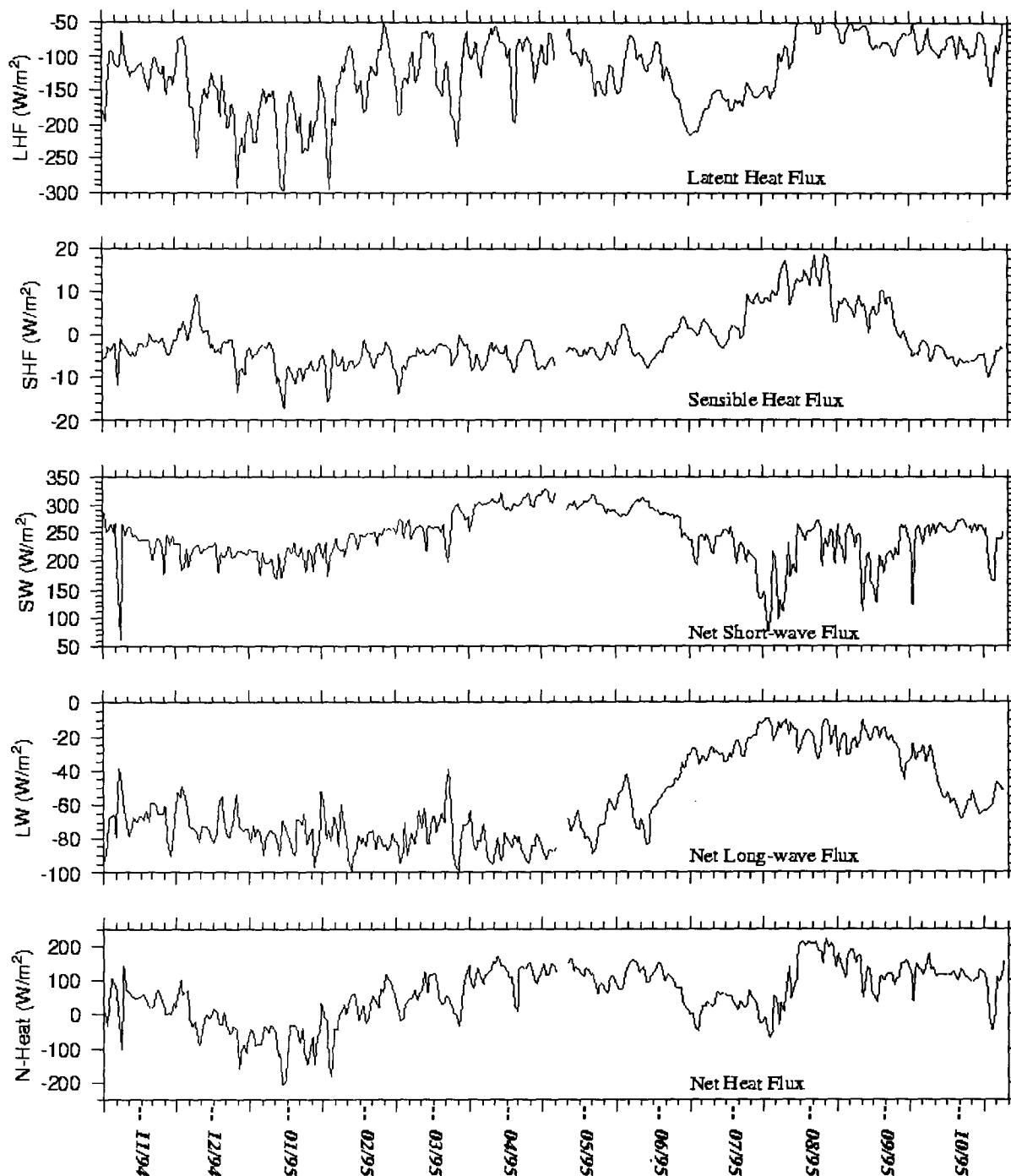


Fig. 4.4: Measured radiative flux observations over the buoy time span.

monsoon. Wind speed is moderately strong (from $5ms^{-1}$ to $10ms^{-1}$) during this period. But they were not completely steady, showing variations, with periods of

higher winds lasting about five days appearing approximately every 15 - 20 days. Though the recorded sea surface temperature dominated over air temperature, the air temperature and sea surface temperature both dropped during northeast monsoon. The solar radiation slightly reduced due primarily to the winter season and finally the reduced levels of downwelling longwave radiation are in keeping with the low cloud cover and relatively low moisture in the atmosphere. From February through May 1995, the air temperature and sea surface temperature both scaled-up, with evidence of strong diurnal heating. The southwest monsoon dominated the record from May through the end of September 1995, although the starting date of the southwest monsoon is difficult to restrain, certainly at the beginning of May, the stronger (up to 10ms^{-1}) and steady southwesterly direction of the winds prevailed. By the second week of June, however, the southwest monsoon has reestablished itself, and does not relinquish its hold until end of September. Wind speeds were strong, ranging from 10ms^{-1} to 15ms^{-1} , with gusts up to 18ms^{-1} . The air temperature and sea surface temperature again drops. The sea surface temperature is much colder than the air temperature over this period. The incoming solar radiation record is sharply reduced, in part due to the natural yearly cycle, which has two peaks in the tropics, but primarily showing influence of clouds. The record ends going into another inter-monsoon period with relaxed wind, and repeating the cyclic nature of air and sea surface temperature record. The daily averages of air-sea heat flux and momentum are shown in figure 4.5.

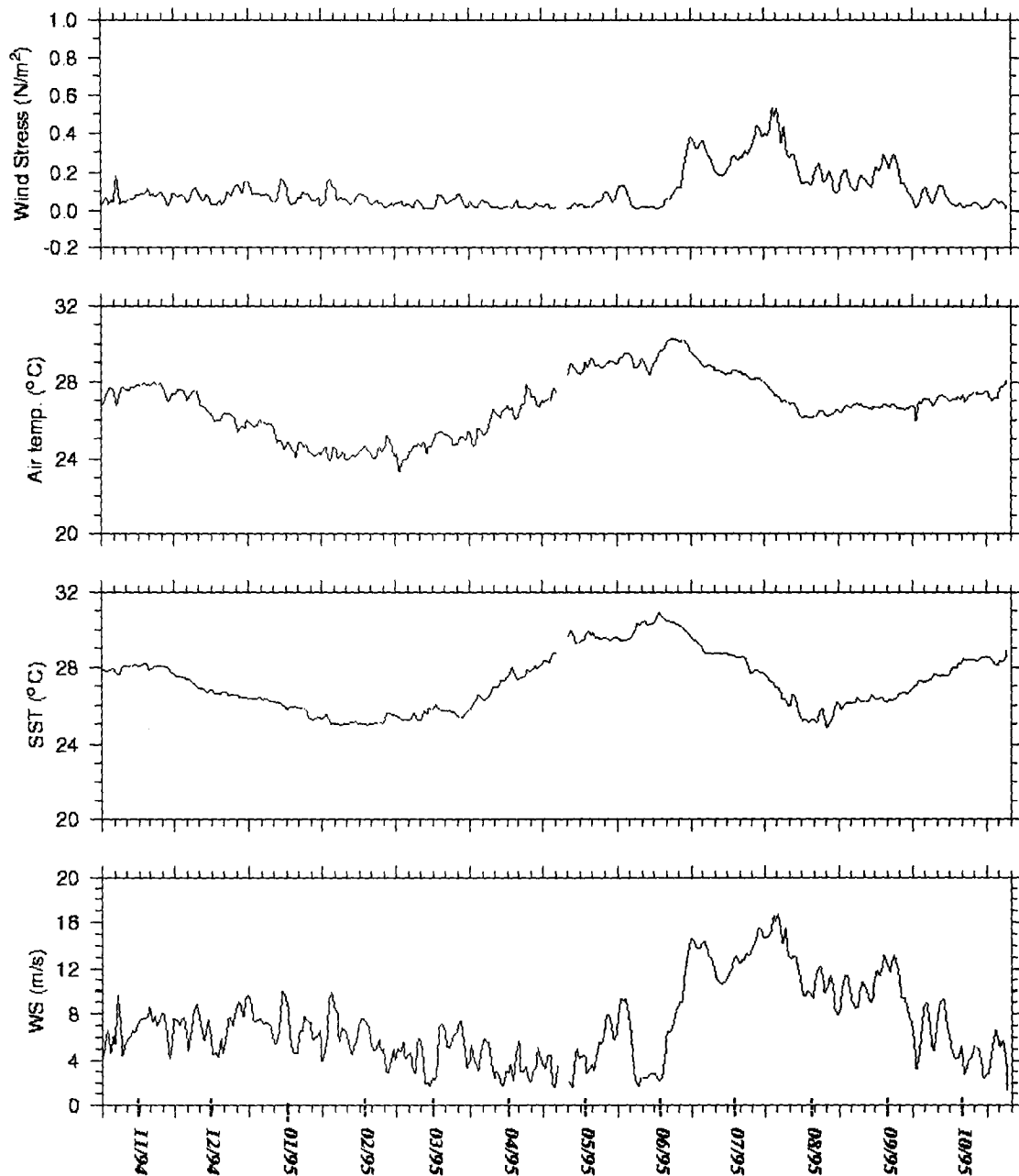


Fig 4.5: Meteorological observation over the buoy time span.

During the northeast monsoon, a combination of factors led to a net heat loss from the Ocean. Possibly due to the strongest latent heat losses driven by the moderate flow of dry air over the sea surface, the net shortwave heat flux is weak and the strong net longwave heat flux. The heat loss may be modulated with the characteristic modulation of wind speed. This can also clearly be seen in the wind

stress record, as broad peak of wind stress approaching 0.2Nm^{-2} are following by periods of reduced wind stress. As mentioned before, a net heat loss at this site has been reported during the southwest monsoon (Hastenrath and Lamb, 1979), although this is disputed by other climatologies. The record shows that at the mooring site, the net heat flux stays positive for the majority of the southwest monsoon season.

4.3.2. Over view of oceanic response and Mixed Layer Depth

Resembling the atmospheric record, the density and temperature records over depth are dominated by the two monsoon seasons. The dominant signal in the mixed layer is the twice-annual cycle of deepening and shoaling. This striking feature of the upper ocean deepening and cooling of the mixed layer over the central Arabian Sea during southwest and northeast monsoon seasons is unique among the world oceans (Rao et al., 1989). Owing to the combined action of cold continental air blow over the sea surface and positive wind stress curl (during January 1994 and beginning of April 1995), which favors convective, overturning of surface waters with water beneath the surface, the characteristic water temperature up to 120m depth get adjusted between 24°C to 26°C and corresponding density is ranging from 23 to 25 in σ_t scale (Fig. 4.6). Subsequently quashes the seasonal thermocline in each winter season with permanent thermocline. Intense solar heating and moderate surface wind forcing

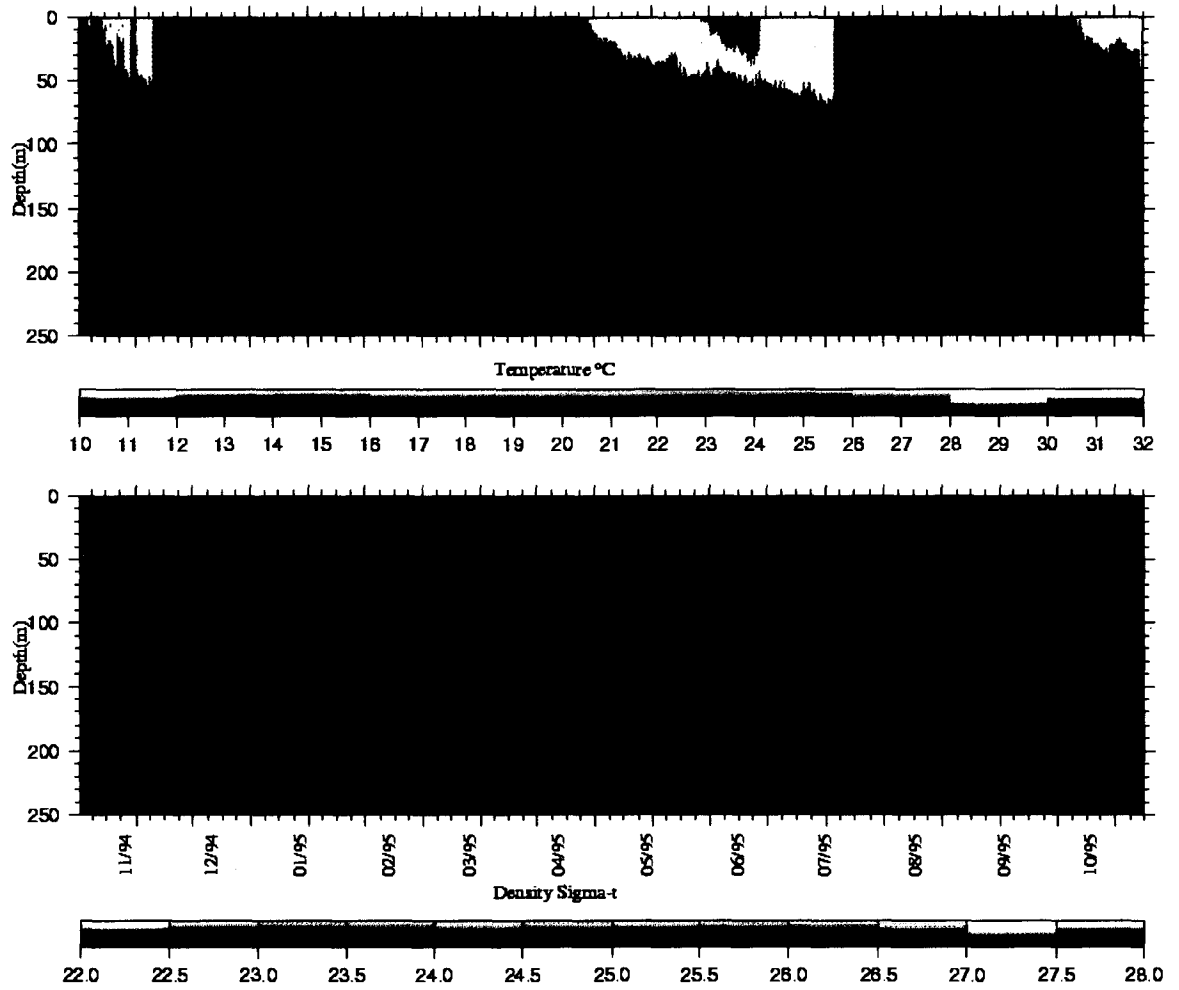


Fig. 4.6: Upper ocean thermal and density response to surface forcing.

during summer season favors for the formation of seasonal thermocline during austral spring season. During the observational period the seasonal thermocline with unified water temperature of $30^{\circ}\text{C} - 32^{\circ}\text{C}$ is observed at the bulk level of 30m – 40m depth. The seasonal thermocline region characterized with density of $23.5\sigma_t$. The magnified winds over Arabian Sea strengthen the mixing and mixed layer depth further deepens. The mixed layer depth computed from the density profile is near about 80m (Fig. 4.7). An alternate explanation for the deepening of mixed layer depth during this period had given by Bauer et al., (1991), who

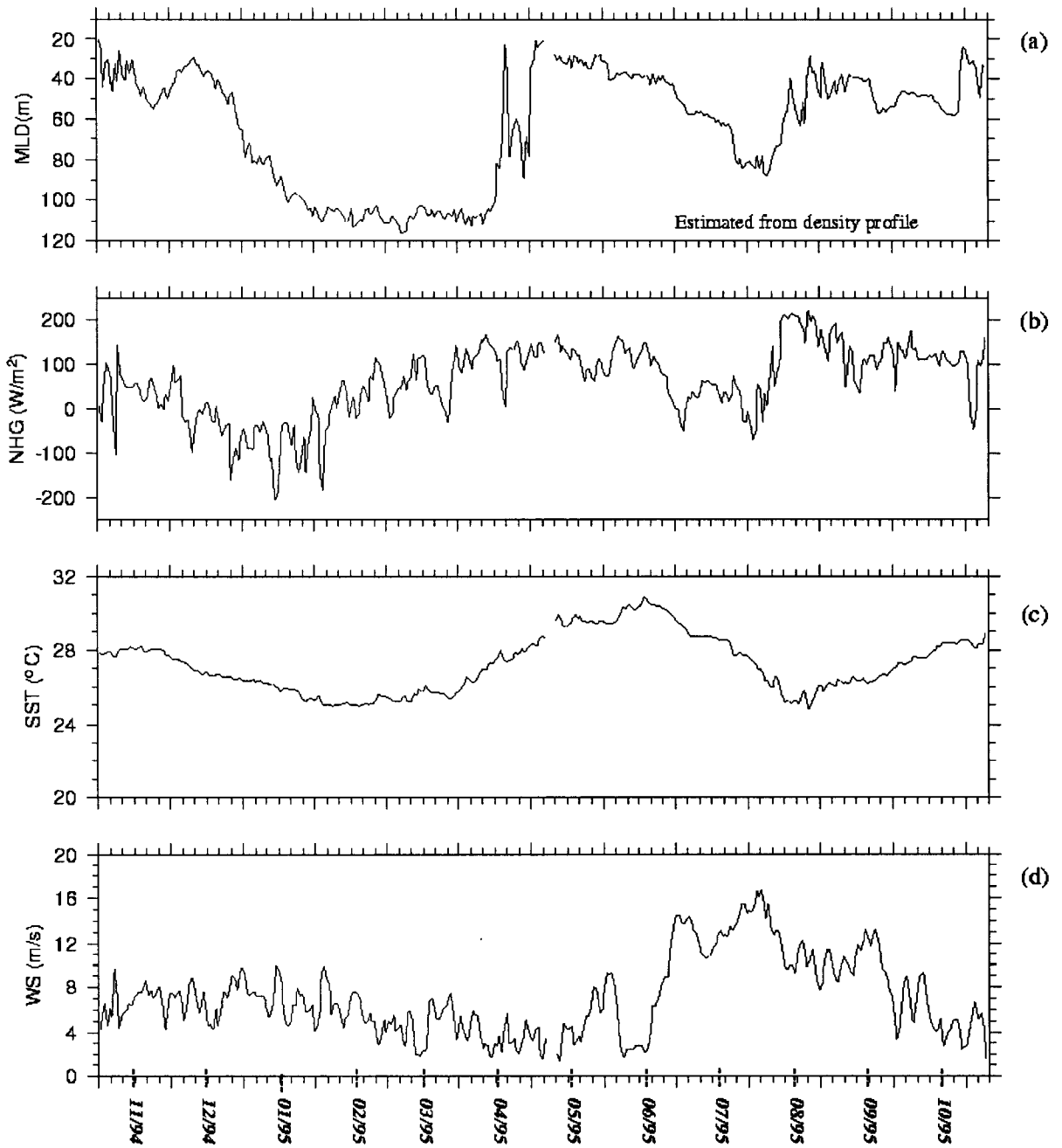


Fig. 4.7: Estimated MLD and the parameter concerned for its variation.

proposed that shoreward of Findlater jet pulls the thermocline closer to surface leading to open-ocean upwelling, and shallower mixed layers, while on the offshore side wind stress curl-driven downwelling leading to deepen the mixed layers.

4.3.3 Model performance for these observations

The model forcing parameters are averaged on daily basis, which is identical to the model run with satellite winds/reanalysis fields for the years 1990 - 1996. In the model, all the input parameters are linearly interpolated to model time step (15 minutes) and the radiation input in accordance to equation 4.10. The initial temperature and salinity profile are taken from Levitus climatology and the model is initialized at the beginning of each month. The biological dependent coefficients are considered to type-1 ocean waters. The model output and *in-situ* mixed layer depth are averaged on daily basis. Figure 4.8 shows both the model derived and observed mixed layer depth over the site. Both the observation and model results captured the twice-yearly deepening of mixed layer to the surface forcing. Model trend matches well with *in-situ* values during the initial period of

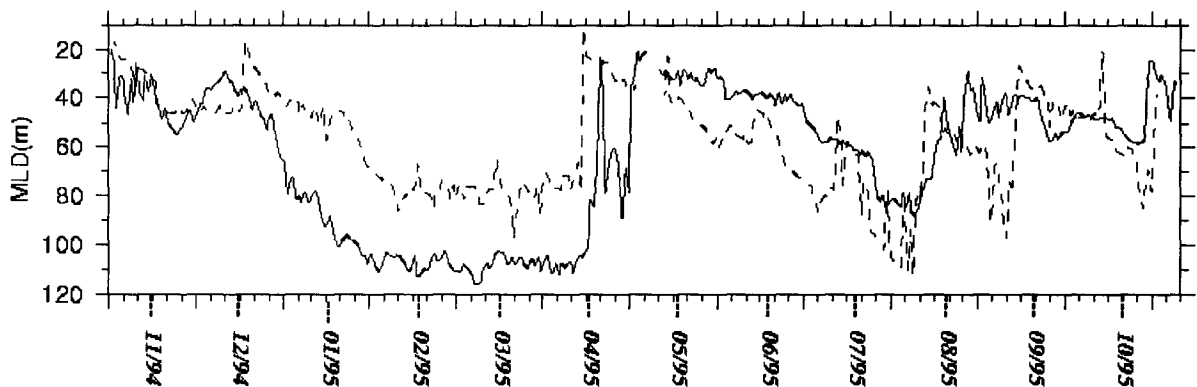


Fig.4.8: Comparison of model with buoy observations MLD. Solid line corresponds to the buoy observation, and the dashed line corresponds to model output.

deployment up to December-1994 and subsequently model mixed layer depth deepens, but deepening is less compared with observations till third week of March. The second deepening of model mixed layer depth follows in agreement

to *in-situ* mixed layer depth with bias of ~10m. During second and third weeks of August the bias is increased nearly to 40m - 60m.

4.4. Remote sensing parameters in Mixed Layer computation

Few assumptions were made to quantify remote sensing/re-analysis parameters into the model computation. They are;

- (1) The solar heating on the sea surface follows a cosine pattern
- (2) Wind speed is constant over a day
- (3) Total heat loss from the surface is uniform throughout a day
- (4) Classification of water type based on chlorophyll concentration. Thus the above classified oceanic region is assumed for the treatment of seawater turbidity, suspended sediments, and biodegraded yellow substances

4.4.1. Diurnal variation of model forcing parameters

One-day profile of diurnal variation of the surface radiative forcing and wind speed is given in the figure 4.9 for the day (20th October 1994). Of these the surface ranges from -400Wm^{-2} to -350Wm^{-2} , maximum heat loss observed at the middle of the day. Neglecting this part it may be concluded that total loss is uniform in a diurnal cycle. Wind speed shows a minimum value towards the beginning of the solar cycle, 2.5ms^{-1} , and maximum in night, 5ms^{-1} . For further model investigation only daily winds were considered, even though it has a significant variation in diurnal cycle. Since most of these parameters are available from remote sensing platforms/re-analyzed fields it is possible to assume the

diurnal variation over remote sensing observations with little error and added advantage of all weather and spatial availability.

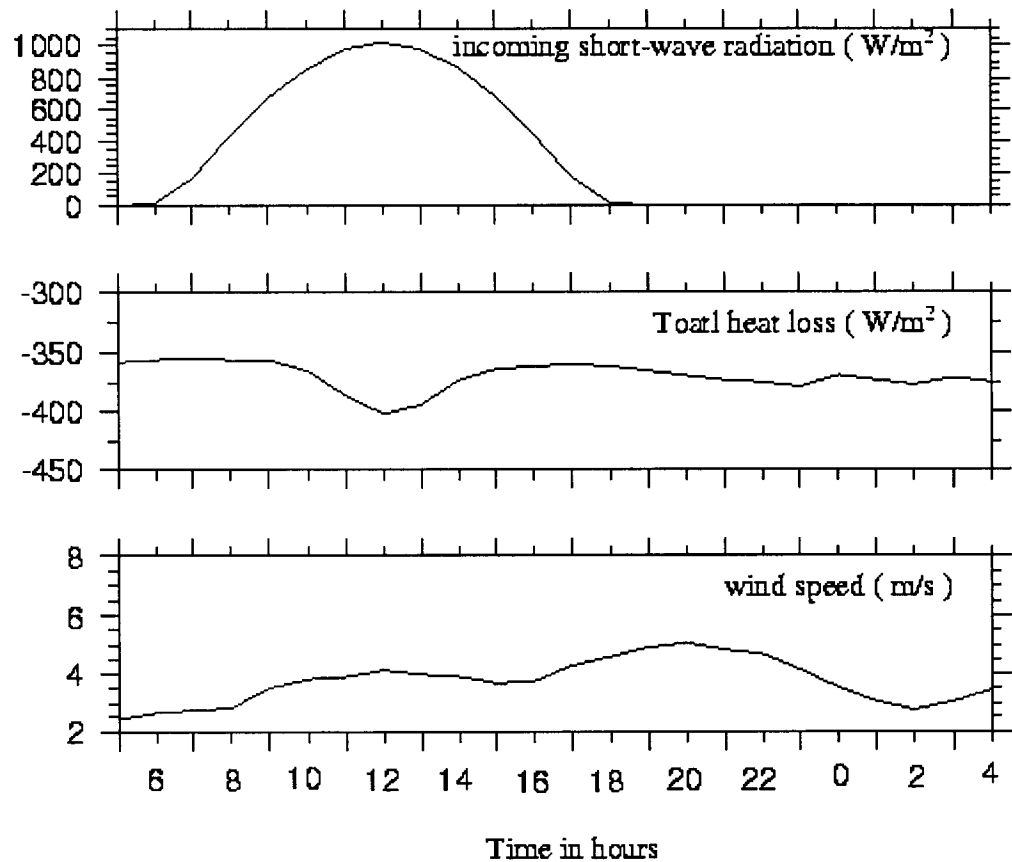


Fig. 4.9: Typical one-day diurnal cycle of the radiative and wind forcing to the model. parameters only solar radiation had large variations with time. Total heat loss at

4.4.2. Parameterization of radiative forcing

Solar irradiance at the ocean surface at a particular time step of the model run is computed by fitting a *cosine* curve over time with noon radiation as amplitude factor (Fig. 4.10). Thus one day solar cycle corresponds to one *cosine* curve, keeping the first and last quadrant fit for duration of sunshine hours, the remaining part is assigned to night and is equated to zero (since direct solar heating from upper hemisphere is negligible).

The radiation I at the surface is computed by using equation 4.10 for a particular time t , by considering the noon radiation I_0 .

$$I = I_0 \cos\left(\frac{2\pi t}{T}\right) \quad (4.10)$$

where T corresponds to 24 hours.

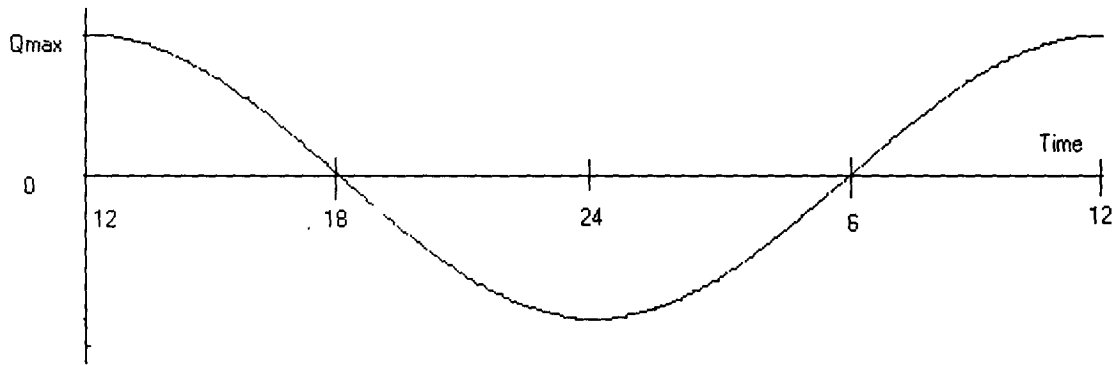


Fig. 4.10: Model solar cycle.

Using the noon radiation on 20th October 2004 and hourly observations of incoming shortwave radiation for that day verify the equation 4.10. The result is shown in Figure 4.11. The solid line represents the observed incoming shortwave

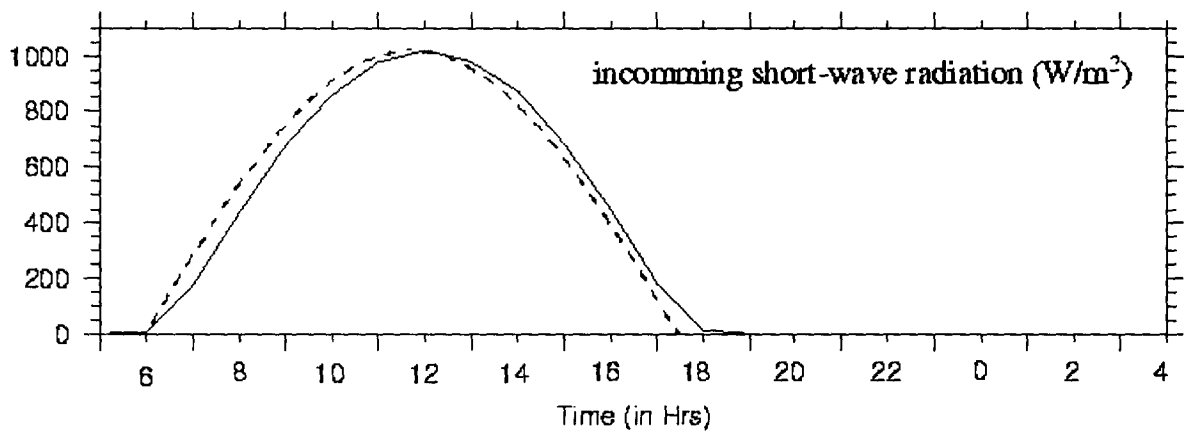


Fig. 4.11: Comparison of solar cycles.

radiation, where as the dotted line represents the derived value by using equation 4.10. On comparison day the observed noon radiation is 1018 Wm^{-2} .

Using the day average of shortwave radiation over the sea surface a solution for obtaining the noon solar insolation, the radiation at the ocean surface when the sun is at 90° with respect to the sea surface, is given below.

$$I_0 = 24 * Ar * \left(\frac{2.134}{24} \right) * \sin \left(\frac{2.314 * D_{sh}}{24} \right)^{-1} \quad (4.11)$$

where, Ar is the average solar radiation over 24 hours. D_{sh} is the duration of sunshine hours and I_0 corresponds to the noon solar insolation.

4.4.3. Validation of noon radiation

The above formula is (Equ. 4.11) verified with the buoy observations. The comparison between the *in-situ* and the estimated noon radiation is represented in figure 4.12. To better appreciate the results are shown on monthly basis.

The over all performance shows computation is under estimating with respect to the actual values. The one-to-one agreement found for the months April and May and relation is poor for the months December, January and February in addition they possess nearly similar distribution. The root mean square error cited in the plot signifies after removal of bias. The maximum root mean square error is ($>50 \text{ Wm}^{-2}$) found for the months April, July, August and October. Root mean square error is least during May.

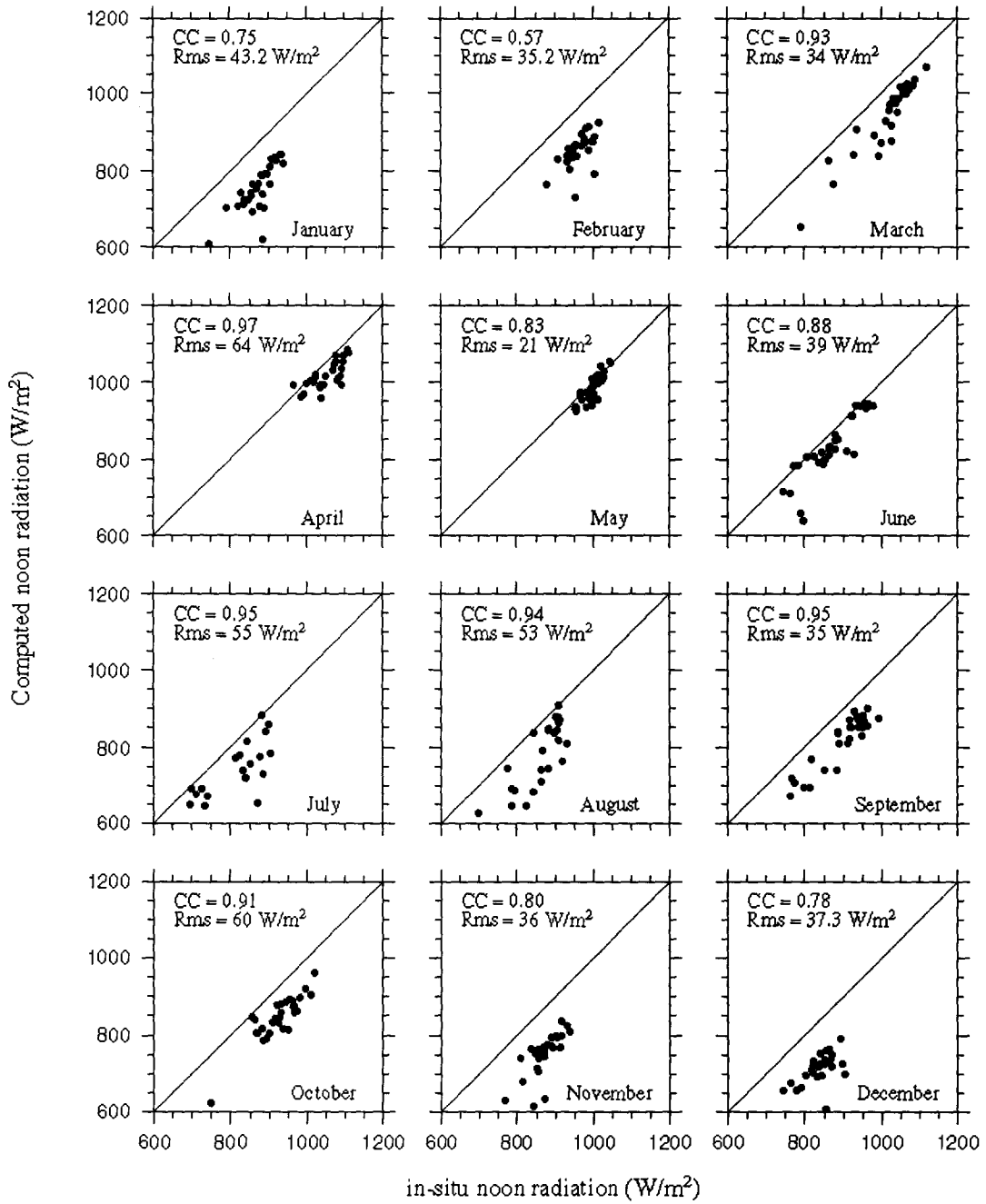


Fig. 4.12: A comparison of in-situ noon radiation over the ocean surface to the noon Radiation computed from equation 4.11 using daily averaged radiation value.

Note: CC refers to Correlation coefficient.

Rmse refers to root mean square error after bias removal.

4.4.4 Parameterization of ocean turbidity

Knowledge of the vertical distribution of solar radiation in the upper ocean is important for modeling the physical, the chemical and the biological processes. The principal physical application is modeling the heating of the upper layers by absorption of solar radiation. The assumption often used (eg., Denman, 1973) is that the downward irradiance is an exponential function of depth given by

$$I = I_0 e^{-z/\zeta} \quad (4.11)$$

Where I , the downward irradiance, is the radiant flux density (energy per unit area per unit time) on a horizontal surface due to contribution from the entire upper hemisphere, I_0 the incident, less reflected and emergent irradiance at the surface, z the vertical coordinate positive upward with origin at mean sea level and ζ the attenuation length. Upward irradiance, due to back scattering, ranges from about 0.3% to 3% of downward irradiance and is neglected assuming that optical properties of the upper ocean are independent on depth, a reasonable approximation in the surface mixed layer (Denman, 1973).

The assumption of an exponential decay with depth is a poor approximation in the upper 5m of the ocean because of the preferential absorption of the shortwave and longwave components of sunlight. Below depth of 10m, however the assumption of exponential decay is a good approximation because the preferential absorption above left only blue-green light. These facts concerning the distribution of light in the upper ocean have long been known (eg., Jerlov, 1968). Another aspect of modeling the distribution of solar radiation is the variation of optical

characteristics with depth, geographical location and season. As mentioned in the earlier an indirect method is attempted in this work to quantify the turbidity of the seawater.

4.5 Seasonal variability in attenuation coefficient and chlorophyll concentration over Indian Ocean

The downwelling solar radiation heats the upper ocean; the degree of heating depends on the ability of its penetration or its attenuation with respect to depth. The space-borne ocean color sensor has the potential of giving the information on chlorophyll distribution. In this analysis chlorophyll concentration is used to classify the water type over spatially and temporal (seasonal) basis. Here coastal zone color scanner (CZCS) derived chlorophyll concentration used to classify the Indian Ocean waters. Coastal zone color scanner was the first flown sensor for the monitoring of the above parameter (1978-1986). Watson and Margarita, (2000) used Reynolds and Smith, (1994) technique for mapping the chlorophyll over global Oceans. In a blending method both the *in-situ* as well as the satellite information is injected in order to generate seasonal chlorophyll concentration. The following pages explain the method of water type classification.

The extinction length corresponding to blue-green light is derived from chlorophyll concentration after following Parsons et al., (1984) method,

$$\lambda_2 = 0.04 + 0.0088 chl + 0.0054 chl^{2/3}$$

where, *chl* is the chlorophyll pigment concentration.

The spatial and seasonal variability of chlorophyll pigment concentration (right panel) and thus estimated extinction length (left panel) is shown in the figure 4.13.

Season 1:

Season 1 refers to the months January, February, and March. During this period, northwestern Arabian Sea depicted with higher concentration ($>0.6\text{mg m}^{-3}$) and most of Arabian Sea is covered with 0.2mg m^{-3} chlorophyll values. The extinction length of shortwave component is less in correspondence to higher water constituents. The reverse occurs for lower values. Though the solar energy observed in a shallower depth, the climatic mixed layer depth maximum values are found over this region. Unlike Arabian Sea, Bay of Bengal shows different nature for this parameter. Bay of Bengal resembles with low chlorophyll concentration and hence higher extinction length for shortwave solar component are found those regions. The lowest chlorophyll concentrations are found from coastal zone color scanner seasonal data set over the southern Indian Ocean and consistent with 0.5mg m^{-3} and the corresponding λ_2 were 22m.

Season 2:

Season 2 refers to the months April, May, and June. A major change occurs in case of Arabian Sea with respect to chlorophyll and water types. The higher chlorophyll concentration over northwestern Arabian Sea decreased considerable from season 1. As a result, the extension length of shortwave component increases from 12m to 20m depth. Almost Arabian Sea depicted with uniform chlorophyll

concentration values (approximately 0.1mg m^{-3}). Analogous to Arabian Sea, seasonal variability in chlorophyll is very minimal over Bay of Bengal at this season while compare to previous season. However there shown an indication for increasing chlorophyll value over regions of southern ocean.

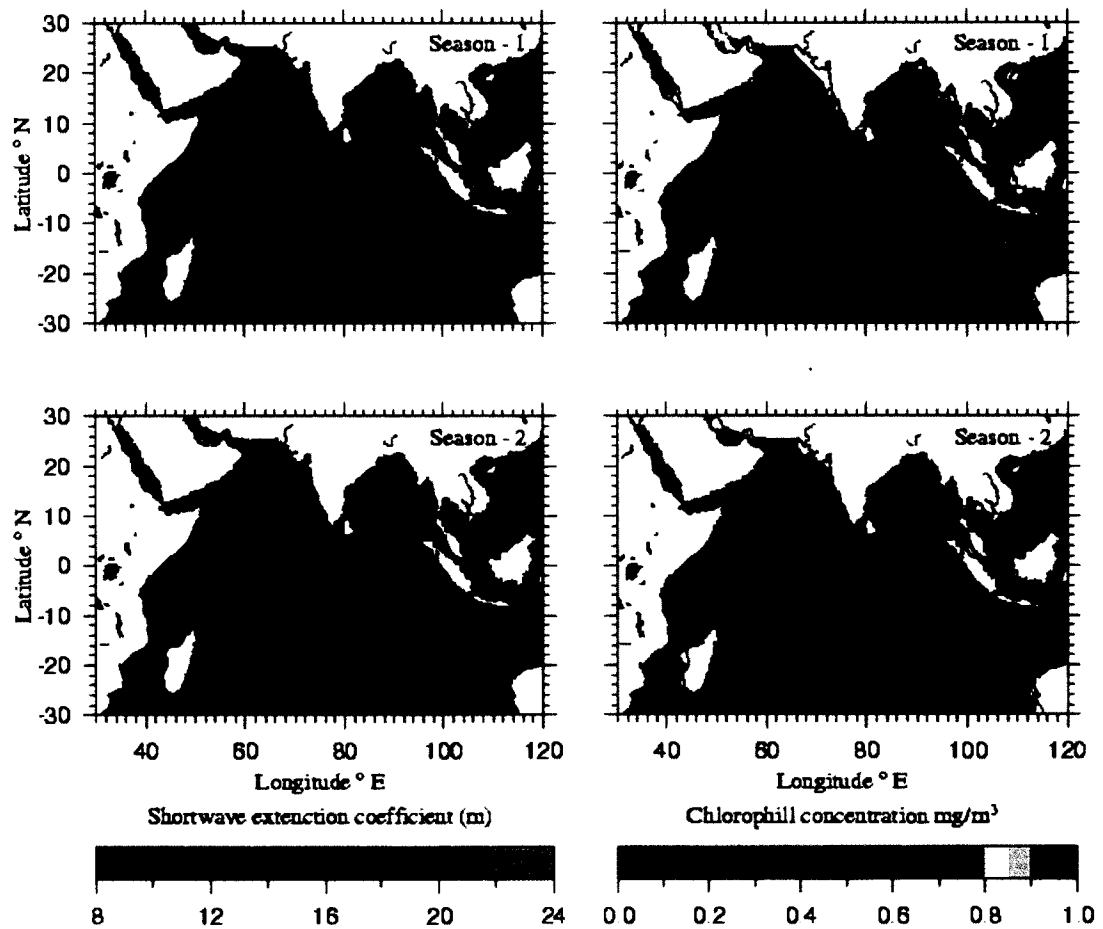


Fig. 4.13 (a): Seasonal distribution of chlorophyll concentration, and short-wave extinction coefficient.

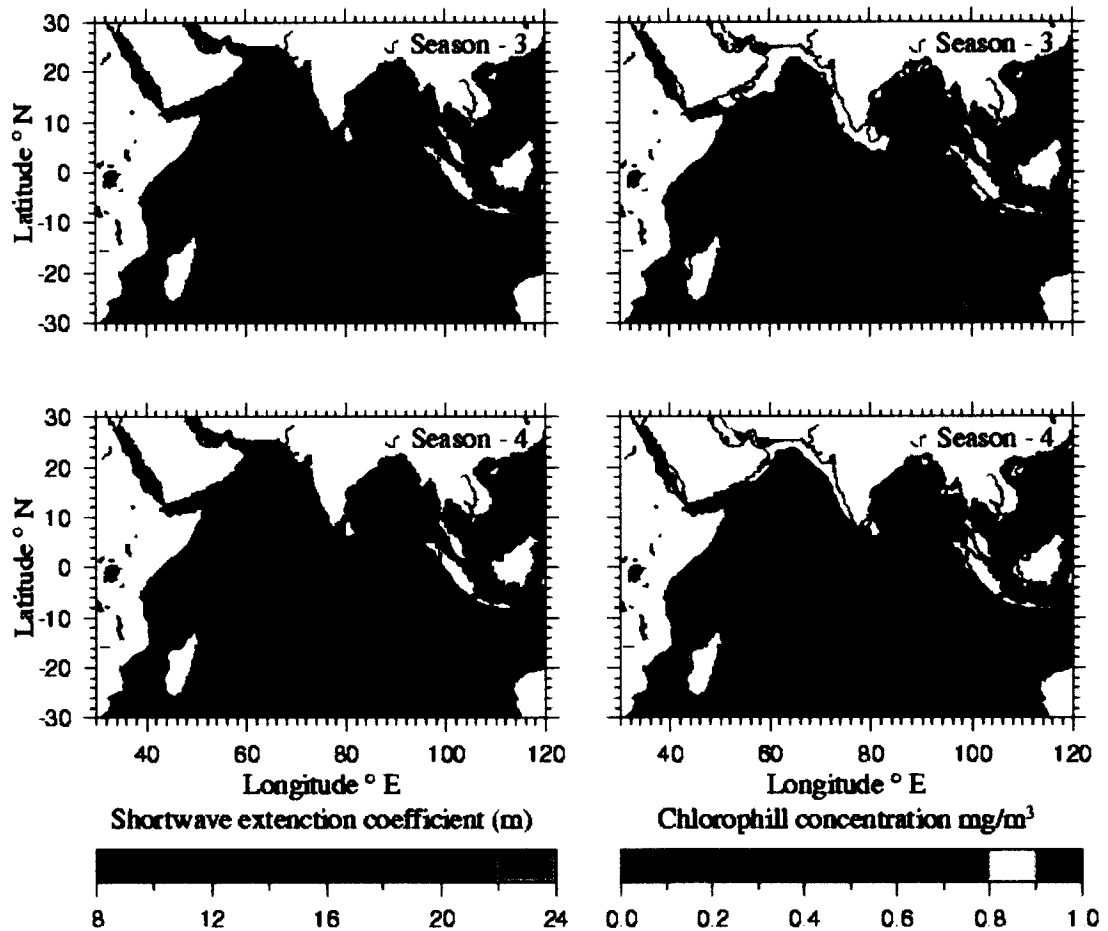


Fig. 4.13 (b): Continuation ...

Season 3:

The months July, August, and September are referred to season 3. Maximum chlorophyll values are observed in this season over Arabian Sea and are maximum in annual time frame. The values higher than 1 mg m^{-3} are not shaded. The Somalia coast facilitated with intense upwelling and horizontal advection, which ultimately favor for chlorophyll growth. The biology of Bay of Bengal changes considerable during this season with reference to other seasons. Most part of coastal Bay of Bengal covered with higher chlorophyll of concentration $>0.6 \text{ mg m}^{-3}$. The waters over southern Sri Lanka also dramatically changed in this period

of time. The regions south of 15°S showed uniformity with 0.1mg m⁻³ values and corresponding λ_2 were 20m.

Season 4:

The months October, November, and December are referred to season 4. This season covers post southwest monsoonal and winter monsoonal time frame. The high biology growth over south Sri Lanka Sea is changed to normal picture. The aerial extent of maximum chlorophyll values over Arabian Seacoasts are decreased compared to season 3. Bay of Bengal bounces back to its season 1 chlorophyll concentration values. The southern ocean regions had 0.1mg m⁻³ chlorophyll values.

4.6 Model run with constant and variable biology

The track wind data of the ERS scatterometer winds were used to generate daily fields. The daily data had many gaps, which were filled in two steps: first by performing a 3-day running average and then, in the second stage, by filling the residual gaps by an inverse interpolation technique. Seasonal chlorophyll data derived from the coastal zone color scanner were used to account for variable biology in the present study. Monthly climatological data of heat loss and noon solar radiation at the ocean surface are taken from comprehensive oceanographic and atmospheric data set of Da Silva et al., (1994).

4.7 Validation of ERS Scatterometer Winds

To examine how well ERS wind speeds replicate the actual winds, comparisons were made with the surface mooring observations in the Arabian Sea. The ERS winds are given at a standard height, 10m, whereas the buoy data is at 3m height from the sea surface. Using a logarithmic approach following Mears et al., (2001), the data buoy measurements were first converted to 10m neutral stability wind speeds. Figure 4.14 shows the daily time series of these two wind products from

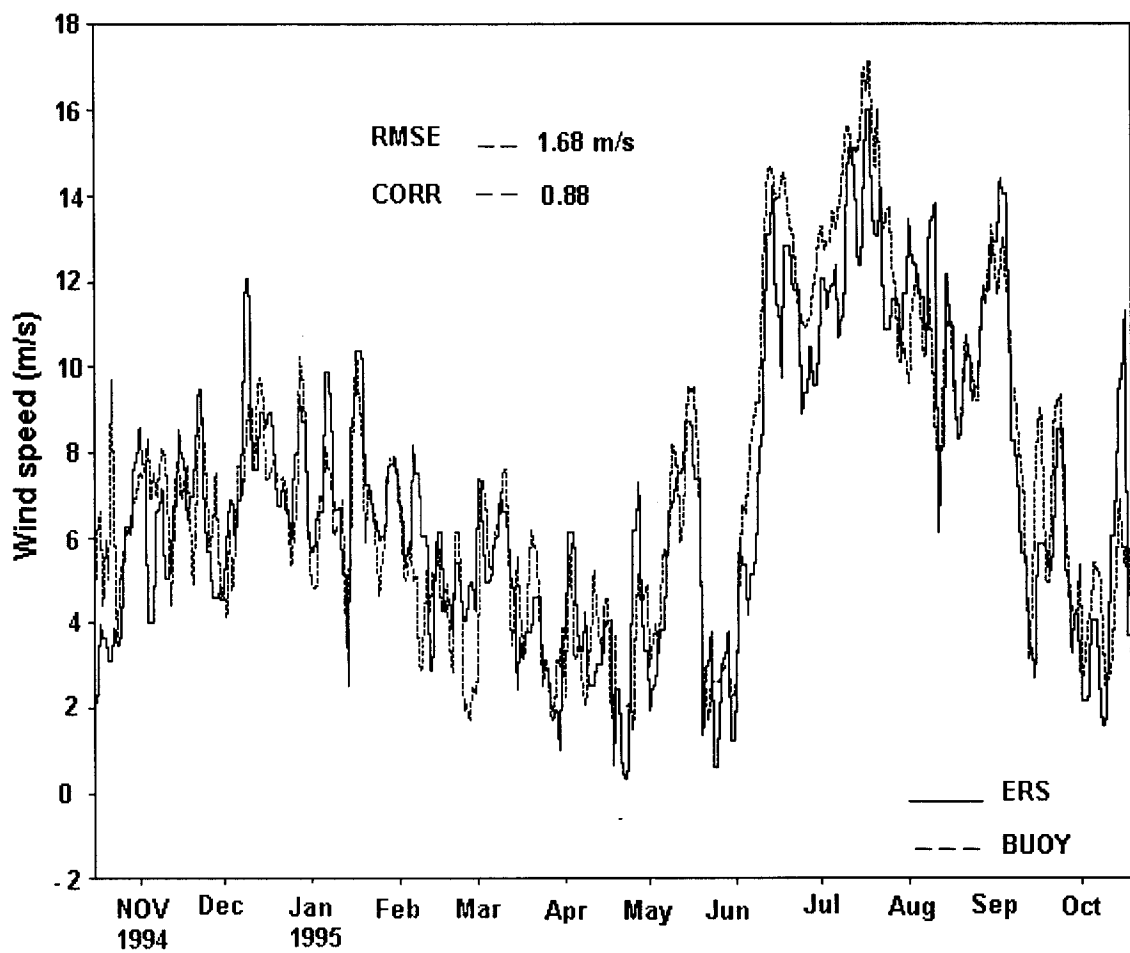


Fig. 4. 14: Time series of the daily averaged ERS scatterometer wind speed (dashed line) and observed daily averaged wind speed (solid line) at the mooring site (15.5° N and 61.5° E).

October 1994 through October 1995. The wind speeds range from 1 to 17ms^{-1} over the period of comparison. During the southwest monsoon season (June 1995 through August 1995), when the winds are quite strong, the ERS winds are quite close to the observed winds. The root-mean-square difference between the two series is 1.68ms^{-1} , with correlation of 0.88. However, there are some isolated peaks in both the series. However, overall the ERS wind speeds are close to the observations.

4.8 Analysis of the Model Simulations

The model ran for a period of 2 years (1994–1995), and the density profiles obtained were diagnosed to quantify mixed layer depth variability. For the same period, the model is also run without including variability in biological heating, i.e., with constant extinction depths of 0.6m and 20m for the red and blue-green components, respectively, as typical of clear water. In each of the 1m layers, change in heat is computed from the vertical mixing of heat between adjacent layers as well as the solar radiation profile. At each time step (900s), solar radiation is absorbed according to equation (4.4) and the heat loss and fresh water flux are extracted from the surface. The density profile is then computed and adjusted to achieve static stability, if required. From these profiles, using the density criterion (mentioned in the previous section), mixed layer depth is obtained. Here mixed layer depth with constant biology is denoted by MLD_{cb} , which with variable biology by MLD_{wb} and the *in-situ* (based on ocean observations) mixed layer depth by $\text{MLD}_{\text{insitu}}$.

During 1994–1995, a large (~700) number of conductivity temperature depth observations were collected as part of Joint Global Ocean Flux Studies experiment in the Arabian Sea and also by the World Ocean Circulation Experiment program. Model results are validated with these observations. There is a definite improvement by including biology in to the model. The root mean square error reduced from 17m to 14.9m. The scatter between mixed layer depth simulated using variable biology and mixed layer depth from *in-situ* profiles has shown in figure 4.15. The coefficient of determination (R^2) is about 0.66.

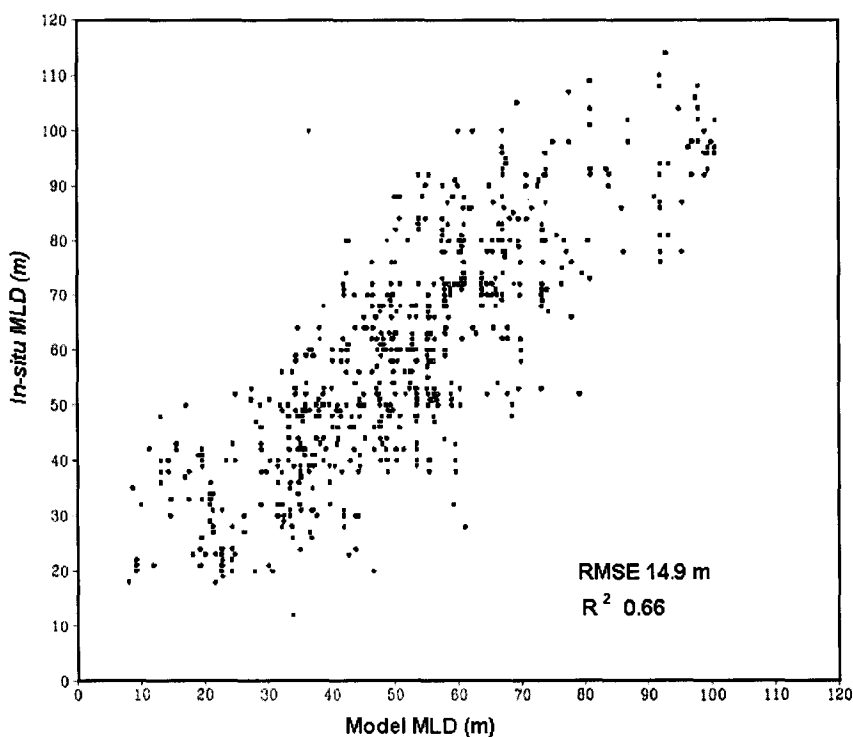


Fig. 4. 15: Scatter plot of MLD simulated with variable biology versus observed MLD from CTD observations.

4.9 Evolution of MLD in the Central Arabian Sea

Figure 4.16 shows an annual evolution of simulated MLDs (with and without biological heating) and the observed mixed layer depth at the mooring location.

Also the time series of extinction depth derived from the coastal zone color scanner chlorophyll maps and wind speed showed in the same figure. The reason for plotting these two parameters is to see the relative importance of biological heating and wind speed on mixed layer depth. Mixed layer depth clearly shows a semi-annual oscillation: (1) one maxima during January–March due to convective mixing because of winter cooling (Shetye, 1986; Rao and Mathew, 1990; Rao and Sivakumar, 1998), where there is not much effect of wind and biological heating, and (2) a second maxima during July and August, where there is competitive effect of high winds and high chlorophyll abundance. The extinction depth is very small (12m) during July and August, due to high chlorophyll content. This is in agreement with the earlier finding by Sathyendranath et al., (1991). In the Arabian Sea, chlorophyll concentration peaks in August (3mg m^{-3}) due to the summer plankton bloom induced by coastal upwelling. A higher abundance of chlorophyll increases the absorption of solar radiation and heating rate in the upper ocean, resulting in decreasing the mixed layer thickness (Babu et al., 2003). Although the pigment concentration is high during July, the mixed layer depth is deep; this is due to the high wind speed leading to higher turbulence and increased mixed layer depth. However, during August, due to a drop in wind speed, the effect of biological heating overcomes the wind mixing effect, which leads to shallow mixed layer depth (Babu et al., 2004). Here, MLD_{wb} values are very close to $\text{MLD}_{\text{in_situ}}$, whereas the same is not brought out in MLD_{cb} . In the month of March, there is a large discrepancy between simulated (constant and variable biology) and observed mixed layer depth. A sudden deepening in the mixed layer depth

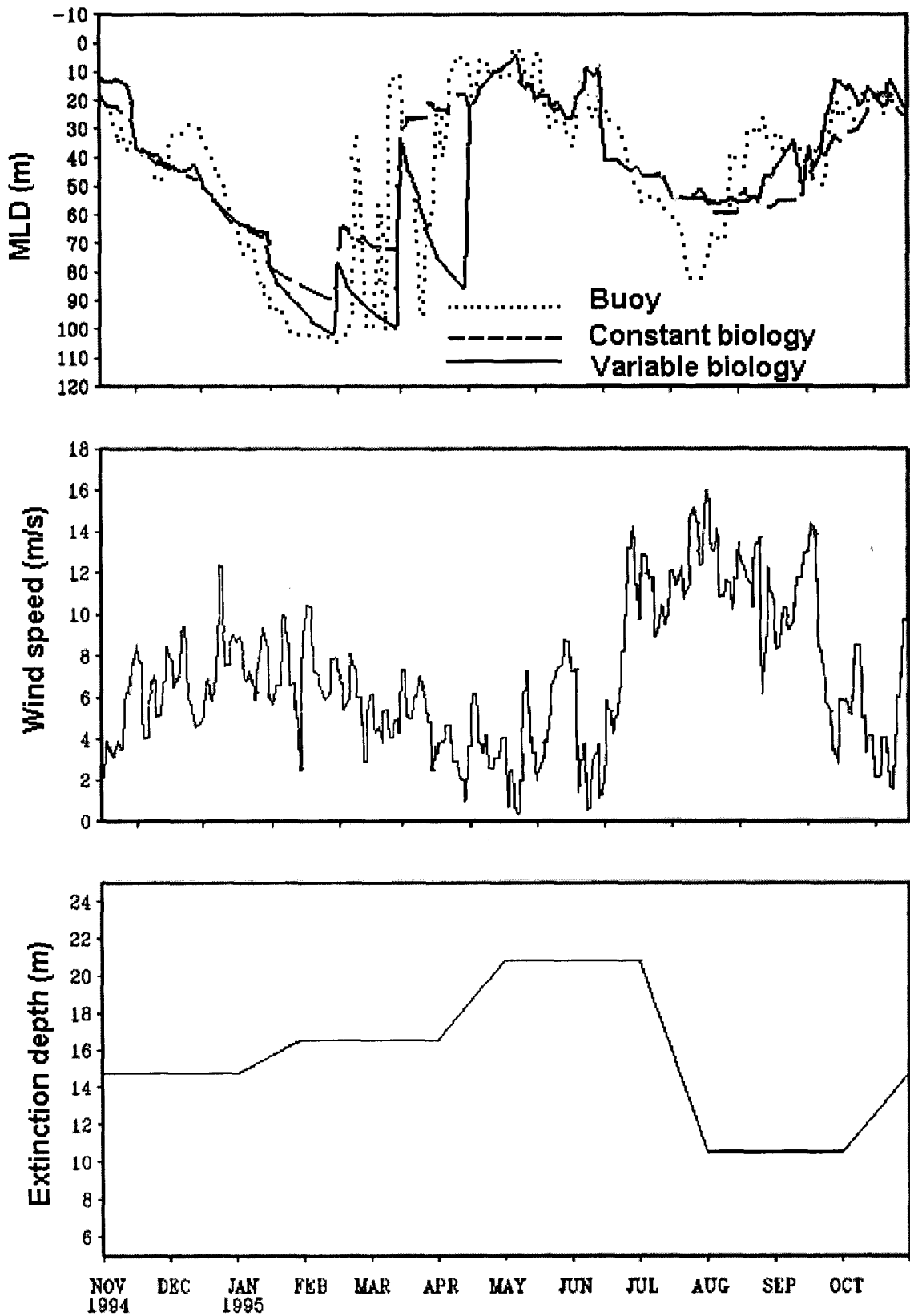


Fig. 4. 16: (a) Annual changes of MLD at the central Arabian Sea (15.5°N and 61.5°E) simulated from model with constant (dashed line) and varying biology (solid line), and MLD from *in-situ* observations (dotted line). Time series of (b) wind (ms^{-1}) and (c) extinction depth (meters).

occurred around mid-March in the observations. MLD_{wb} becomes deeper, but toward the end of the month, whereas MLD_{cb} remains shallow throughout March. This lag of around 15 days in the simulated mixed layer depth with variable biology is definitely not due to the chlorophyll effect. Also, the mooring data demonstrated that this is not a period of strong advection. It may be that heat flux has a role to play here; however, the reason for this lag is not clear. Overall, there is a reduction in the root mean square error from about 15m to 12m in mixed layer depth at the buoy location after the inclusion of the seasonal chlorophyll data in the model run.

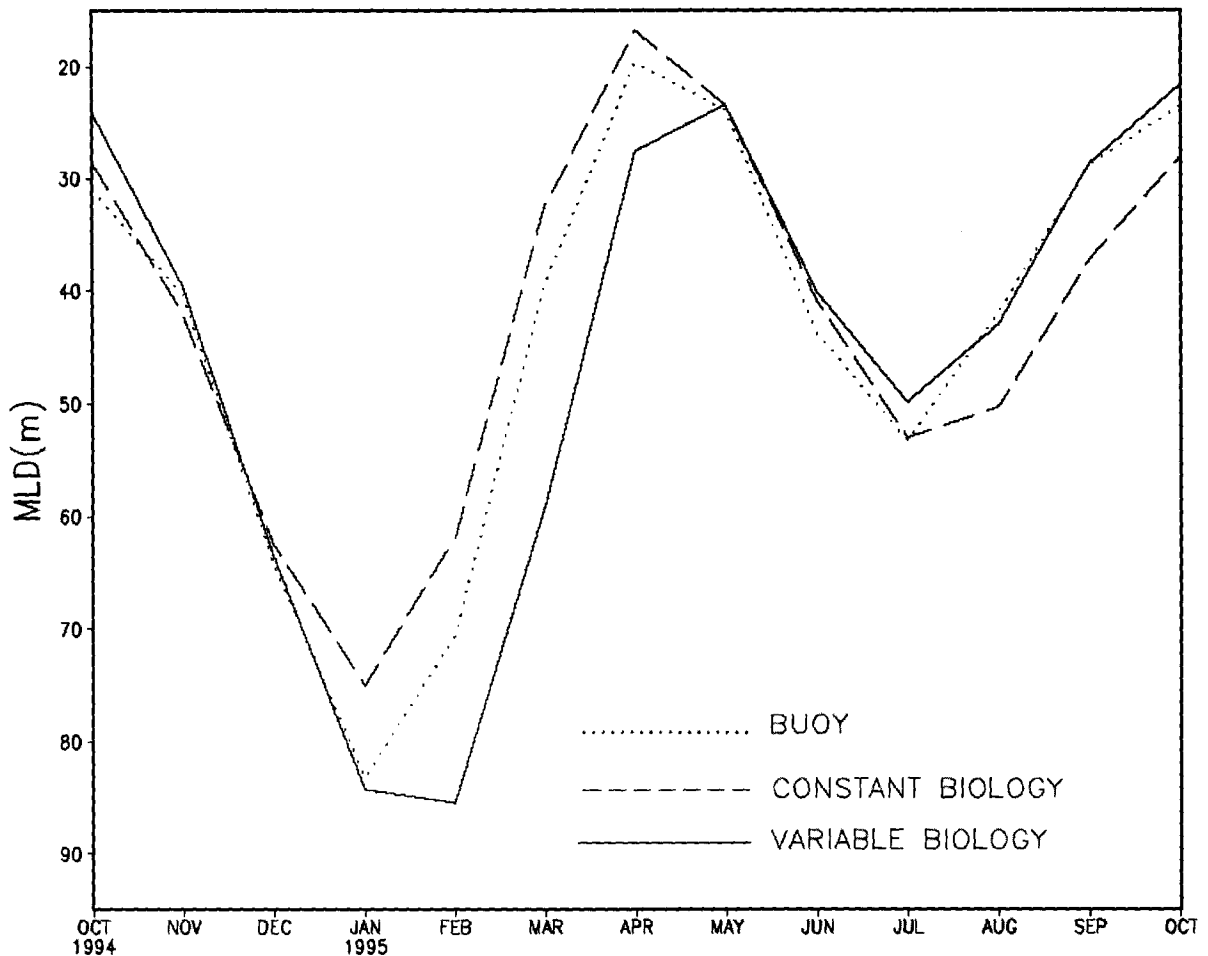


Fig. 4. 17: Monthly averaged mixed layer depth at the central Arabian Sea (15.5°N and 61.5°E) simulated from model with constant and varying biology. Also shown is the MLD from *in-situ* observations.

Since seasonal mean chlorophyll data were used to model the effect of biological heating, it is thought appropriate to compare simulated MLDs with observed values on a monthly averaged basis. Figure 4.17 shows the time series of monthly averaged MLD_{insitu} , MLD_{cb} , and MLD_{wb} . As it can be seen, the maximum impact of biological heating is observed during August and September, and overall, there is a definite improvement in the model-simulated mixed layer depth when variable biology is used. The next section extends the study to the entire tropical Indian Ocean by examining the differences in the two simulations (MLD_{cb} and MLD_{wb}).

In the previous sections it had shown that at the Woods Hole Oceanography Institution data buoy location; MLD_{wb} is closer to MLD_{insitu} than MLD_{cb} . For this reason, it will be appropriate to investigate the temporal and spatial characteristics of the difference between the two mixed layer depth estimates in detail. In Figure 4.18, we present the difference between the two MLDs for 4 months (January, May, August, and November of 1994) representative of the winter, pre-monsoon, monsoon, and post-monsoon seasons. The most obvious characteristic is that the difference is less than 10 m at most of the places in Tropical Indian Ocean. However, an exception to this is the Arabian Sea, where a large difference in the two estimates is seen. The differences are seasonally varying, being largest in August. During this season, the estimates differ by as much as 40m in the central Arabian Sea and also near Somalia. In May also, the two simulated MLDs in the

central Arabian Sea show large difference ($>10\text{m}$). This implies that the impact of biological

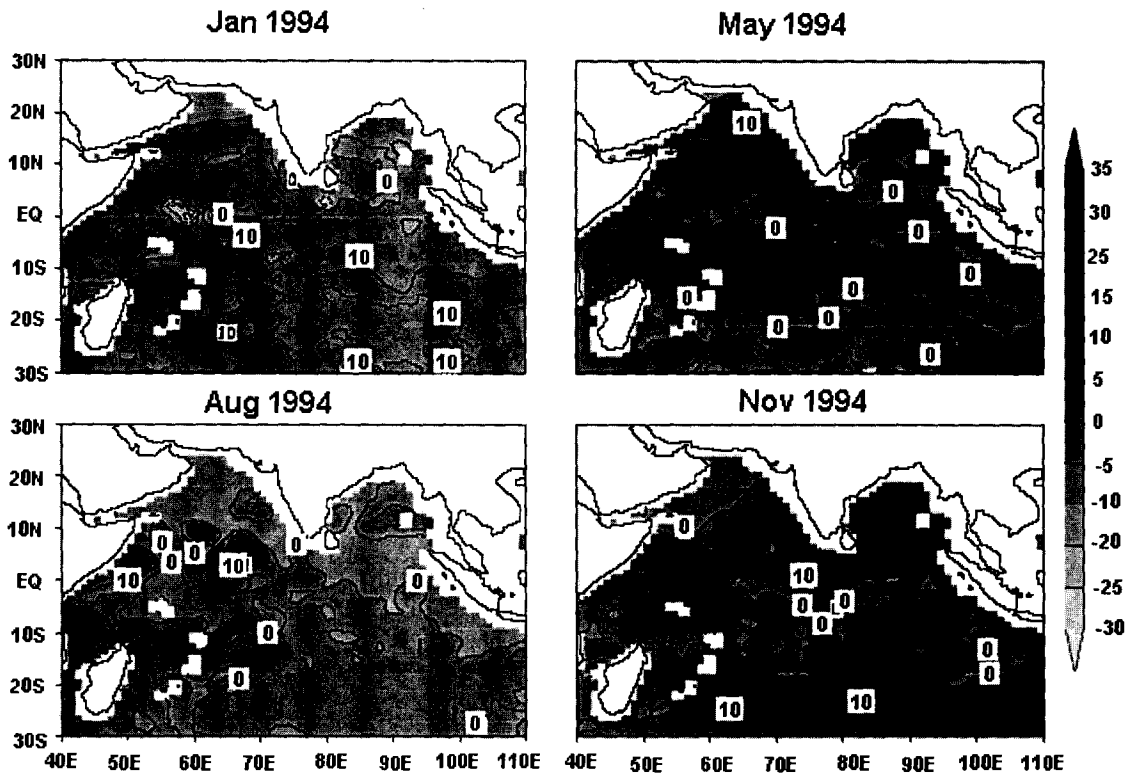


Fig. 4.18: Distribution of difference of the two MLDs (simulated using constant and varying biology) over the study area during January, May, August, and November of 1994.

heating is quite significant in the Arabian Sea. In contrast, relatively small differences are obtained for the Bay of Bengal. Probably other processes, in particular fresh water discharge, control the mixed layer depth in this region more than the heating due to chlorophyll.

4.7 Summary

The model is able to estimate the mixed layer depth on the daily averaged surface forcing even though the governing equations are of diurnal in nature. Sensitivity

analysis of the model shows wind is the most effective parameter in the evolution of mixed layer depth. The solar cycle is modeled from the noon radiation. The noon solar radiation calculated from the daily averaged net short wave radiation is having considerable relation with the observed noon radiation. This information can be extracted with the help of the analysis and the other forcing from remote sensing observations.

The Arabian Sea is known as a place of especially high primary productivity, and so selecting constants (for Equ. 4.10) for clear water may not be true representative. But as the primary concern is with periods of deepening, where the mixed layer is generally deep enough to neglect a solar heating flux through its base, this is not a major concern (Fischer, 2000). It may become important in examining periods of restratification with shallow mixed layers. In the case of fairly clear mid-ocean water (type-1), which here assume holds for central Arabian Sea during the sensitivity analysis and one-year model computation period. The clarity of the ocean water leads to the solar penetration, and hence the heating of the upper ocean depends up on the seawater type. The information derived from coastal zone color scanner shows a maximum of 12m depth in the mixed layer depth estimation with and without the water type classification.

Chapter V
Seasonal variability of mixed layer depth

5.1 Introduction

The study region (northern Indian Ocean) is known to be fairly dynamic oceanographically (Flagg and Kim, 1998; Kumar et al., 1998). Recent publications were concentrated mainly on upwelling during the southwest monsoon along the coast of Oman (Quarishie, 1984; Manghnani et al., 1998; Shi et al., 2000). Lee et al., (2000) have investigated the seasonal and spatial variability of mixed-layer depth in the northern Arabian Sea in response to summer (southwest) and winter (northeast) monsoonal forcing. He suggested that wind driven entrainment, coastal upwelling, and offshore advection are all important factors that determine the ocean response to monsoonal forcing along the Omani coast and that Ekman pumping is relatively weak. Satellite data further confirm that the northern Arabian Sea and Gulf of Oman are dynamic, and dependent, at least to some extent, on the annual monsoon cycle (Stapleton et al., 2002). However, compared to the tropical Pacific or the North Atlantic, the Indian Ocean is very little understood. The tropical Indian Ocean is one of the essential regions where El Nino Southern Oscillation in the tropics and the Asian monsoon system interact (Webster and Yang, 1992).

There are many mathematical tools available for separating the seasonal signals from a long-term record. Empirical Orthogonal Function (EOF) is often used for this purpose in the present study. Like Fourier transforms, EOFs are a mean of decomposing a signal into its constituents (orthogonal components). They are also a form of Principal Component Analysis (PCA) (Preisendorfer, 1988; Mitchum,

1993) of data. The method depends on finding Eigen functions of the covariance function of the variable, it is also called proper orthogonal decomposition (POD; Lumley, 1971; Berkooz et al., 1993) while Fourier transform uses universal global function for decomposition, EOFs use specific basic functions that are unique in that particular data set and therefore do not always apply to a different data set. In fact, often, small changes in the composition of a data set can cause significant change in the EOFs. EOFs constitute the most optimum means of decomposing (and reconstructing) a data set, made possible by the fact that they are orthogonal to each another. They can also be looked upon as the most efficient way of characterizing a time series of data set. The EOFs are an ordered set in that the first one contains the most variance, the second one the second most, and so on, so that by truncation at a particular level, it is possible to retain only the most essential components of the signal (and reconstitute it appropriately). Thus they can be used for data compression purpose as well. They are called empirical, since they are derived from the data set itself. They are the most efficient approximation to a data set possible, in the absence of any a priori knowledge of the actual principal components of the data set. As they are not require any a priori knowledge on the pattern of variability, examples of application of EOFs to oceanic data set Hendricks et al., (1996) and Nerem et al., (1997). EOFs analysis is only applicable to the time-dependent spatial fields of a single variable. Theory, data preparation and the results are described in the following sections.

5.2 Hovmoller diagram of mixed layer depth

Hovmoller diagram (Space-time) is the best way to infer any propagating features. Figure 5.1 shows the zonal section of model derived mixed layer depth at latitude of 15°N over a longitude range from 50°E to 70°E . This section lies in central Arabian Sea, which normally under goes most of the dynamic changes due to monsoonal wind reversal. Mixed layer depth exhibits bimodal oscillation, two maxima and two minima in a year. The first maximum occurs during December-February, where the mixed layer depth as a result of convective mixing deepens more than 95m. However, the inter-annual variations during this time are not prominent. This could be due to the stable structure of mixed layer depth, which is affected only on a longer time scale. Stating that convective mechanism leading to mixing is not the same every year during this time. The second maximum of mixed layer depth is observed during southwest monsoon period of wind mixing event. One emerging difference of these two maximums is in their spatial extent. The first maxima (winter) covers the entire Arabian Sea (50°E - 70°E), where as the second maxima has spatial coverage only up to 57°E , starting at 70°E . This could be because of the upwelling near west coast of Arabian Sea, which is very prominent during southwest monsoon season and leads to shallow mixed layer depth. Another important point to note is the merge of two maxima towards eastern Arabian Sea. The central Arabian Sea exhibits prominent nature of deepening and cooling of mixed layer. Bay of Bengal, on the other hand, also shows twice-yearly variations but with lesser values and also with lesser aerial coverage. This is because of the complex nature of different forcing,

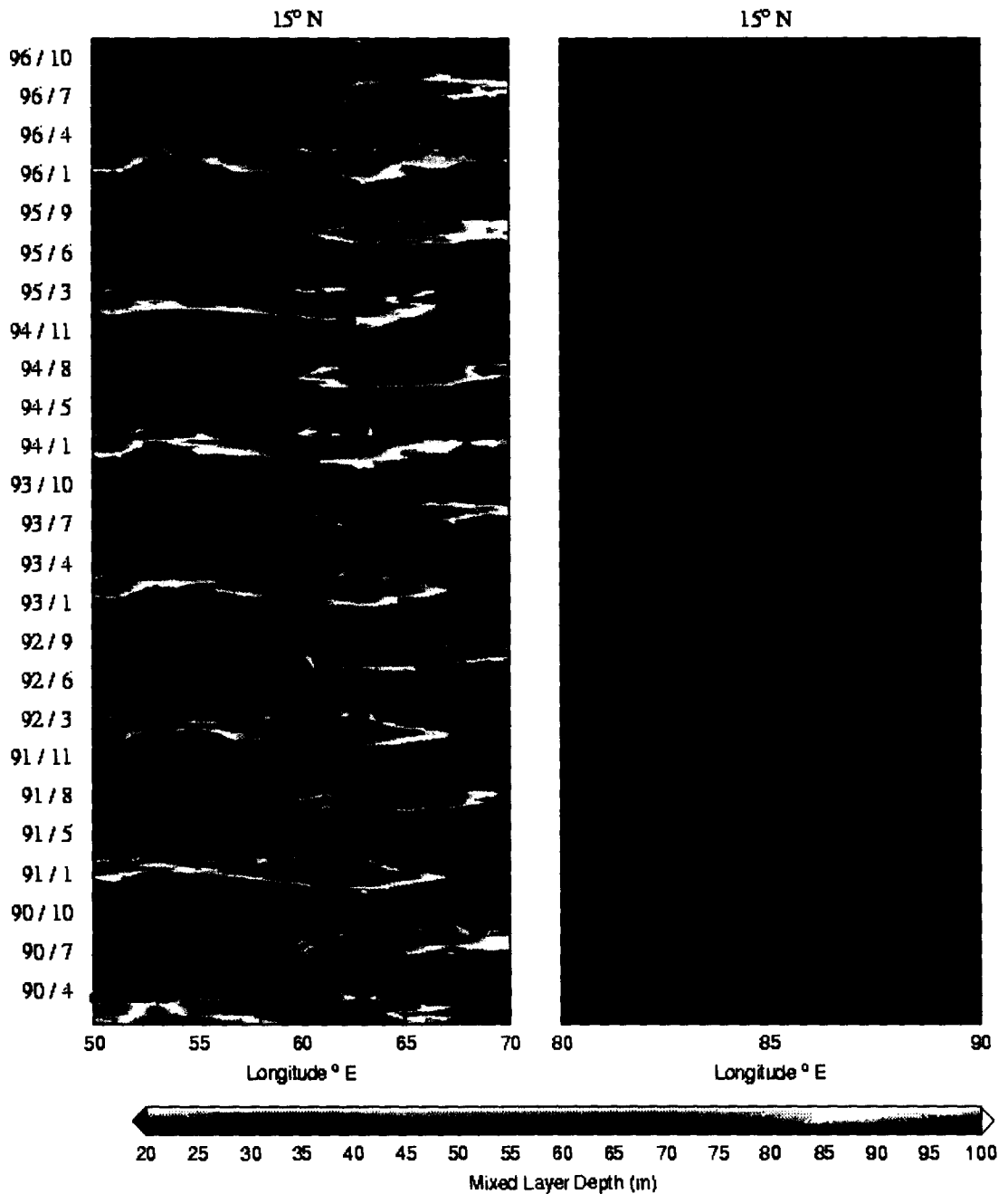


Fig. 5.1: Havmoller plot of MLD over Arabian Sea and Bay of Bengal along 15° N.

which affects the upper ocean thermal structure differently than Arabian Sea. The smaller domain of Bay of Bengal along with intense river discharge is few reasons for the complexity. The impact of winter cooling is seen over Bay of Bengal, over

this region, maximum is observed towards the western side. The second impact of maximum mixing is found during the summer monsoon.

5.3 EOF analyses of MLD

Any dynamic variable has different spatial and temporal components. The dynamical behavior of complex system is often dominated by interactions between a few characteristic 'patterns'. Hence it is essential to decompose this physical field into few dominant interactive patterns of different time scales. A standard strategy is to devise a simple analog system from such complex dynamical system, which, nonetheless, can capture all the essential properties of the full system. The basic technique is: the reduced dynamical model is constructed by finding the optimal model, within a given model class, which best fits the data in a generalized least square sense. This has been accomplished using EOF (Empirical Orthogonal Function). The theory is taken from Hasselmann, (1988).

Theory

A physical field is described by state variables, which are functions of space and time. Let us have a variable $X(r,t)$ with r denoting the spatial point and t the time.

For a large system, dominant normal modes will be hard to extract. Hence, data is transformed to EOF space. EOFs are a set of orthonormal functions, which

completely spans the real space and are time invariant. EOFs are given as the eigenvectors of the covariance matrix C .

For M spatial points, the Eigen values and eigenvector equations of the matrix C is written as,

$$C a_i = \beta_i a_i \quad (i=1,2,3, \dots, M) \quad 5.1$$

where, β_i are M Eigen values and a_i corresponding Eigen vectors.

Sum of the Eigen values is equal to the total variance of the field $X(r,t)$ ie.,

$$\sum_{i=1}^M \beta_i = tr(C) \quad 5.2$$

$tr(C)$ is the trace of matrix C and is defined as the sum of the diagonal elements of matrix C .

The EOFs are defined as the Eigen vectors (a_i 's) of the covariance matrix C .

Hence, the data set $X(r,t)$ may be expanded as,

$$X(r,t) = \sum_{i=1}^M \beta_i(t) a_i(r) \quad 5.3$$

If now, we truncate EOF-space to n dimensions, (which will preserve most of the variance, while removing the noise),

$$X(r,t) \implies x(r,t) = \sum_{i=1}^n \beta_i(t) a_i(r) \quad 5.4$$

The Eigen value β_i describes the variance associated with the i^{th} empirical orthogonal function a_i . If $(\beta_i, i=1,2,\dots,n)$ are arranged in decreasing order, the first empirical orthogonal function accounts for most of the total variance, the second

empirical orthogonal function accounts for most of the variance in the field excluding the first empirical orthogonal function, and so on. An empirical orthogonal function gives the description of the space structure of the physical field and the corresponding Eigen value indicates how much variance is explained by this empirical orthogonal function.

Data preparation

Empirical orthogonal function analyses need the data in a specified format. This section describes how the data sets have been prepared. Seven years (1990-96) of model derived mixed layer depths have been used to extract few dominant patterns using empirical orthogonal function technique. The study area is divided in to two regions, one in AS and the other in Bay of Bengal. The grid spacing is $1^\circ \times 1^\circ$ and 5 days in longitude, latitude and time, respectively. The length of the time series is 510 (corresponding to 2550 days with 5-day interval).

In order to extract oceanic signals of the desired frequencies, the data set is filtered. Here the Fourier filtering by finite Fourier transformation (Gallagher et al., 1991) used, with defined four filtering parameters $P(max)$, $P1$, $P2$ and $P(min)$ with cosine tails, this reduces the noise level.

$$\begin{aligned}
 &0, && \text{if } v < v_{\max} \\
 &\{1 + \cos[\pi(v - v_1)/(v_1 - v_{\max})]\}/2, && \text{if } v_{\max} < v < v_1 \\
 G(v) = &1, && \text{if } v_1 < v < v_2 && 5.5 \\
 &\{1 - \cos[\pi(v - v_{\min})/(v_{\min} - v_2)]\}/2, && \text{if } v_2 < v < v_{\min}
 \end{aligned}$$

0, if $v_{\min} > v$

where, $v_{\min} = 1/P_{\min}$, $v_{\max} = 1/P_{\max}$, $v_1 = 1/P_1$, $v_2 = 1/P_2$.

The time filter to smoothen MLDs has shown schematically in figure 5.2.

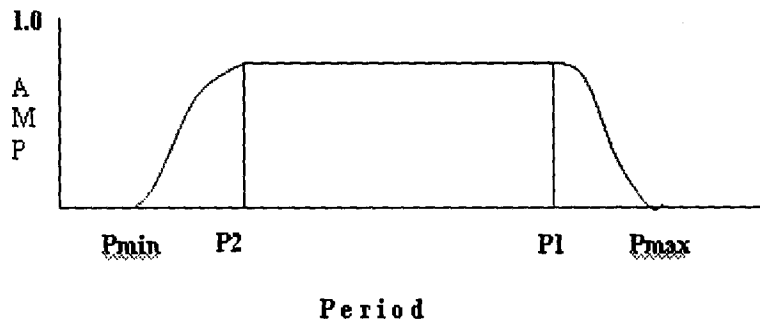


Fig. 5.2: The time filter used to smooth the high frequency and delete the low frequency components in the data.

5.3.1 EOF over Arabian Sea

In order to extract patterns shorter than a year, a band pass filter has to be applied on the physical fields. Here a band pass filter parameters of $P(\min) = 45$, $P(1) = 60$, $P(2) = 185$ and $P(\max) = 205$ days were chosen in separating the signals of this period. The EOFs obtained with the filtered data have been arranged so that the Eigen values are in decreasing order.

Interpretation of univariant pattern is straightforward. Positive and negative lobes are present in the spatial EOFs patterns. In regions in the same sign, temporal variations are in phase; in those with opposite signs they are out of phase. Often two successive EOFs show similar patters, but they are out of phase in one compared to the other. These indicate oscillating features. Naturally, areas of large

amplitudes are also regions of large temporal variability (Kantha and Clayson, 2000).

First two EOFs explain about 84.1% of the variance in the band pass filtered data set with first EOF explaining about 74.7%, and second explain 9.4% of the total variance in the filtered mixed layer depth. Figure 5.3 shows the time series as well as spatial pattern of the first two modes, these EOFs have semiannual periodicity, which is clearly represented in coefficients time series (Fig. 5.3a,b). Among them the variations in coefficient of mode-1 is maximum ranging from -600 to 600 , and the other has variations from -200 to 200 . The first mode (Fig. 5.3c) shows the empirical orthogonal function spatial variation over Arabian Sea. The spatial distribution of the first empirical orthogonal function is characterized by the opposite signs in mixed layer depth between north east of central Arabian Sea and 10° parallel to this. Earlier one with strong negative value of -9 and maximum of 2 , these values are units of 10^{-2} . The more interesting feature of both the signal is they are parallel to one another with almost unified value. Arabian Sea negative coefficient of mode-1 empirical orthogonal function (-400) occurs on each February and July, coefficient of positive values occurs during April and September of each year. The mixed layer depth can be reconstructed by using the coefficients of time series and the spatial distribution values. Hence so over the strong negative regions of empirical orthogonal function first mode, mixed layer depth reconstruction values will have maximum during February and July when added with mean mixed layer depth of the matrix. Thus this feature is an indicator

of strong convective mixing, which deepens mixed layer depth to a depth of permanent thermocline, during winter season with strong intensification in February. Also the second during July, is a feature of strong

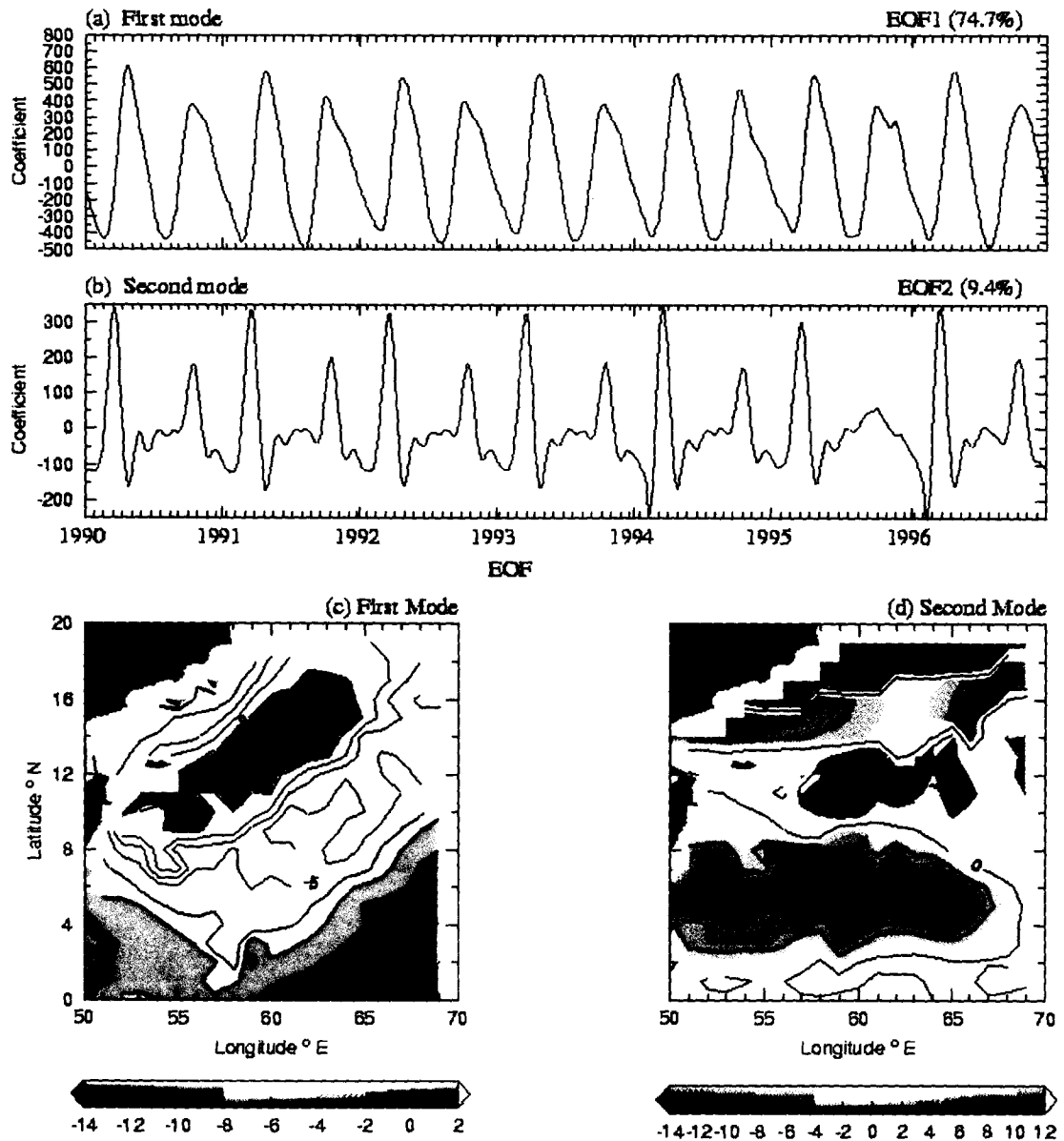


Fig. 5.3: EOF over Arabian Sea.

wind mixing whose strength of penetration is limited and not equal to the winter period. Over the same region minimum values are centered at April and September of each year. Zero value of empirical orthogonal function keeps

minimum variation of mixed layer depth throughout a year. Along Equator at 65°E maximum mixed layer depth seen during the transition months, this is due to the Wyrтки Jet flow which intensifies during this periods. First maxima occurs in April, this is due to the eastward flow of equatorial jet which deepens mixed layer depth along its direction, and reversal during September and hence there are two peaks in mixed layer depth values over this region in a calendar year. The deepening of mixed layer depth due to the formation of the equatorial jet can be identified in mode-2 of EOF (next dominative mode of variability). The contribution of next dominative mode (mode-2) is maximum during the month March along the near equatorial belt (from 50°E to 67.5°E). After March the strength of equatorial jet increases and subsequently this variation could lead to the intensification of mixed layer depth, which mired at mode-1. This is because of the establishment of a strong eastward jet within a few degrees of the equator in the central and eastern portions of the ocean. This arises in direct response to the moderate equatorial westerlies of the transition period, as noted by Wyrтки, (1973). The strong ocean response to these moderate winds is due to the efficient with which zonal winds drive zonal currents near the equator, where Coriolis force is weak.

5.3.2 EOF over Bay of Bengal

The time domain for band pass filter parameters are $P(min) = 45$, $P(1) = 60$, $P(2) = 185$ and $P(max) = 205$ days were chosen in separating the signals of this period as in the case of Bay of Bengal. The EOFs obtained with the filtered data have

been arranged so that the Eigen values are in decreasing order. Figure 5.4 explains time series variation EOFs coefficients and its spatial distribution for mode –1 and mode –2.

First two EOFs explain about 80.9 % of the variance in the band pass filtered data set with first empirical orthogonal function explaining about 69.8 %, and second explains 11.1 % of the total variance in the filtered mixed layer depth derived from model, these EOFs have semiannual periodicity, which is clearly represented in coefficients time series (Fig. 5.4a,b). Even though the obtained signals are semiannual dominant in first mode, they are less in magnitude over the values obtained over Arabian Sea. Among them the variations in coefficient of mode-1 is maximum ranging from –200 to 200, and the other has variations from –60 to 75. The spatial distribution of the first empirical orthogonal function is characterized by maximum aerial coverage of negative signs in mixed layer depth except few near coastal areas. All the values are of unit 10^{-2} . At the central Bay of Bengal large negative values accumulation is observed. Arabian Sea negative coefficient of mode-1 empirical orthogonal function (-200) occurs almost similar time of occurrence as Arabian Sea (February and July of each year), coefficient of positive values occurs during April and September.

Figure 5.4 shows the time series plot of empirical orthogonal function coefficients over Bay of Bengal, which is lesser in magnitude than Arabian Sea. The first two

empirical orthogonal functions explain 80.9 % in total. Mode-1 explains 69.8%, and mode-2 11.1%. Semi-annual variations in mixed layer depth are observed

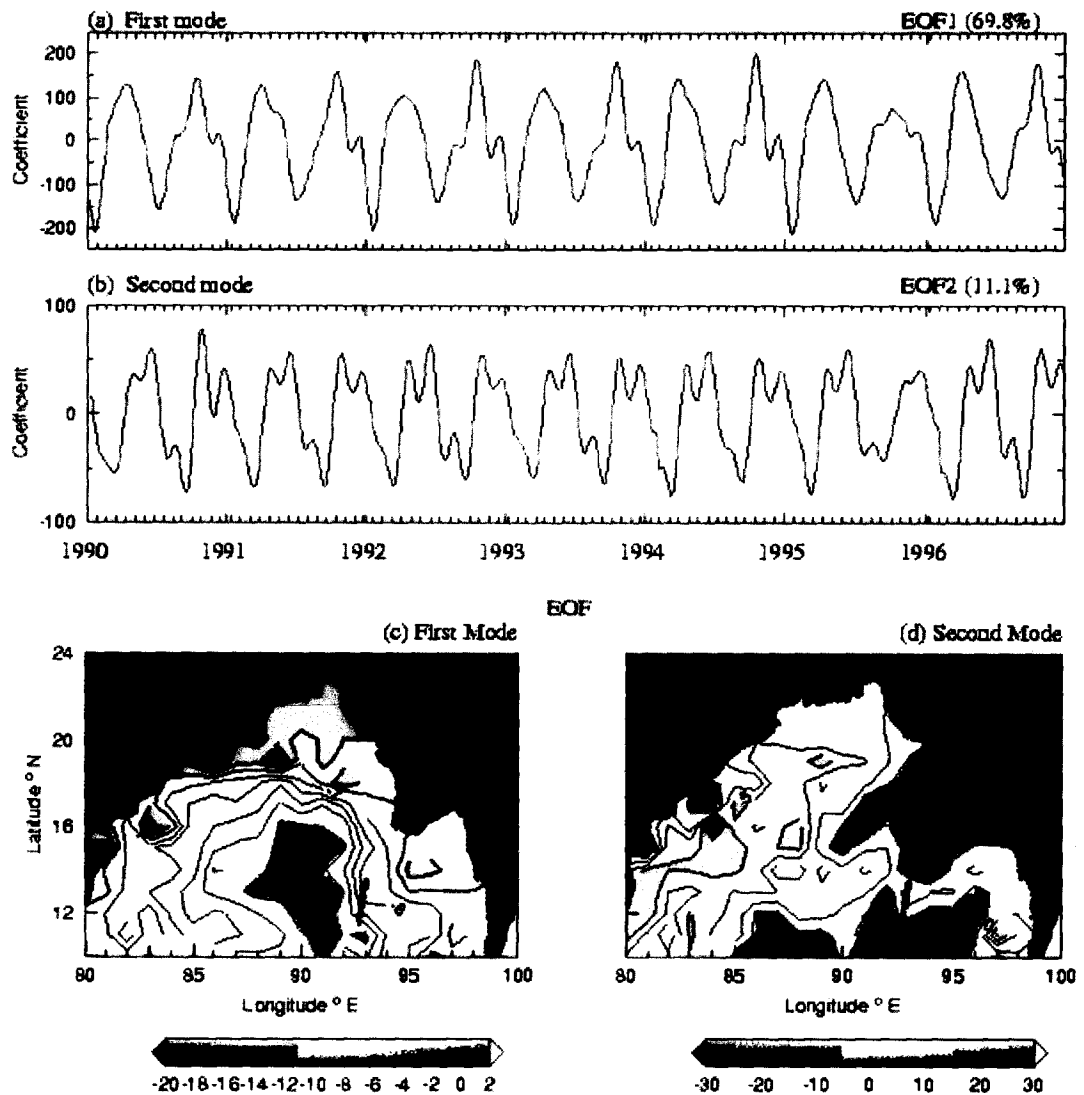


Fig. 5.4: EOF over Bay of Bengal.

in all the two modes. Over Bay of Bengal negative coefficient of mode-1 empirical orthogonal function (-200) occurs on each February and July, coefficient of positive values occurs during April and September of each year. The convective mixing during winter season, which deepens mixed layer depth to a depth (65m) lesser in compare to Arabian Sea. Over the same region will have

minimum values centered to the months April and September; this corresponds to the minimum mixed layer depth values during transition periods. In July Changes that have occurred in the Bay of Bengal are most visible in the spatial distribution of second empirical orthogonal function, which shows deepening along the eastern boundary of the Bay. The northeast monsoon weakened considerably by this time, and most of the circulation in the northern ocean is remnants of flows that were generated earlier.

5.5 Summary

The seasonality of mixed layer depth is studied by using empirical orthogonal function as a tool for extracting the information by applying band pass filter. Arabian Sea and Bay of Bengal the resemblance of EOFs coefficient and its spatial distribution are different, indicating the different dynamical nature of these regions. Over Arabian Sea first two EOFs explain about 84.1 % of the variance (74.7 % and 9.4 % for first and second mode of EOF). The presence of semiannual periodicity is clearly represented by empirical orthogonal function coefficients time series. Among them the variations in coefficient of mode-1 is maximum ranging from -600 to 600, and the other had variations from -200 to 200. The spatial distribution of the first empirical orthogonal function is characterized by the opposite signs in empirical orthogonal function between north east of central Arabian Sea and 10° E parallel to this. This is because of strong convective mixing, which deepens mixed layer depth to a depth of permanent thermocline, during winter season with strong intensification in

February. Also the second during July of strong wind mixing whose strength of penetration is limited and not equal to the winter period. Over the same region with minimum values centered to the months April and September of each year. During the transition period deepening along the near equatorial belt is observed in mode -2 of empirical orthogonal function spatial pattern. During April eastward flow equatorial jet, which deepens mixed layer depth along its direction, and reversal during September, and hence there were twice peak in mixed layer depth values over this region in a calendar year. Over Bay of Bengal the obtained signals are semiannual dominant in first mode they are less in magnitude over the values obtained in Arabian Sea. Among them the variations in coefficient of mode-1 is maximum ranging from -200 to 200, and the other of from -60 to 75. The spatial distribution of the first empirical orthogonal function is characterized by maximum spatial coverage of negative signs in mixed layer depth except few near coastal areas. The influence of monsoonal wind in deepening the mixed layer depth over Bay of Bengal is observed at 90°E; 12.5°N even though the time of occurrences are same as Arabian Sea, the scale of mixed layer depth variation is less. The second deepening of winter cooling is very well observed over this domain. The same region will have minimum values centered to the months April and September; this is due to the minimum mixed layer depth values during transition periods. In July Changes that have occurred in the Bay of Bengal are most visible in the spatial distribution of second empirical orthogonal function, which shows deepening along the eastern boundary of the Bay.

Chapter VI
Conclusion

The response of the ocean mixed layer to surface forcing that are derived from remote sensing observation/re-analysis fields is investigated for the years 1990 – 1996 over the northern Indian ocean spanning from 30°E to 120°E longitude; – 30°N to 30°N latitude. The upper ocean mixed layer is the link by which the atmosphere and ocean are coupled. The form and the strength of mixing are important to concern such as the fluxes of heat, gases, nutrients, and for the growth/health of marine life. Improved understanding of these processes depends in some measure on our prior knowledge of the mixed layer and the variability surface forcing parameters. The dynamics of the mixed layer are influenced by numerous factors, among them solar heating, surface heat loss, turbulent and convective entrainment, horizontal heat flux divergences (advection), and vertical advection induced by Ekman pumping or associated with mesoscale flows.

Mixed layer dynamics has bearing on the exchange of heat and fresh water between the atmosphere and the ocean. By absorbing, transporting and exchanging heat with the atmosphere, this layer affects weather and climate. The most well known example of this is the El Nino phenomenon in the equatorial Pacific Ocean. The sharp gradient in temperature and density below the mixed layer, its variation affects acoustic propagation in the horizontal range. Its dynamics play an important role in chemical, biological activity. This layer also probably has a bearing on the cyclogenesis.

Conventionally, this layer has been studied using the temperature and salinity profiles from the observations of ship and/or data buoys. Due to the limitations of the *in-situ* observations of such profiles, the variations in the mixed layer depth could not be studied extensively both in space and time domain. On the other hand satellite remote sensing with synoptic and temporal coverage has significantly helped in overcoming the difficulty of sparse sea truth measurements and thus giving an opportunity to study this phenomenon through the surface parameters affecting it.

Theoretically these processes are investigated in this thesis under four different categories namely radiative forcing, wind forcing, penetration of solar radiation and evapo-precipitation. The mixing of upper ocean is treated by radiative mixing (buoyancy aided convective mixing) and wind forced mixing. These mixings are well resolved by ocean mixed layer model. The basic families of different models explained in chapter 2.

The spatial and temporal distribution of climatic mean monthly surface parameters is in agreement with the different physical processes cited above is discussed in chapter 3. For example sea surface height is due to thermal expansion of the ocean by a process of radiative forcing into the upper ocean and also associated with convergence and divergence of waters (by wind forcing) and thus increasing the water temperature. The net heat gain is in association with penetrative and non-penetrative solar radiative forcing components at the ocean

surface. The evaporation minus precipitation is in contest of evapo-precipitation process. Some place of time individual parameters dominated the mixed layer evolution thought mostly mixed layer is influenced by many parameters.

Further to model these surface parameters and processes an 1-dimensional mixed layer model of Price, Weller and Pinkel is used. The model equations are diurnal in nature and sensitivity analysis showed that the model is much sensitive to wind speed under constant heat loss and profile of incoming shortwave radiation at the surface of a particular day. Wind speed showed a maximum percentage reduction of 73.35% for varying winds ($12\text{ms}^{-1} - 3 \text{ms}^{-1}$), -13.59% for varying noon radiation ($1000\text{Wm}^{-2} - 400\text{Wm}^{-2}$), and 11.38% for varying total heat loss ($-120\text{Wm}^{-2} - -30\text{Wm}^{-2}$). Here varying noon radiation means changing the nature of incoming shortwave radiation at the surface for a day. The range of parameter values is given in parenthesis.

Interestingly the model computation showed approximately 5m variations in mixed layer depth while varying the water type with higher meteorological forcing conditions. This exercise is not carried out for low met-forcing conditions, since in realistic situation the lower meteorological forcing condition may corresponds to winter season where the depth of convection is greater than the influence depth of biological heating.

The model performance with buoy observations is explained in section 4.3.3. A large difference between the observed and model derived mixed layer depth is found during late December 1994 to mid March 1995 and approximately 20m difference during second deepening of mixed layer. However the model over estimated the second event of deepening and under estimated the first. In an average basis the model could able to predict mixed depth with known initial fields and surface forcing conditions. The model ambiguity could be attributed to the model initialization with Levitus 1982 climatology in case of first event, where convective mixing dominates. The second due to the ill treatment of advection and enhanced biological activity

In order to address the limitations of 1-Dimensional model performance and also to use the satellite/re-analysis observations the following methods are considered and results are also validated with available observations. They are;

- (1). The solar heating on the ocean surface follows a *cosine* pattern
- (2). Wind speed is constant over a day
- (3). Total heat loss from the sea surface is uniform throughout a day
- (4). Classification of water type based on seasonal chlorophyll concentration values

The first assumption is validated using 10th October 1994 hourly observations. Then the *cosine* factor is multiplied with noon radiation to get the radiation value at any given model time. Hence to parameterize noon radiation in to the model we need to convert the daily average incoming shortwave radiation, which is

available from reanalysis to noon radiation. Here a methodology is devised to compute the same and validated with buoy observations. Higher than 50Wm^{-2} root mean square error is observed for the months April, July, August, and October with a confidence level of more than 90% and the error is less in may. Model sensitivity for such error shows very less impact on mixed layer depth. Though the total heat loss and winds showed diurnal variations, the variability is much closer to mean values. Hence we can treat the model is capable of giving better day average mixed layer depth rather than on diurnal scale. The seasonal chlorophyll concentration derived from coastal zone color scanner is used to classify the Indian Ocean waters up to five types in accordance to Jerlov water types. The method of water classification is elaborated in section 4.5.

With the above assumptions, the model ran for the years 1990 – 1996 using ERS winds. Comprehensive oceanographic and atmospheric data set climatic total heat loss and average radiation and derived noon radiation, Levitus 1982 temperature and salinity profiles, coastal zone color scanner derived chlorophyll concentration are also used. The model simulations are performed for water type-1 (called constant biology) and Jerlov waters (called variable biology).

The model performance in the entire Arabian Sea is assessed with joint global ocean flux study and world ocean circulation experiment conductivity temperature and depth profiles during 1994 – 1995. There is a definite improvement by including biology into the model. The root mean square error reduced from 17m

to 14.9m with coefficient of determination is about 0.66 when biology is included in the model computation. Further the model performance is studied at the buoy location with respect to its sub-surface observations of temperature and salinity profiles. The semi-annual oscillation in mixed layer in the mixed layer is observed and also model could able to pick the enhanced convection during winter season. Effect of biological heating of mixed layer is high during August. Over all, there is a reduction in the root mean square error from 15m to 12m at buoy location after the inclusion of the seasonal chlorophyll data in the model run.

The temporal and spatial characteristics of the difference between the two model run for January, May, August, and November of 1994 showed a difference less than 10m at most of the places in the tropical Indian Ocean. However, as exception to this is the Arabian Sea, where a large difference in the two estimations is seen. The difference are seasonally varying, being largest in August. In may, the two simulations in the central Arabian Sea shown large difference ($>10\text{m}$). This implies that the impact of biological heating is quite significant in the Arabian Sea. In contrast, relatively small difference is obtained for the Bay of Bengal. Probably other processes in particular fresh water discharge controls the mixed layer depth in this region more than the heating due to chlorophyll.

The seasonal behaviour of mixed layer depth is explained by empirical orthogonal function (EOF) analysis for the years 1990 – 1996. The data preparation is

explained in chapter 6. Over Arabian Sea, the first two EOFs explain about 84.1% of the total variance (74.7% and 9.4 % for first and second mode of EOF). The presence of semiannual periodicity is clearly represented by empirical orthogonal function coefficients time series. The empirical orthogonal function coefficients over Bay of Bengal were lower in magnitude than Arabian sea, explains 80.9% in total (69.8%, and 11.1%).

Future scope

1. The information of chlorophyll modulation in 3-Dimensional mixed layer model for five water types can be investigated.
2. The evaporation minus precipitation processes over Indian Ocean can be incorporated in the mixed layer model, and this can be parameterized from satellite derived/re-analysis observations.
3. The climatic seasonal resolution of chlorophyll concentration can be made fine resolution to monthly or weekly.
4. Near coastal mixing can be investigated in detail by combining chlorophyll, yellow substance, suspended sediment, and etc. information.
5. Forecasting method of Ali et al, 2006 can be fine-tuned with biological dependent coefficient of the model equations.

Reference

Archer, D. E., Emerson, S., and Wong, C. S., 1993. Numerical prediction of pCO₂ at the sea surface at weather station Papa. *Progress in Oceanography*, Vol. 32, pp. 319-351.

Alexandre, I., 1977. Oceanic absorption of solar energy, in modeling and prediction of the upper layers of the ocean, edited by E. B. Kraus, Pergamon, New York, pp. 326.

Ali, M. M., Sharma, R., and Cheney, R. E., 1998. An atlas of the north Indian Ocean eddies from TOPEX altimeter derived sea surface heights, SP-69-98, Special publication, ISRO.

Ali, M. M., and Rashmi Sharma, 1998. Remote sensing of the marine mixed layer, *Indian journal of Marine Sciences*, Vol. 27, pp. 26-29.

Ali, M. M., Gopalan, A. K. S., Babu, K. N., Rashmi Sharma, and Weller, R. A., 2006. Predicting the upper ocean mixed layer depth in the north Indian Ocean using surface fluxes from a medium range weather forecast system. *Indian journal of Marine Sciences*, Vol. 35, pp. 104-110.

Babu, K. N., Sharma, R., and Agarwal, V. K., 2003. A case study of biological effect on mixed layer depth over north Indian Ocean. International workshop on biogeochemical processes in the northern Indian Ocean, NIO, Goa, February 24-25.

Babu, K. N., Sharma, R., Neeraj, A., Agarwal, V. K., and Weller, R. A., 2004. Study of the mixed layer depth variations within the north Indian Ocean using a 1-D model. *Journal of geophysical research*, Vol. 109, C08016, doi:10.1029/2003JC002024.

Bathen, K. H., 1972. On the seasonal changes in the depth of the mixed layer in the North Pacific Ocean, *Journal of geophysical research*, Vol. 77, pp. 7138-7150.

Bauer, S., Hitchcock, G. L., and Olson, D. B., 1991. Influences of monsoonally forced Ekman dynamics upon surface layer depth and plankton biomass distribution in the Arabian Sea. *Deep Sea research, Part A*. Vol. 38, pp. 531-553.

Berkooz, G., Holmes, P., and Lumley, J. L., 1993. The proper orthogonal decomposition in the analysis of turbulent flows. *Annu. Review in fluid. Mechanics*, Vol. 25, pp. 539-575.

Brown, O. B., Bruce, J. G., and Evans, R., 1980. Evolution of sea surface temperature in Somali basin during the southwestern monsoon of 1979, *Science*, Vol. 209, pp. 595-597.

Bruce, J. G., 1968. Comparison of near Surface Dynamic Topography during the Two Monsoons in the western Indian Ocean, *Deep Sea research*, Vol. 15; pp. 665-677.

Bruce, J. G., 1970. Notes on the Somali current system during southwest monsoon, *Journal of Geophysical research*, Vol. 75, pp. 4170-4173.

Bruce, J.G., 1973. Large-scale variations of the Somali Current during the southwest monsoon. *Deep Sea research*, Vol. 20, pp. 837-846.

Chen, D. R., Rothstein, R., and Busalacchi, A. J., 1994. A hybrid vertical mixing scheme and its application to tropical ocean models. *Journal of physical oceanography*, Vol. 24, pp. 2156-2179.

Chu, P. C., Wang, Q. Q., and Bourke, R. H., 1999. A geometric model for the Beaufort/Chukchi Sea thermocline structure. *Journal of Atmosphere and Ocean Technology*, Vol. 16, pp. 613-632.

Chu, P. C., Chenwu, F., and Liu, W. T., 2000. Determination of Vertical Thermal Structure from Sea Surface Temperature. *Journal of Atmosphere and Ocean Technology*, pp. 971-979.

Clancy R. M. and Pollark, K. D., 1983. A real-time synoptic ocean thermal analysis/forecast system. *Progress in Oceanography*, Vol. 12, pp. 383 – 424.

Colborn, J. G., 1971. Thermal Structure Dynamics in the upper 500 meters of the Indian Ocean, Ocean Science Department, Naval Underwater Research, San Diego pp. 99.

Colborn, J. G., 1975. Thermal Structure of the Indian Ocean, IIOE Monographs, No.2., An East-West Centre press, Univ. Hawaii, Honolulu, pp. 173.

Coantic, M., 1974. Formules empiriques d'évaporation. *Rapport Scientifique CNEXO/IMST No. 74-951*.

Crawford, G. B., and Large, W. G., 1996. A numerical investigation of resonant inertial response of the ocean to wind events. *Journal of physical oceanography*, Vol. 26, pp. 873-891.

Da Silva, A. M., Young, C. C., and Levitus, S., 1994. Atlas of Surface Marine Data 1994, vol. 4, Algorithms and Procedures, NOAA Atlas NESDIS 6, pp. 83.

Davis, R. E., deSzoeko, R., and Niiler, P., 1981. Variability in the upper ocean during MILE. Part I: The heat and momentum balances. *Deep Sea Research*, Vol. 28, pp. 1427-1451.

Defant, A. 1961. *Physical Oceanography*, I. Pergamon press. Oxford

Denman K. L., 1973. A time-dependent model of the upper ocean. *Journal of Physical Oceanography*, Vol. 3, pp.173-184.

Denman, K. L., and Gargett, A. E., 1988, Multiple thermoclines are barriers to vertical exchange in the subarctic Pacific during SUPER, May 1984. *Journal of Marine research*, Vol. 46, pp. 77–103.

Denman, K. L., and Gargett, A. E., 1995. Biological-physical interactions in the upper ocean: the role of vertical and small scale transport processes. *Annual review of Fluid Mechanics*, Vol. 27, pp. 225-255.

Dera, J., 1992. *Marine physics*, Elsevier, Amsterdam–Oxford–New York–Tokyo, pp. 516.

Dodimead, A. J., Favorite, F., and Hirano, T., 1963. Salmon of the North Pacific Ocean. Part II: Review of oceanography of the subarctic Pacific region. *International North Pacific Fisheries Commission, Bull. 13*, Vancouver, BC, Canada, pp. 195.

Ellison, T. H., and Turner, J. S., 1959. Turbulent entrainment in stratified flows. *Journal of fluid mechanics*, Vol. 6, pp. 423-448.

Elsberry, R. L., Friam, T. S., and Trapnell, R. N. J., 1976. A mixed layer model of the oceanic thermal response to hurricanes, *Journal of Geophysical Research*, Vol. 81, pp. 1153-1162.

Eric, D., Skillingstad, Smyth, W. D., and Crawford, G. B., 2000. Resonant wind-driven mixing in the ocean boundary layer, *Journal of Physical Oceanography*, pp. 1866-90.

Findlater, J., 1969. A major low-level air current near the Indian Ocean during the northern summer. *A Quarterly Journal of Royal Met. Society*, Vol. 95, pp. 362-380.

Fischer, A. S., 1997. Arabian Sea mixed layer deepening during the monsoon: Observations and dynamics, M. S. Thesis, Massachusetts Institute of Technology, Cambridge, pp. 130.

Fischer, A. S., 2000. The upper ocean response to the monsoon in the Arabian Sea Ph. D. Thesis, Massachusetts Ins. of Tech. and Woods Hole Oceanography Institute, pp. 222.

Flagg, C. N., Kim, H. S., 1998. Upper ocean currents in the northern Arabian Sea from shipboard ADCP measurements collected during the 1994-1996 U. S. JGOFS and ONR programs. *Deep-Sea Research II*, Vol. 45, pp. 1917-59.

Gallimore, R. G., and Houghton, D. D., 1987. Approximation of ocean heat storage by ocean-atmosphere energy exchange: Implications for seasonal cycle

mixed layer ocean formulation, *Journal of Physical Oceanography*, Vol. 17, pp. 1214-31.

Gallagher, F. H., Storch, V., Schnur, R., and Hannoschok, G., 1991. *The Principle Oscillations Patterns*, Max-Planck-Institute fur meteorologie technical report No. 1.

Ganapati, P. N. and Murty, V. S. R., 1954. Salinity and temperature variations of the surface waters off Visakhapatnam, *Andhra University Memoirs*, Vol. 1, pp. 168-192.

Gargett, A. E., T. B. Sanford, and Osborn, T. R., 1979. Surface mixing layers in the Sargasso Sea. *Journal of Physical Oceanography*, Vol. 9, pp. 1090-1111.

Gasper, P., 1988. Modelling the seasonal cycle of the upper ocean. *Journal of Physical Oceanography*, Vol. 18, pp.161-180.

Gill, A. E., 1981. *Atmosphere-Ocean Dynamics*. Academic Press, pp 662.

Gopalan, A. K. S., Ali, M. M., Babu, K. N., Sharma, R., and Reddy, B. S. R., 2000. Mixed layer depth estimation in the north Indian Ocean using 1-D model. Preprints in proceedings, fifth Pacific Ocean Remote Sensing Conference, (PORSEC National Institute of Oceanography, Goa, India) pp. 439 – 442.

Giulio, B., Ronald, C., George, P. S., Philander, H., and Fedorov, A. V., 2004. The thermal structure of the upper ocean, *Journal of Physical Oceanography*, Vol. 34, pp. 888- 902.

Grassl, H., Jost, V., Schulz, J., Ramesh Kumar, M. R., Bauer, P., and Schluessel, P., 2000. The Hamburg ocean-atmosphere parameters and fluxes from satellite data: A climatological atlas of satellite-derived air-sea interaction parameters over the World Oceans (<http://www.mpimet.mpg.de/Depts/Physik/HOAPS>).

Grawood, R. W., 1977. An oceanic mixed layer model capable of simulating cyclic states. *Journal of Physical Oceanography*, Vol. 7, pp. 455-468.

Hasselmann, K., 1988. The reduction of complex dynamical systems using principle interaction and oscillation patterns, *Journal of Geographical Research*, Vol. 93, pp. 11015-11021.

Hastenrath, S., Lamb, P. J., 1979. *Climatic Atlas of the Indian Ocean, Part I: Surface climate and Atmospheric circulation*: University of Wisconsin press, pp. 19, 97 charts.

Hendricks, J. R., Leben, R. R., Born, G. H., and Koblinsky, C. J., 1996. Empirical orthogonal function analysis of global TOPEX/POSEIDON altimeter data and implications for detection of global sea level rise. *Journal of Geophysical research*, Vol. 101, pp. 14131-45.

Ivanoff, A., 1977. Oceanic absorption of solar energy, in modeling and prediction of the upper layers of the Ocean, Pergamon, New York, pp. 47-71.

Jerlov, N. G., 1968. *Optical Oceanography*. Elsevier, pp. 194.

Kantha, L. H., and Clayson, C. A., 2000. *Numerical Models of Oceans and Oceanic Processes*. Academic Press.

Kara, A. B, Rochford, P. A., and Hurlburt, H. E., 2003. Mixed layer variability over the global ocean, *Journal of Geophysical research*, 108, 3079, doi:10.1029/2000JC000736.

Kim, J. W., 1976. A generalized bulk model of the oceanic mixed layer. *Journal of Physical oceanography*, Vol. 6, pp. 686-695.

Kim, H. S., Flagg, C.N., Howden, S. D., 2001. Northern Arabian Sea variability from TOPEX/Poseidon altimetry data: an extension of the US JGOFS/ONR shipboard ADCP study. *Deep-Sea Research II*, Vol. 48, pp. 1069-96.

Kirth, J. T. O., 1985. Effects of suspensioids (turbidity) on penetration of solar radiation in aquatic ecosystem, *Hydrobiologica*, pp. 125, 195.

Klein, P., Coantic, M., 1981. A numerical study of turbulent processes in the marine upper layers. *Journal of Physical Oceanography*, Vol. 11, pp. 849-863.

Knox, R. A., 1987. The Indian Ocean. Interaction with the monsoon. In: Fein., J. S. Stephen, P. L., (Eds.), *Monsoons*. John Wiley and Sons, New York, pp. 365-397.

Kraus, E. B., and Turner, J. S., 1967. A one-dimensional model of the seasonal thermocline. II. the general theory and its consequences. *Tellus*, Vol. 19, pp. 98-105.

Kraus, E., 1972. *Atmosphere-Ocean Interactions*, clarendon, Oxford, 1972.

Kumar, S. P., Snaith, H., Challenor, P. G., and Guymer, T. H., 1998. Seasonal and inter-annual sea surface height variations of the northern Indian Ocean from TOPEX/POSEIDON altimeter. *Indian Journal of Marine sciences*. Vol. 27, pp. 10-16.

Large, W. G., and Crawford, G. B., 1995. Observations and simulations of upper ocean response to wind events during the ocean storms experiment, *Journal of Physical Oceanography*, Vol. 25, pp. 2831-52.

Large, W. G., Mc Williams, J. C., Doney, S. C., 1994. Oceanic vertical mixing: A review and a model with a non-local boundary layer parameterization. *Reviews of Geophysics* Vol. 32(4), pp. 363-403.

Lee, C. M., Jones, B. H., Brink, K. H., and Fischer, A. S., 2000. The upper-ocean response to monsoonal forcing in the Arabian Sea: seasonal spatial variability. *Deep Sea Research*, Vol. 47, pp. 1177-1226.

Levitus, S., 1982. Climatological atlas of the World Ocean, NOAA Prof pap. 13,173 PP., U.S. Government printing office, Washington D.C.

Levitus, S., and Boyer. T., 1994: Temperature. Vol. 4. World Ocean Atlas. NOAA Atlas NESDIS, pp. 117.

Lewis, M. A., Carr, M. E., Feldman, G. C., Esaias, W., and McClain, C., 1990. Influence of penetrating solar radiation on the heat budget of the equatorial Pacific Ocean, *Nature*, Vol. 347, pp. 543-545.

Lombardo, C. P., and Gregg, M. C., 1989. Similarity scaling of viscous and thermal dissipation in a convecting surface boundary layer. *J. Geophys. Res.*, 94, 6273-6284.

Lumley, J. L., 1971. *Stochastic tools in turbulence*. Academic Press, New York, pp. 194.

Mahrt, L., 1999. Stratified atmospheric boundary layers. *Boundary Layer Meteorology*, Vol. 90, pp. 375-396.

Manghnani, V., Morrison, M., Hopkins, T. S., and Bohm, E., 1998. Advection of upwelled waters in the form of plumes off Oman during the southwest Monsoon. *Deep Sea research*, Vol. 45, pp. 2027-52.

Martin, P. J., 1985. Simulation of the mixed layer at OWS November and Papa with several models. *Journal of Geophysical research*, Vol. 90, pp. 903-916.

Martin, P. J., 1986. Testing and comparison of several mixed-layer models. *Naval Ocean Research and development activities*. Technical report number 143.

McCreary, J. P., Kundu, P. K., and Molinari, R. L., 1993. A numerical investigation of dynamics, thermodynamics and mixed-layer processes in the Indian Ocean, *Progress in Oceanography*, Vol. 31, pp. 181-244.

Mears, C. A., Smith, D. K., and Wentz, F. J., 2001. Comparison of Special Sensor Microwave Imager and buoy-measured wind speeds from 1987 to 1997, *Journal of Geophysical research*, Vol. 106, pp. 11719–29.

Meehl, G. A., 1984. A calculation of ocean heat storage and effective ocean surface layer depths for the Northern Hemisphere, *Journal of Physical Oceanography*, Vol. 14, pp. 1747 – 1761.

Mellor, G. L., 1973. Analytic prediction of the properties of stratified planetary surface layers. *Journal of the Atmospheric Sciences*, Vol. 30, pp. 1061-1069.

Mellor, G. L., Durbin, P. A., 1975. The structure and dynamics of the ocean surface mixed layer. *Journal of physical oceanography*, Vol. 5, pp. 718-728.

Mellor G. L., and Yamada, T., 1974. A hierarchy of turbulence closure models for planetary boundary layers. *Journal of Atmospheric Science*, Vol. 31, pp. 1791 – 1806.

Mellor, G. L. and Yamada, T., 1982. Development of a turbulence closure model for geophysical fluid problems. *Review of Geophysics and Space Physics*, Vol. 20, pp. 851-876.

Miller, L., and Cheney, R., 1990. Large-scale meridional transport in the tropical Pacific Ocean during the 1986– 1987 El Niño from Geosat, *Journal of Geophysics research*, Vol. 95, pp. 17,905– 19.

Mitchum, G. T., 1993. Principal component analysis: Basic methods and extension. In P. Muller and Henderson (Eds), *statistical methods in physical oceanography*, Proc. ‘Aha Huliko’a Hawaiian winter workshop, Hawaii, Jan 12-15, 1993, pp 185-199. School of Ocean and Earth Science, Tech., Honolulu Special publication.

Molinari, R. L., Olson, D., Reverdin, G., 1990. Surface current distributions in the tropical Indian Ocean derived from compilations of surface trajectories. *Journal of Geophysical Research*, Vol. 95, pp. 7217-7238.

Monterey, G., and Levitus, S., 1997. Seasonal variability of mixed layer depth for the World Ocean, NOAA Atlas NES-DIS 14, 100 pp., U. S. Govt. Print. Off, Washington, D. C.

Morel and Antoine, 1994. Heating rate in the upper ocean in relation to its bio-optical state *Journal of Physical Oceanography*, Vol. 24, pp. 1652-64

Moum, J. N., and Smyth, W. D., 2001. Upper ocean mixing processes, Academic press. Doi:10.1006/rwos.2001.0156.

Nerem, R. S., Rachlin, K. E., and Beckley., B. D., 1997. Characterization of global sea level variations observed by T/P using empirical orthogonal functions. *Surv. Geophysics*, Vol. 18, pp. 293-302.

Niiler P. P., and Kraus, E. B., 1977. One-dimensional models of the upper ocean. In: *Modelling and predications of the upper layers of the ocean*, E. B. Kraus, editor, Pergamon, Elmsford, New York, pp. 143-172.

Oberhuber, J. M., 1988. An atlas based on the "COADS" data set: The budgets of heat, buoyancy and turbulent kinetic energy at the surface of the global ocean. Rep. 15, Max-Planck-Institute for Meteorology, pp. 20.

Paulson, C. A., and Simpson, J. J., 1977: Irradiance measurements in the upper ocean. *Journal of Physical Oceanography*, Vol. 7, pp. 952-956.

Parsons, T. R., Takahashi, M., Harhrave, B., 1984. Biological Oceanographic Processes. Pergammon Press, Oxford, U. K.

Pickard, G. L., and Emery, W. J., 1982. Descriptive physical oceanography, 4th edition, Pergamon press.

Pickard, G. L., and Emery, W. J., 1990. Descriptive physical oceanography, 6th edition, Pergamon press.

Pollard, R. T., Rhines, P. B., and Thompson, R., 1973. The deepening of the wind-mixed layer. Geophysical Fluid Dynamics, Vol. 4, pp. 381-404.

Preisendorfer, R. W., 1988. Principal component analysis in Atmospheric Science, Elsevier, Amsterdam, New York, Vol. 17, pp. 425.

Price, J. F., Mooers, C N. K., Leer, J. C. V., 1978. Observation and simulation of storm-induced mixed-layer deepening. Journal of Physical Oceanography, Vol. 8, pp. 582-599.

Price J. F., Weller, R. A., Bowers, C. M., and Briscoe, M. G., 1987. Diurnal response of sea surface temperature observed at the Long Term Upper Ocean Study (34°N, 70°W) in the Sargasso Sea. Journal of Geophysical Research, Vol. 92, pp. 14480-90.

Price, J. F., Weller, R. A., and Pinkel, R., 1986. Diurnal Cycling: Observations and model of the upper ocean response of diurnal heating, cooling, and wind mixing. *Journal of Geophysical research*, Vol. 91, pp. 8411 – 8427.

Quarishie, G. S 1984. Circulation in the north Arabian Sea at Murray Ridge during the S. W. monsoon. *Deep Sea Research*, Vol. 31, pp. 651-664.

Ramesh Babu, V. and Sastry, J. S., 1984. Summer Cooling in the East Central Arabian Sea – A process of Dynamic Response to the Southwest Monsoon., *Mausam.*, Vol. 35, pp. 17-26.

Rao, R. R., and Mathew, B., 1990. A case study on the mixed layer variability in the south central Arabian Sea during the onset phase of MONEX-79. *Deep Sea research*, Vol. 37, pp. 227-243.

Rao, R. R., Molinari, R. L., Festa, J. F., 1989. Evolution of the climatological near-surface thermal structure of the tropical Indian Ocean I. Description of mean monthly mixed layer depth, sea surface temperature, surface current, and sea surface meteorological fields. *Journal of Geophysical research*, Vol. 94, pp. 10801-10815.

Rao, R. R., Molinari, R. L., Festa, J. F., 1991. Surface meteorological and subsurface oceanographic atlas of the tropical Indian Ocean. NOAA Tech. Memor. ERL-AOML- pp. 69, 59.

Rao, D. P., Sarma, R. V. N., Sastry, J. S., and Premchand, K., 1976. On the lowering of the surface temperature in the Arabian Sea with the advance of the

southwest monsoon season, Proc. Of IITM Symposium on Tropical Monsoons held at Pune, India, 8-10 September.

Rao, R. R., and Sivakumar, R., 1998. Observed seasonal variability of heat content in the upper layers of the tropical Indian Ocean from a new global ocean temperature climatology. *Deep Sea research I*, Vol. 45, pp. 67-89.

Ravindran, P., Wright, D. G., Platt, T., Sathyendranath, S., 1999. A generalized depth-integrated model of the oceanic mixed-layer, *Journal of Physical Oceanography*, Vol. 29, pp. 791-803.

Roden, G. I., 1979. The depth variability of meridional gradients of temperature, salinity and sound velocity in the western North Pacific, *Journal of Physical Oceanography*, Vol. 9, pp. 756-767.

Rosati, A., and Miyakoda, K., 1988. A general circulation model for upper ocean simulation. *Journal of Physical Oceanography*, Vol. 18, pp. 1601-1626.

Reynolds, R. W. and Smith, T. M., 1994. Improved global sea surface temperature analysis using optimum interpolation, *Journal of Climate*, Vol. 7, pp. 929-948.

Sathyendranath, S., Gouveia, A. D., Shetye, S. R., and Platt, T., 1991. Biological controls of surface temperature in the Arabian Sea, *Nature*, Vol. 349, pp. 54– 56.

Schott, F., 1983. Monsoon response of the Somali current and associated upwelling. *Progress in Oceanography*, Vol. 12, pp. 357-381.

Schneider, N., and Muller, P., 1990. The meridional and seasonal structures of the mixed-layer depth and its diurnal amplitude observed during the Hawaii-to-Tahiti Shuttle experiment. *Journal of Physical Oceanography*, Vol. 20, pp. 1395–1404.

Semtner, A. J., and Chervin, R. M., 1992. Ocean general circulation from a global eddy-resolving model, *Journal of Geophysical research*, Vol. 97, pp. 5493-5550.

Shay, T. J., and Gregg, M. C., 1986. Convectively driven turbulent mixing in the upper ocean, *Journal of Physical Oceanography*, Vol. 16, pp. 1777-1798.

Shetye, S. R., 1986. A model study of the seasonal cycle of the Arabian Sea surface temperature. *Journal of Marine research*, Vol. 44, pp. 521-542.

Shi, W., Morrison, J. M., Bohm, E., and Manghanani, V., 2000. The Oman upwelling zone during 1983, 1994 ad 1995. *Deep Sea research*, Vol. 47, pp. 1227-1247.

Simpson, J. J., and Dickey, T. D., 1981. The relationship between downward irradiance and upper ocean structure, *Journal of Physical Oceanography*, pp. 11,309.

Simpson, J. J. and Dickey, T. D., 1981. Alternative parameterizations of downward irradiance and their dynamical significance, *Journal of Physical Oceanography*, pp. 11,876.

Simonot, Y. Y., Dollinger, E., and Le Treut, H., 1988. Thermodynamic-biological-optical coupling in the oceanic mixed layer, *Journal of Geophysical research*, Vol. 93, pp. 8193-8202.

Sprintall, J., and D. Roemmich, 1999. Characterizing the structure of the surface layer in the Pacific Ocean. *Journal of Geophysical research*, Vol. 104, pp. 23,297–23,311.

Sprintall, J., and Tomczak, M., 1992. Evidence of the barrier layer in the surface layer of tropics, *Journal of geophysical research*, Vol. 97, pp. 7305-7316.

Stapleton, N. R., Aicken, W. T., Dovey, P. R., and Scott, J. C., 2002. The use of radar altimeter data in combination with other satellite seasons for routine monitoring of the ocean: Case study of the northern Arabian Sea and Gulf of Oman, *Canadian Journal of Remote sensing*, pp. 567-572.

Stevenson, J. W., 1979. On the effect of dissipation on seasonal thermocline models. *Journal of Physical Oceanography*, Vol. 9, pp. 57-64.

Stevenson, J. W., and Niiler, P. P., 1983. Upper Ocean heat budget during the Hawaii-to- Tahiti Shuttle experiment. *Journal of Physical Oceanography*, Vol. 13, pp. 1894-1907.

Stull R. and Kraus, E. B., 1987. The transient model of the upper ocean. *Journal of Geophysical research*, vol. 93, pp. 10745-10755.

Swallow, J. C., Molinari, R. L., Bruce, J. G., Brown, O. B., and Robert, H. E., 1983. Development of Near-Surface Flow Pattern and Water Mass Distribution in the Somali Basin in Response to the Southwest Monsoon of 1979. *Journal of Physical Oceanography*: Vol. 13, pp. 1398–1415.

Tapley, B. D., Chambers, D. P., Shum, C. K., Eanes, R. J., Ries, J. C., and Stewart, R. H., 1994. Accuracy assessment of the large-scale dynamic ocean topography from TOPEX/POSEIDON altimetry, *Journal of Geophysical research*, Vol. 99, pp. 24,605-17.

Therry, G., Lacarrere, P., 1983. Improving the eddy kinetic energy model for planetary boundary layer description. *Boundary layer Meteorology*, Vol. 25, pp. 63-88.

Wanninkhof, R., 1992. Relationship between wind-speed and gas-exchange over the ocean, *Journal of Geophysical Research*, Vol. 97, pp. 7373-7382.

Watson, W. G., and Margarita, E. C., 2000. Global seasonal climatologies of ocean chlorophyll, blending in-situ and satellite data for the CZCS Era. *Journal of Geophysical Research*,

Webster, P. J., and Yang, S., 1992. Monsoon and ENSO: Selectively interactive systems. *Quarterly Journal of Royal Meteorology Society*, Vol. 118, pp. 877–926.

Weller, R. A., Baumgartner, M. F., Josey, S. A., Fischer, A. S., and Kindle, J. C., 1998. Atmospheric forcing in the Arabian Sea during 1994-1995:

observations and comparisons with climatology and models, Deep Sea research II, Vol. 45, pp. 1961-1999.

White, W. B., Cayan, D. R., and Lean, J., 1998. Global upper ocean heat storage to radiative forcing from changing solar irradiance and increasing greenhouse gas/aerosol concentration, Journal of Geophysical research, Vol. 103, pp. 21, 355-66.

Woods, J. D. 1984. Air-Sea interaction and the upper ocean in global climate. In the Global Climate, 141-187. (Ed by Houghton) Cambridge Univ. Press.

Woods, J. D., and Barkmann, 1986. The response of the upper ocean to solar heating. I: The mixed layer, Quarterly journal of the Royal Meteorological Society, January 1986, Vol. 112, pp. 1-27.

Wooster, W. S., Schaefer, M. B., and Robinson, M. K., 1967. Atlas of Arabian Sea for fishery Oceanography, Univ. California, Institute of Marine Resources, IMR-Ref: pp. 67-12.

Wyrki, K., 1971. Oceanographic Atlas of the International Indian Ocean Expedition. National Science Foundation, Washington DC, pp.531.

Wyrki, K., 1973. An equatorial jet in the Indian Ocean. Science Vol. 181, pp. 262-264.

Yan, X. H., 1989. Applications of remote sensing to studies of oceanic upper mixed layer dynamics. Ph. D. Thesis. State University of New York, Stony Brook, University Microfiche Cooperation.

Yan, X. H., Bowman, A., and Schubel, J., 1989. Satellite observed spatial and temporal variability of the mixed layer depth in the Sargasso Sea. Proceedings of IEEE IGARSS, held in Vancouver, Canada, July 1989. Vol. I, pp. 323-329.

Yan, X. H., Okubo, A., Schubel, J. R., and Pritchard, D. W., 1991. An analytical mixed layer remote sensing model. Deep Sea research, Vol. 38, pp. 267-287.

Annexure

The criterion for the mixed layer depth estimation used by different authors are;

The mixed layer depth criteria used by researchers vary widely. Various schemes based on fixed temperature gradient (Ali and Sharma, 1998), fixed density difference (Levitus, 1982; Gopalan et al, 2000), statistical significance criterion of Bathen, (1972), and fixed temperature difference (Monterey and Levitus, 1997) have been utilized in the past. Sprintall and Tomczak, (1992) pointed out that the temperature criterion for mixed layer depth estimation ignores salinity effects, which can lead to errors of typically 10–20 m. Recently, Kara et al., (2003) made a detailed study of the temperature and density criterion used for defining the surface mixed layer of the world ocean. In regions like Bay of Bengal, where due to the fresh water influx, the stratification is high; the two criteria may lead to quite different values. Hence it is necessary to compare the different mixed layer depth criteria. However, the lack of adequate CTD data on longer timescales hampers study in Bay of Bengal. In the future, profiling ARGO floats (see <http://www.argo.ucsd.edu/whatisargo.html>) will provide salinity as well as temperature profiles and make significant improvements to data availability. Here we compute mixed layer depth from both temperature and density profiles in order to assess the differences. The approach is different than the one adopted by Kara et al., (2003). We considered the Levitus criteria for computing mixed layer depth with density profiles. For this purpose, subsurface profiles from the Woods

Hole Oceanographic Institution (WHOI) mooring in the central Arabian Sea were used.

Mixed layer depth computed from density (Levitus criteria) and temperature (0.1° C from water temperature at the surface) profiles for the yearlong observations are shown in Figure app. Mixed layer depth computed from the two criteria match well over a large part of the mooring record. The average difference between the two MLDs is about 14 m. During 15 February to 15 March, the two estimates show large differences. In this period, mixed layer depth (computed using density criteria) fluctuations were also too large. This is a period of intense heating, leading to enhanced stratification, and shallow MLDs, which are represented well by the temperature criteria. However, MLDs computed with the density criteria show some isolated large values. It is known that salinity variations are generally not large in this region, and when we looked at the salinity data from this period, no abnormal pattern in its distribution is noted. This indicates that differences in the mixed layer depth estimates, computed using the two criteria, are derived from the different values selected as thresholds for determining mixed layer depth from temperature and density profiles. One point worth noting is that almost throughout the period, mixed layer depth is slightly deeper using density criteria than the temperature one. However, the results remain qualitatively the same regardless of the particular criterion used; that is, the time series patterns of mixed layer properties are equivalent. However, the differences between the two mixed layer depth series vary from 4 to 80m (differences are large during February–March, the reason for which has already been explained). This certainly cannot be

considered to be statistically insignificant. Hence one should be cautious in using the temperature criteria to define mixed layer depth.

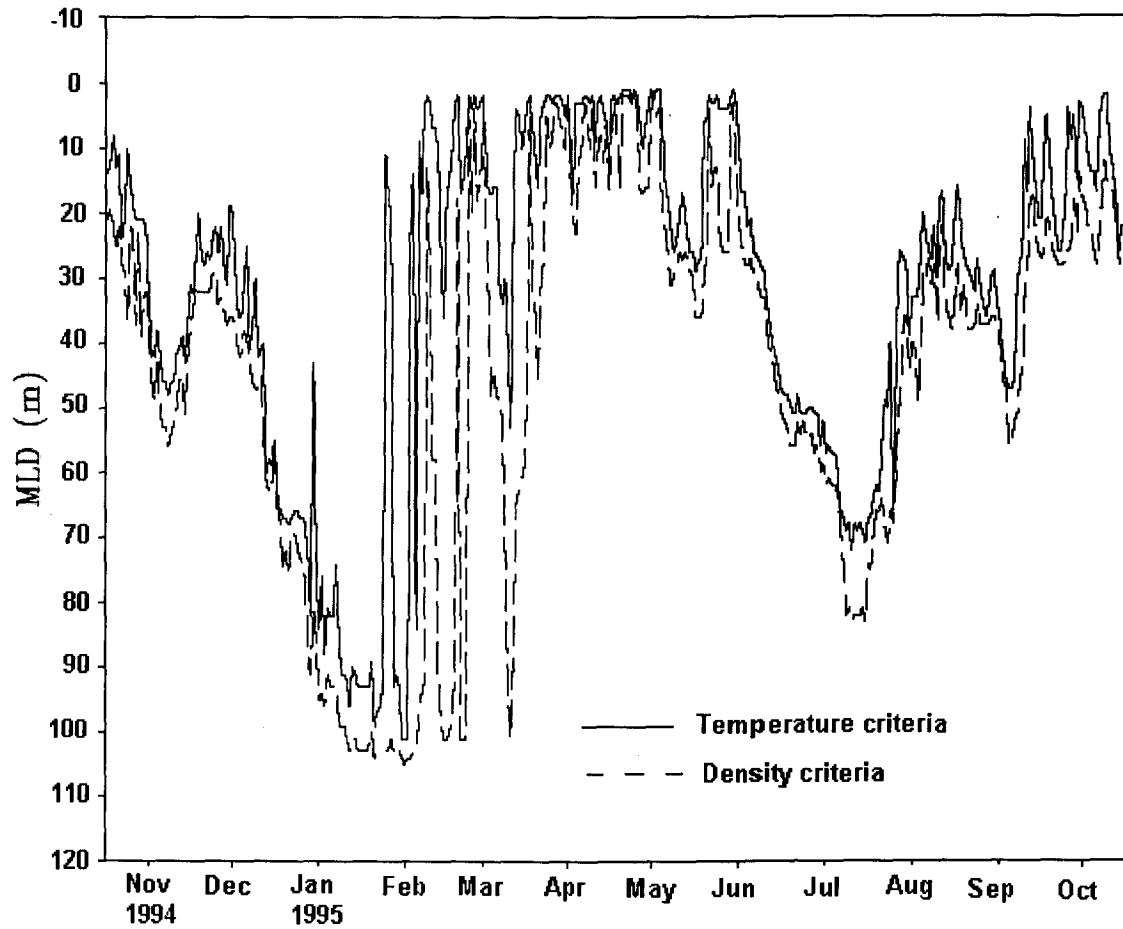


Fig. app: Time series of MLD (meters) computed with density (dashed line) and temperature (solid line) criteria at the data buoy location in central Arabian Sea.